Auxiliary barrier function of karyopherins at the Nuclear Pore Complex

Inauguraldissertation

zur
Erlangung der Würde eines Doktors der Philosophie
vorgelegt der
Philosophisch-Naturwissenschaftlichen Fakultät
der Universität Basel

von

Joanna Małgorzata Kalita

Basel, 2023

Genehmigt von der Philosophisch-Naturwissenschaftlichen Fakultät auf Antrag von

Erstbetreuer: Prof. Dr. Roderick Y.H. Lim

Zweitbetreuer: Prof. Dr. Markus Affolter

Externe Expertin: Prof. Dr. Liesbeth Veenhoff

Basel, 19.10.2021

Prof. Dr. Marcel Mayor, Dekan

Declaration

During my doctoral work at the Biozentrum of the University of Basel, two review articles and one research paper were published. Moreover, another research manuscript is in revision. The presented thesis includes parts or the extended versions of the following publications:

1. *The role of nucleocytoplasmic transport in mechanotransduction*
   Elena Kassianidou, Joanna Kalita, and Roderick Y. H. Lim
   Published in Experimental Cell Research, 377, 86-93, doi:10.1016/j.yexcr.2019.02.009 (2019)

2. *On the asymmetric partitioning of nucleocytoplasmic transport – recent insights and open questions*
   Joanna Kalita, Larisa E. Kapinos, and Roderick Y. H. Lim
   Published in Journal of Cell Science, 134(7), doi:10.1242/jcs.240382 (2021)

3. *Karyopherin enrichment and compensation fortifies the nuclear pore complex against nucleocytoplasmic leakage*
   Joanna Kalita[1], Larisa E. Kapinos[1], Tiantian Zheng[2], Chantal Rencurel[1], Anton Zilman[2], and Roderick Y. H. Lim[1]
   [1]Biozentrum and the Swiss Nanoscience Institute, University of Basel, Switzerland
   [2]Department of Physics, University of Toronto, Canada
   Published in Journal of Cell Biology, 221(3), doi:10.1083/jcb.202108107 (2022).

4. *Mechanism of exportin retention in the cell nucleus* (in revision)
   Larisa E. Kapinos, Joanna Kalita, Elena Kassianidou, Chantal Rencurel, and Roderick Y. H. Lim

Acknowledgments

First, I would like to thank my supervisor, Prof. Dr. Roderick Lim for allowing me to pursue my doctoral research in his laboratory. I would also like to express my deep gratitude to Dr. Larisa Kapinos for her generous support and bottomless helpfulness. Thank you for sharing your knowledge and teaching me how to be a better scientist.

I would also like to thank all present and former members of the Lim Group with whom I had the pleasure to cross paths. None of this would be possible without the tremendous work of our lab technician, Chantal Rencurel, who made sure I had everything I needed to complete my project. Special thanks also go to Dr. Elena Kassianidou whose passion for science was and still is contagious.

I am grateful to all Biozentrum Core Facilities, especially Imaging Core Facility, for providing exceptional expertise which allowed me to perform experiments I would not be able to complete on my own. I would like to thank the Werner Siemens Foundation and the Biozentrum for granting me a three-year-long fellowship that funded the first years of my Ph.D.

Many thanks to all my friends, old ones and those I have met during my stay in Basel. Thanks, Gosia, Kasia, and Natalie for your scientific and personal support.

Finally, I would like to thank Quentin for always having my back and simply being there whenever I needed it.

Table of Contents

Chapter 1. Introduction

1.1 Nucleocytoplasmic transport 1
1.2 NCT is impaired in aging and cellular pathologies 3
1.3 Karyopherins (Kapβs) orchestrate NCT 4
1.3.1 Conformational flexibility of Kapβs 4
1.3.2 Kapβ transport kinetics within NPCs 5
1.3.3 Variety of Kapβ cargoes 6
1.4 The Nuclear Pore Complex 11
1.5 Nature of the permeability barrier 13
1.6 Aim of the Thesis 16
1.7 References 17

Chapter 2. Karyopherins *in vivo*- localization and NPC enrichment

2.1 Asymmetric partitioning of Kapβs 33
2.2 Kapβ enrichment at NPCs supports the Kap-centric control model 35
2.3 Subcellular localization of fluorescently-tagged Kapβs 37
2.4 Persistence of Kapβs at the NPCs 38
2.5 Cellular abundance of Kapβs in MDCK cells 40
2.6 Conclusions 41
2.7 Materials and Methods 41
2.7.1 Cell culture 41
2.7.2 Mammalian cell transfection 41
2.7.3 Immunofluorescence 42
2.7.4 Permeabilized cell assay 42
2.7.5 Confocal microscopy, imaging, and analysis 42
2.8 References 46

Chapter 3. Binding of Kapβs *in vitro* and *ex vivo*

3.1 Surface Plasmon Resonance (SPR) 53
3.2 Measurement of Kapβ binding constants 54
3.3 Analysis of Kapβ binding kinetics 55
3.4 Molecular occupancy of Kapβs within FG Nup layers 56
3.5 Concentration-dependent binding of exoKapβs to NPCs *ex vivo* 58
3.6 Competitive binding of Kapβs to NPCs in permeabilized cells 60
3.7 Biophysical basis of Kapβ competition at the NPC 63
3.8 Conclusions 65
3.9 Materials and Methods 66
3.9.1 Protein expression and purification 66
3.9.2 Fluorescent labeling 67
3.9.3 Dynamic Light Scattering (DLS) 68

3.9.4 Reagents 68
3.9.5 SPR Sensor Chip Preparation 68
3.9.6 SPR measurements 68
3.9.7 SPR protocol 69
3.9.8 SPR analysis 69
3.9.9 Kapβ binding in permeabilized cells 72
3.9.10 Confocal microscopy, imaging, and analysis 73
3.9.11 Mean-field model of Kapβ accumulation within a pore 74
3.10 References 76

Chapter 4. Kapβs are integral constituents of the NPC *in vivo*
4.1 Kap-centric model in living cells 81
4.2 Evidence of Kapβ compensation at the NPC 81
4.3 Kapβ1 depletion impairs NPC barrier function *in vivo* 86
4.4 CRM1 reduction does not show to affect the NPC permeability barrier 88
4.5 NPC passive permeability increases upon Kapβ1 reduction 88
4.6 NPCs *in vivo* are saturated with Kapβ1 90
4.7 The permeability barrier remains intact after CRM1 depletion 90
4.8 Conclusions 92
4.9 Materials and Methods 95
4.9.1 siRNA design and validation 95
4.9.2 Western Blotting 95
4.9.3 Knockdown of Kapβ1 and CRM1 in stable MDCK cell lines 96
4.9.4 Immunofluorescence 96
4.9.5 Confocal microscopy, imaging, and analysis 97
4.9.6 Cell and nuclear volume measurements 97
4.9.7 Fluorescent Recovery After photobleaching (FRAP) experiments 98
4.9.8 Analysis of FRAP half-time recovery (τ) 98
4.9.9 Analysis of NPC permeability changes 100
4.10 References 101

Chapter 5. Outlook
5.1 Role of NCT in mechanotransduction 107
5.2 Cell squeezing experiments 109
5.3 Prospects 111
5.4 References 111

List of Figures

Figure 1.1 Mechanism of nucleocytoplasmic transport..... 2
Figure 1.2 Structure and conformational flexibility of Kapβs 5
Figure 1.3 Diversity of NCT and cargoes 7
Figure 1.4 Overall structure of the NPC. 11
Figure 1.5 Diversity and localization of nucleoporins (Nups) within the NPC. 12
Figure 1.6 Models of NPC selective barrier..... 15
Figure 2.1 Asymmetric partitioning of Kapβs and their enrichment at NPCs in cells..... 34
Figure 2.2 Recapture at NPCs facilitates nucleocytoplasmic partitioning..... 36
Figure 2.3 Kapβs enrichment *in vivo* 38
Figure 2.4 Retention of Kapβ1-EGFP, EGFP-CRM1, and Imp5-mCherry at NPCs following digitonin permeabilization and Ran mix treatments. 39
Figure 2.5 Absolute abundance of Kapβs in MDCK cells..... 40
Figure 3.1 Binding of CRM1 and Imp5 to FG Nup layers. 53
Figure 3.2 Equilibrium analysis of Kapβ-FG Nup binding. 54
Figure 3.3 Kinetic analysis of Kapβ-FG Nup interactions 56
Figure 3.4 FG Nup layer height is determined by the interacting Kapβ..... 57
Figure 3.5 Kapβ1, CRM1, and Imp5 bind to NPCs in a concentration-dependent manner 59
Figure 3.6 Kapβ1 pre-loading shifts K_D to weaker values..... 60
Figure 3.7 Pairwise binding reveals the relative occupancies for different Kapβs..... 63
Figure 3.8 Promiscuous binding is balanced by Kapβ size, binding affinity, and abundance.... 64
Figure 3.9 Reduction of Kapβ1 occupancy in response to CRM1 and Imp5 binding 65
Figure 3.10 Fluorescence calibration curves..... 73
Figure 4.1 Quantitative analysis of Kapβs after siRNA treatment..... 83
Figure 4.2 NE occupancy of CRM1 increases upon Kapβ1 silencing..... 84
Figure 4.3 CRM1 silencing does not lead to significant changes in Kapβ1 occupancy. 85
Figure 4.4 Kapβ1 enrichment fortifies the NPC permeability barrier *in vivo* 87
Figure 4.5 CRM1 depletion does not disturb the NPC permeability barrier 88
Figure 4.6 Kapβ1 depletion softens NPC permeability barrier against non-specific cargoes *in vivo*. 89
Figure 4.7 Overexpression of Kapβ1 does not further fortify the permeability barrier..... 90
Figure 4.8 CRM1 depletion does not impact NPC permeability against 2xEGFP 91
Figure 4.9 Summary of Kapβ enrichment and compensation at the NPC permeability barrier 93
Figure 5.1 Cellular mechanotransduction is mechanical and biochemical. 107
Figure 5.2 Schematic of combined spinning disk (SD) and atomic force microscopy (AFM) setup 109
Figure 5.3 Nuclear leakage of cargo upon indentation. 110

Abbreviations

3D	Three-dimensional
AFM	Atomic force microscopy
ATP	Adenosine tri-phosphate
BSA	Bovine serum albumin
CAS	Cellular apoptosis susceptibility protein homolog (Exportin-2)
CRM1	Chromosomal maintenance 1 (Exportin-1)
DAPI	4′,6-diamidino-2-phenylindole
DLS	Dynamic light scattering
EGFP	Enhanced green fluorescent protein
FACS	Fluorescence-activated cell sorting
FIB	Focused ion beam
FRAP	Fluorescent recovery after photobleaching
GDP	Guanosine di-phosphate
GFP	Green fluorescent protein
GTP	Guanosine tri-phosphate
IF	Immunofluorescence
Imp5	Importin-5
Kapβ1	Importin subunit beta-1 (Karyopherin beta-1)
Kapβs	Karyopherins
MS	Mass spectrometry
N:C	Nuclear-to-cytoplasmic ratio
NCT	Nucleocytoplasmic transport
NE	Nuclear envelope
NES	Nuclear export signal
NLS	Nuclear localization signal
NPC	Nuclear pore complex
NTF2	Nuclear transport factor 2
NTR	Nuclear transport receptor
Nup	Nucleoporin
ROI	Region of Interest
siRNA	Small interfering ribonucleic acid
SPR	Surface plasmon resonance

Abstract

Nuclear pore complexes (NPCs) are highly selective gateways that mediate nucleocytoplasmic transport (NCT) in eukaryotic cells. Recent discoveries have shown that leaky NPCs and defective NCT are linked to aging, neurodegenerative disorders, and viral pathogenesis. Nevertheless, their exact underlying cause(s) are unknown, reflecting an incomplete understanding of the key regulatory aspects of NPC function. At the heart of this problem lies the NPC permeability barrier, whose behavior has been largely modeled after the *in vitro* behavior of intrinsically disordered proteins termed phenylalanine-glycine nucleoporins (FG Nups). Nonetheless, this view is puzzling since certain key soluble nuclear transport receptors called β-karyopherins (Kapβs) are strongly enriched within NPCs *in vivo*.

The experimental results reported in this thesis show that two major Kapβs, Kapβ1 (importinβ) and CRM1 (exportin1) are essential for fortifying the NPC permeability barrier against defective NCT and nuclear leakage *in vivo*. A further surprise is that CRM1 partially compensates for Kapβ1 upon depletion of the latter from the NPC, which suggests that Kapβ1 and CRM1 engage in a balancing act to reinforce NPC barrier function. Combining *ex vivo* and biophysical experimentation, as well as computational modeling, we further show how the occupancy of different Kapβs at the NPC is constrained by their size, cellular abundance, binding avidity to the FG Nups, and competition with other Kapβs, such as demonstrated for another Kapβ, Importin-5 (Imp5). Taken together, these findings provide important intersection points and raise new questions with respect to the causes of NPC leakage and defective NCT in aging and cellular pathologies.

Chapter 1

Introduction

Adapted from

On the asymmetric partitioning of nucleocytoplasmic transport – recent insights and open questions

Joanna Kalita, Larisa E. Kapinos and Roderick Y. H. Lim

Published in Journal of Cell Science, 134(7), jcs.240382 (2021)

1.1 Nucleocytoplasmic transport

Eukaryotic cells feature a protective double-layered membrane known as the nuclear envelope (NE) that encapsulates the nucleus within the cytoplasm. NE separates the genome from the protein synthesis machinery and thus enables spatiotemporal control of transcription and translation. However, this requires key macromolecular cargoes, such as transcription factors and mRNA, to be selectively shuttled into or out of the cell nucleus. Understandably, neurodegeneration (Kim and Taylor, 2017), aging (Cho and Hetzer, 2020), cancer (Cagatay and Chook, 2018; Dickmanns et al., 2015), and viral pathogenesis (Fulcher and Jans, 2011; Miorin et al., 2020; Yarbrough et al., 2014) are associated with a dysregulation of this intracellular trafficking process, which is termed nucleocytoplasmic transport (NCT) (Stewart, 2007; Strambio-De-Castillia et al., 2010) and proceeds through nanoscale conduits in the NE known as nuclear pore complexes (NPCs) (Beck et al., 2007; Eibauer et al., 2015; Kim et al., 2018; von Appen et al., 2015).

NCT is unprecedentedly selective and efficient within the complex biological milieu. To appreciate its importance, range, and complexity, at least 17% of all eukaryotic proteins are deemed to be imported into the nucleus (Cokol et al., 2000) with over 1000 cargoes being exchanged through each NPC every second (Ribbeck et al., 1998). In the past three decades, the key soluble factors that orchestrate NCT have been identified (Christie et al., 2016; Görlich and Kutay, 1999; Macara, 2001; Weis, 2003). Intensive efforts have also been devoted to understanding how these factors actively facilitate the speed, selectivity, and direction of NCT through the permeability barrier of the NPC (Stewart, 2007). These comprise members of the β-karyopherin family (collectively termed Kapβs), which include importins that usher diverse cargoes bearing nuclear localization signals (NLSs) into the nucleus (Boulikas, 1994; Cokol et al., 2000) and exportins, which escort cargoes bearing nuclear export signals (NESs) out of it (Fig. 1.1A) (Xu et al., 2012), (Baade and Kehlenbach, 2019). Additionally, certain Kapβs can exhibit both import and export functionalities (Twyffels et al., 2014). By convention, NES-containing cargoes are termed NES-cargos and NLS-containing cargoes are termed NLS-cargos. Another essential factor, the 25 kDa GTPase Ran, cooperates with Kapβs to regulate the delivery and accumulation of cargoes in an asymmetric, compartment-specific manner (Fig. 1.1B) (Görlich et al., 1996; Moore and Blobel, 1993).

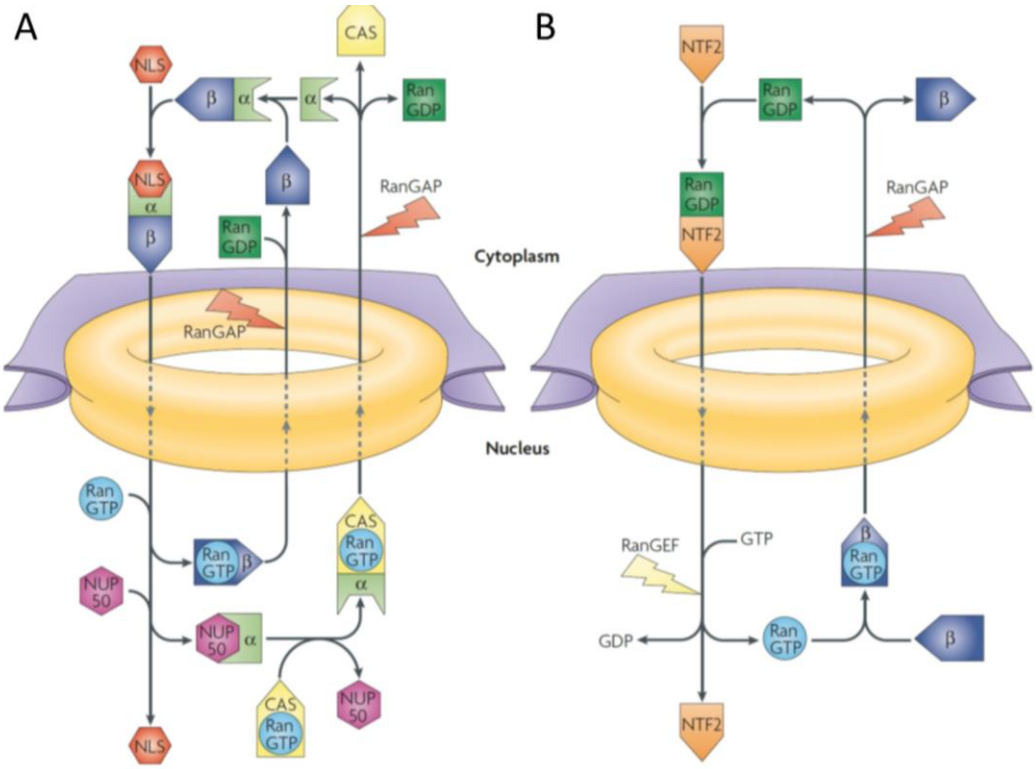

Figure 1.1 Mechanism of nucleocytoplasmic transport

(A) NLS-cargoes are selectively trafficked through the NPC by a major Kapβ, karyopherin beta 1 (Kapβ1; also known as importin-β) and its adaptor karyopherin α (Kapα also called importin-α). The binding of RanGTP to Kapβ1 within the nucleus leads to the disassembly of Kapβ1-Kapα and NLS-cargo release. The return of RanGTP-Kapβ1 to the nucleus is unimpeded by NPCs. This is followed by the hydrolysis of RanGTP to RanGDP by RanGAP, which frees Kapβ1 to undertake another import cycle. In comparison, the nuclear export of Kapα is facilitated by exportin 2 (cellular apoptosis susceptibility protein or CAS) and RanGTP. Upon exiting the NPC, the RanGTP-CAS-Kapα export complex disassembles in the cytoplasm following the hydrolysis of RanGTP by RanGAP. CAS is then free to return to the nucleus for another export cycle. The same mechanism applies generally to all Kapβs, except that Kapα binding is not required by importins other than Kapβ1. (B) The RanGTP/GDP cycle is tightly regulated by NTF2, RanGAP and RanGEF (RCC1). This generates a steep energy gradient across the NE that dictates the directionality of NCT. See text for more details. Scheme adapted from Stewart, 2007.

Ran-guanosine triphosphate (RanGTP) is ~200 times more highly concentrated (i.e., partitioned) in the nucleus than in the cytoplasm (Görlich et al., 2003; Kalab et al., 2002; Smith et al., 2002). During import, NLS-cargo–importin complexes entering the nucleus are disassembled upon binding of RanGTP to the respective importin (Fig. 1.1A) (Jäkel and Görlich, 1998). This serves to retain the NLS-cargo in the nucleus as the NPCs hinder its return to the cytoplasm. This stems from the presence of several intrinsically disordered proteins known as phenylalanine-glycine (FG)-rich Nups (FG Nups) that function as a permeability barrier in the central channel. At the same time, the binding of RanGTP–importin complexes to the FG-Nups facilitates their return to the cytoplasm. RanGTP is then hydrolyzed to RanGDP by SUMOylated RanGTPase-activating protein 1 (RanGAP1) together with Ran-binding protein 1

(RanBP1) and Ran-binding protein 2 (RanBP2, also known as Nup358) (Koyama and Matsuura, 2010; Lounsbury and Macara, 1997; Monecke et al., 2013; Vetter et al., 1999). Thereafter, RanGDP is freed from the importin, which is then able to undertake another cargo import cycle (Stewart, 2007). Similarly, GTP hydrolysis mediated by RanGAP1 disassembles ternary NES-cargo–exportin–RanGTP complexes to complete their nuclear exit (Fig. 1.1A). RanGDP is then recycled back to the nucleus by its specific carrier nuclear transport factor 2 (NTF2; also known as NUTF2) (Fig. 1.1B) (Ribbeck et al., 1998). The Ran loop is finally closed by the chromatin-bound enzyme regulator of chromosome condensation 1 (RCC1; also known as RanGEF), which recharges RanGDP to RanGTP (Fig. 1.1B) (Klebe et al., 1995; Renault et al., 2001; Ribbeck et al., 1998). As such, the Ran gradient regulates NCT directionality, cargo partitioning, and Kapβ recycling (Clarke and Zhang, 2008; Görlich et al., 1996; Izaurralde et al., 1997) using GTP as the energy source to power NCT. In this manner, NCT maintains essential functions within the nucleus and the cytoplasm without compromising the compositional integrity of either compartment (Terry et al., 2007).

1.2 NCT is impaired in aging and cellular pathologies

Importantly, NPC leakage and decreased NCT function are common pathological defects in neurodegeneration (Kim and Taylor, 2017) and viral infections (Yarbrough et al., 2014), while low expression levels of nucleoporins and Kapβs are observed in senescence (Kim et al., 2010). Likewise, the downregulation of RanBP17, an importin that is enriched within NPCs in neurons, has been linked to age-dependent disruption of nucleocytoplasmic compartmentalization (Mertens et al., 2015). Moreover, phosphorylated Tau protein in Alzheimer's disease (Eftekharzadeh et al., 2018) and mutant huntingtin in Huntington's disease (Grima et al., 2017) sequester and mislocalize FG Nups. A similar defect is observed in amyotrophic lateral sclerosis and frontotemporal dementia (ALS/FTD) (Hayes et al., 2020), where NCT is disrupted by sequestering Kapβs into cytoplasmic aggregates by TAR DNA-binding protein-43 (TDP-43)(Chou et al., 2018). NCT can be also impaired during viral pathogenesis. This concerns the degradation of FG Nups (Gustin and Sarnow, 2002; Watters and Palmenberg, 2011), or the inhibition of specific nuclear import pathways as is the case for SARS-CoV (Frieman et al., 2007) and SARS-CoV-2 (Miorin et al., 2020). Additionally, oxidative stress has been shown to affect NPC permeability as a consequence of increased proteolysis of Kapβs (Kodiha et al., 2004). Likewise, nuclear leakage has been discovered during postmitotic (chronological) cell

aging (D'Angelo et al., 2009; Rempel et al., 2019; Rempel et al., 2020). Lastly, NCT dysregulation is one of the hallmarks of carcinogenesis (Jans et al., 2019; Parikh et al., 2014).

1.3 Karyopherins (Kapβs) orchestrate NCT

Importins and exportins (O'Reilly et al., 2011) are major factors that control NCT (Table 1.1). As a point to note, Kapβs traverse NPCs with exquisite selectivity and speed that proceeds in a matter of milliseconds (Dange et al., 2008) by engaging in multivalent interactions with the FG Nups that reside in the inner channel of the NPC (Fig. 1.5) (Allen et al., 2001; Bayliss et al., 2000b; Davis et al., 2021; Kapinos et al., 2014; Port et al., 2015). Kapβs are evolutionarily clustered into 15 subfamilies and representatives of each subfamily can be found in all Eukaryotes (except for exportin-6/XPO6) (O'Reilly et al., 2011; Quan et al., 2008). Altogether, 20 Kapβs are known in vertebrates and 14 in *Saccharomyces cerevisiae* (Chook and Suel, 2011; Kimura and Imamoto, 2014). Limiting the number of cargoes assigned to each Kapβ reduces potential errors during NCT. Although all Kapβs can bind to their cargoes directly, the canonical import pathway regulated by importin Kapβ1 (also known as importin β1, KPNB1) relies on the formation of a heterodimeric complex consisting of Kapβ1- Kapα (Fig. 1.1A). In cells, Kapα is present in seven isoforms (KPNA1–KPNA7) and serves as a cargo adaptor that recognizes and binds to specific cargoes that harbor NLSs (Lange et al., 2007; Pumroy and Cingolani, 2015). Moreover, for the import of small nuclear ribonucleoproteins, Kapβ1 recruits snurportin-1 (SPN1, also known as SNUPN (Mitrousis et al., 2008). In both cases, SPN1 and Kapα bind to Kapβ1 through their N-terminal importin β-binding (IBB) domains (Lott and Cingolani, 2011).

1.3.1 Conformational flexibility of Kapβs

Secondary and tertiary structures of Kapβs are highly conserved (Neuwald and Hirano, 2000) across subfamilies and species (Conti et al., 2006), even though they exhibit low sequence homology (only 15-20% within the N-terminus) and interact with different binding partners. Kapβs comprise 19 to 21 consecutive HEAT (Huntingtin, elongation factor 3 (EF3), protein phosphatase 2A (PP2A), and the yeast kinase TOR1) repeats each formed by a pair of amphiphilic α-helices connected *via* a short linker. Thus, Kapβs constitute highly flexible right-handed solenoids that vary in curvature, diameter, and pitch (Fig. 1.2A) (Conti et al., 2006; Fukuhara et al., 2004). By this means, Kapβs exhibit a conformational versatility to bind to different ligands, such as NLS-cargoes, NES-cargoes, Kapα and RanGTP (Cingolani et al., 2000; Fukuhara et al., 2004; Kappel et al., 2010; Monecke et al., 2013; Port et al., 2015;

Yoshimura et al., 2014). Importantly, these structurally distinct partners interact with various binding sites of a given Kapβ causing allosterically propagated changes in the conformation of the entire molecule (Fig. 1.2B) (Cingolani et al., 2000; Cingolani et al., 1999; Fukuhara et al., 2004). Considering the high structural flexibility of Kapβs, supported by a variety of accessible crystal structures and SAXS studies (Fukuhara et al., 2004), it has been suggested that the known structures represent only snapshots from the continuum of conformations that Kapβs adapt *in vivo* (Kappel et al., 2010; Yoshimura et al., 2014; Zachariae and Grubmuller, 2008). In addition, adjacent HEAT motifs harbor several hydrophobic pockets that facilitate multivalent binding interactions with FG-repeats (Bayliss et al., 2000a; Davis et al., 2021; Isgro and Schulten, 2005; Port et al., 2015). Taken together, this suggests that the binding avidity (i.e., the apparent binding affinity of a multivalent molecule) of Kapβs to FG-Nups may depend on the resulting conformation that each respective Kapβ adopts during cargo-loading.

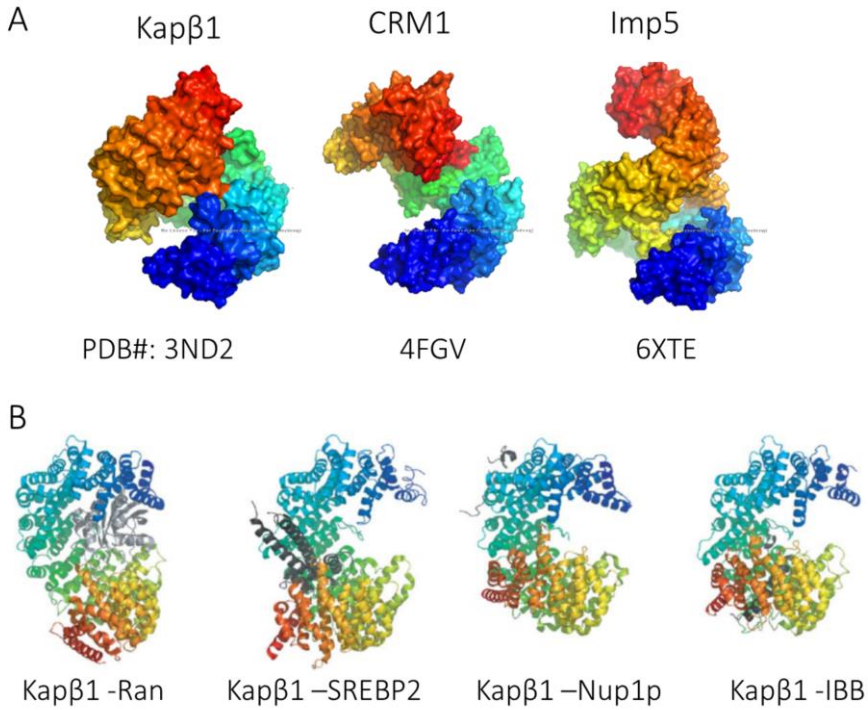

Figure 1.2 Structure and conformational flexibility of Kapβs

(A) Crystal structures of Kapβ1, CRM1, and Imp5. Despite significant differences in amino acid sequences, all Kapβs form flexible right-handed solenoids of different geometrical parameters. The convex surface of each Kapβ contains multiple FG motif-binding pockets that promote their multivalent and promiscuous interactions with the FG Nups. (B) The structure of a given Kapβ fluctuates depending on the binding partner. All Kapβs crystal structures are colored from blue (N-terminus) to red (C-terminus). Interacting molecules (Ran, SREBP2 (Sterol Regulatory Element Binding Transcription Factor 2), Nup1p, IBB (Importin β binding domain)) are shown in grey. Panel (B) adapted from Conti et al., 2006.

1.3.2 Kapβ transport kinetics within NPCs

Depending on the carried cargo, the dwell times of Kapβs in the NPC range between 5 and 20 ms (Kubitscheck et al., 2005; Tu et al., 2013; Yang et al., 2004) but can reach 180 ms for mRNA (Grünwald and Singer, 2010). Interestingly, higher concentrations of Kapβ1 enhances cargo transport efficiency through the NPC and decreases cargo dwell times (Yang and Musser, 2006). The latter might be due to a reduction of available FG repeats and the frequency of their interactions with individual Kapβs (Kapinos et al., 2017; Kapinos et al., 2014; Lowe et al., 2015; Schleicher et al., 2014; Wagner et al., 2015). Nevertheless, import cargo dwell times also depend on the binding of RanGTP to importins and are not *a priori* equivalent to Kapβ residence times. Thus, successful import depends on the accessibility of RanGTP to importin–cargo complexes on the nuclear side of the NPC, whereas successful export depends on GTP hydrolysis by RanGAP1 on the cytoplasmic side (Fig. 1.1).

Within the NPC, Kapβ complexes exhibit Brownian diffusion that is facilitated by interactions with the FG-repeats, also termed facilitated diffusion, which seems to expedite their translocation through the central channel (Cardarelli et al., 2011; Yang et al., 2004). However, whether and how the crowding of Kapβs within the NPC affects their kinetic interactions with the FG-Nups and their dynamic movements within the pore remains unclear. To gain a physical understanding of such effects, the behavior of Kapβ1-functionalized colloidal beads was studied on surface-tethered FG-Nup layers. The beads transitioned from being immobile to exhibiting two-dimensional diffusion when the amount of soluble Kapβ1 was raised from low to physiologically relevant concentrations, which resulted in an enrichment of soluble Kapβ1 within the FG-Nup layer (Schleicher et al., 2014). In contrast, non-specific control beads exhibited three-dimensional diffusion that transiently impinged on the FG-Nup layer without binding (Schleicher et al., 2014). This demonstrates that fast and selective transport can be achieved when FG Nups are saturated with Kapβ molecules, as observed *in vivo* (Chapter 2). Nevertheless, it remains to be determined how Kapβ complexes can exhibit rapid movements in the NPC while reinforcing the permeability barrier at the same time.

1.3.3 Variety of Kapβ cargoes

Numerous NLSs and NESs greatly expand the repertoire of cargoes being recognized by each Kapβ (Fig. 1.3) (Table 1.1). The best -characterized 'classical' nuclear import pathway consists of NLS-cargoes that typically form transport complexes with Kapα–Kapβ1, that is

NLS-cargo–Kapα–Kapβ1 (Fig. 1.1A) (Lange et al., 2007). Classical NLSs harbor multiple lysine (K) and arginine (R) residues as exemplified by the NLS of monopartite SV40 T-antigen (^{126}PKKKRRV^{132}) (Kalderon et al., 1984; Kosugi et al., 2009; Lange et al., 2007) or the bipartite NLS of nucleoplasmin (^{155}KRPAATKKAGQAKKKK^{170}) (Lange et al., 2007; Robbins et al., 1991). Nevertheless, substantial sequence variations exist across NLSs (Boulikas, 1994) that utilize the Kapα–Kapβ1 complex (Kosugi et al., 2009) and those that directly bind to Kapβ1 (Cokol et al., 2000; Lee et al., 2003). Some cargoes, such as myocardin-related transcription factors (MRTFs) (Pawlowski et al., 2010) may even harbor individual NLSs that are recognized by different Kapα isoforms (Goldfarb et al., 2004), although with varying affinities (Friedrich et al., 2006; Pumroy and Cingolani, 2015). Certain cargoes can contain multiple NLSs which associate with different Kapαs or Kapβs, for instance, hypoxia-inducible factors (HIFs) (Chachami et al., 2009; Depping et al., 2008). Other Kapβs such as transportin 1 (also termed Kapβ2) recognize cargoes *via* a consensus NLS-motif that contains proline (P) and tyrosine (Y) residues (termed PY-NLS cargoes (Lee et al., 2006). In terms of exportins, chromosomal maintenance 1 (CRM1; also known as exportin 1, Exp1, or Xpo1) recognizes a consensus leucine-rich NES (ϕ-$X_{2–3}$-ϕ-$X_{2–3}$-ϕ-X-ϕ, where ϕ is Lys, Val, Ile, Phe or Met, X is any amino acid, and the numbers denote the number of repeats) (Dong et al., 2009; Kosugi et al., 2014). This clearly indicates that NLSs and NESs are diverse and that not all comply with consensus motifs (Cokol et al., 2000).

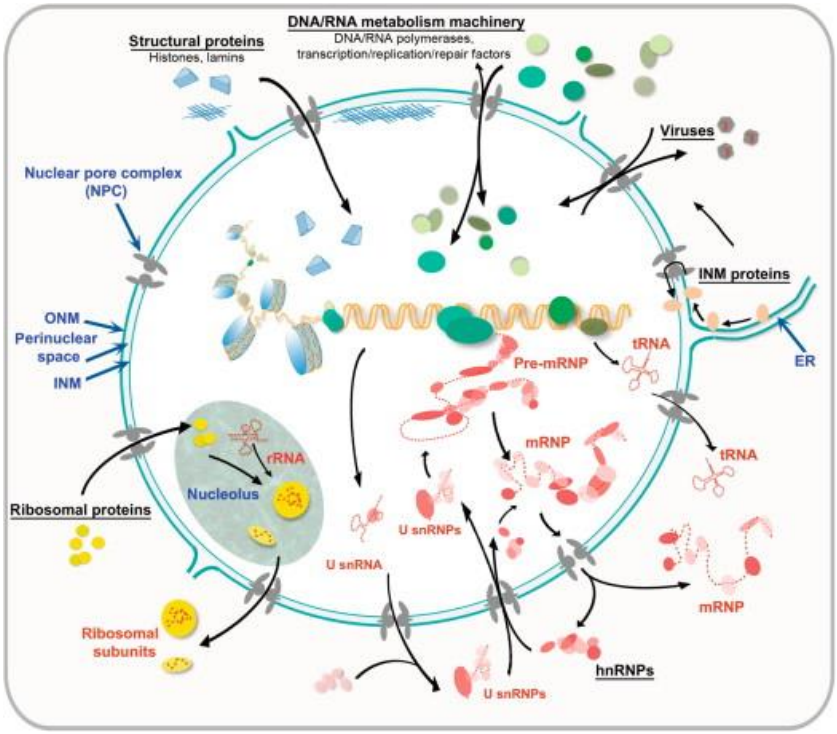

Figure 1.3 Diversity of NCT and cargoes

Overview of the cargoes that require NCT for proper localization and cellular functioning. Figure adapted from Floch et al., 2014.

Table 1.1 Function and cellular localization of Kapβs

Vertebrate	Yeast	Function in NCT/cargos	References (Kapβ function)	Cellular localization*	References (IF data)**
Nuclear import					
Kapβ1 (KPNB1)	KAP95	Import of IBB, NLS-cargo and Kapα isoforms	(Chi, Adam et al. 1995, Görlich, Vogel et al. 1995)	C/NE	(Mingot, Kostka et al. 2001, Guttinger, Muhlhausser et al. 2004)
Imp4 (IPO4, RANBP4, IMP4B)	KAP123	Import of histone H3/H4·Asf1a complex, ribosomal protein S3a, the vitamin D receptor, hypoxia Inducible factor-α, epididymis protein4	(Yoon, Kim et al. 2018)	C	n.d.
Imp5 (IPO5, RANBP5, IMP5B)	KAP121	Import of ribosomal proteins, such as RPL23A (17.7 kDa), RPS7 (17.7 kDa) and RPL5 (34.4 kDa), and histones: H2A (14 kDa), H2B (14 kDa), H3 (11.4 kDa) and H4 histones (11.4 kDa)	(Jäkel and Görlich 1998)	C	(Guttinger, Muhlhausser et al. 2004, Spits, Janssen et al. 2019, Zhang, Lu et al. 2019)
Imp7 (IPO7, RANBP7)	KAP114	Import of ribosomal proteins (RPL23A, RPS7 and RPL5) and histones (H1, H2A, H2B, H3 and H4) together with Kapβ1	(Jäkel and Görlich 1998)	C/NE	(Görlich, Dabrowski et al. 1997, Mingot, Kostka et al. 2001, Wei, Li et al. 2014)
Imp8 (IPO8, RANBP8)	KAP120	Import of SRP19 (signal recognizing particle 19)	(Dean, von Ahsen et al. 2001)	C/NE	(Görlich, Dabrowski et al. 1997, Wei, Li et al. 2014, Hu, Kan et al. 2018)
Imp9 (IPO9*, IMP9, KIAA1192, RANBP9, HSPC273)	KAP114	Import of ribosomal proteins (RPS7, RPL18A (20.8 kDa), RPL6 (32.7 kDa)), histones (H2A, H2B) and actin (by similarity); Prevents the cytoplasmic aggregation of RPS7 and RPL18A by shielding exposed basic domains	(Jäkel and Görlich 1998)	C	(Guttinger, Muhlhausser et al. 2004, Padavannil, Sarkar et al. 2019)
Imp11 (IPO11, RANBP11)	KAP120	Import of UBE2E3 and RPL12	(Strambio-De-Castillia, Niepel et al. 2010)	N	(Plafker and Macara 2000)
Transportin-2 (Kapβ_2B, TNPO2)	KAP104	Import of NLS-cargos (by similarity) / n.d.	(Gaudet, Livstone et al. 2011)	N	(Guttinger, Muhlhausser et al. 2004)
Transportin-3 (Imp12, TNPO3, IPO12, TNP-SR)	-	Import of splicing factor SR proteins RBM4, SFRS1 and SFRS2 (recognized by phosphorylated RS domains, i.e. *arginine-serine rich domains*).	(Lai, Lin et al. 2001, Lai, Kuo et al. 2003, Maertens, Cook et al. 2014)	n.d.	n.d.

Nuclear export					
Exp1 (CRM1, XPO1)	CRM1	Export of NES cargos	(Fornerod, Ohno et al. 1997, Ossareh-Nazari, Bachelerie et al. 1997, Stade, Ford et al. 1997, Haasen, Kohler et al. 1999)	N/NE	(Stade, Ford et al. 1997)
Exp2 (**CAS**, XPO2, CSE1L)	CSE1	Export of Kapα	(Kutay, Bischoff et al. 1997)	N	(Kutay, Bischoff et al. 1997)
Exp4 (XPO4 KIAA1721)	-	Export of Smad3	(Boulikas 1994, Cokol, Nair et al. 2000)	N	(Lipowsky, Bischoff et al. 2000)
Exp5 (XPO5, RANBP21)	MSN5	Export of micro-RNA precursors, synthetic short hairpin RNAs and specific dsRNAs	(Allen, Huang et al. 2001, Gwizdek, Ossareh-Nazari et al. 2004, Lund, Guttinger et al. 2004, Yi, Doehle et al. 2005, Okada, Yamashita et al. 2009, Xu, Farmer et al. 2012)	N	n.d.
Exp6 (XPO6, KIAA0370, RANBP20)	-	Export of actin and profilin-actin complexes in somatic cells	(Görlich, Seewald et al. 2003)	n.d.	n.d.
Exportin-T (XPOT)	LOS1	Export of tRNA	(Kutay, Lipowsky et al. 1998, Kuersten, Arts et al. 2002)	N	(Kuersten, Arts et al. 2002)
Bidirectional transport (import and export)					
Transportin-1 (TNPO1, KPNB2, MIP1, TRN)	KAP104	Import of M9-containing proteins; Binds to a beta-like import receptor binding (BIB) domain. Export of hnRNP A1/A2	(Arnold, Nath et al. 2006, O'Reilly, Dacks et al. 2011)	N	(Siomi, Eder et al. 1997, Guttinger, Muhlhausser et al. 2004)

Imp13 (IPO13* (KIAA0724, RANBP13)	MTR10	Import of UBC9, the RBM8A/MAGOH complex, PAX6; Export of eIF-1A (release is triggered by IPO13)	(Mingot, Kostka et al. 2001, Ploski, Shamsher et al. 2004)	C/nucleoli	(Mingot, Kostka et al. 2001)
Exp7 (XPO7, KIAA0745, RANBP16)	KAP123	Export of approx. 200 cargos, e.g. RhoGAP1 and 14-3-3 σ, α- and β-tubulin, and import of approx. 30 cargos	(Bayliss, Littlewood et al. 2000, Aksu, Pleiner et al. 2018)	n.d.	n.d.
Ran-binding protein 17 (RANBP17)	-	May function as a transporter (by similarity)	-	n.d.	n.d.
-	**sal3**	Import of Cdc25	(Chua, Lingner et al. 2002)	n.d.	n.d.

*Based on immunofluorescence (IF) data; **See also Human Cell Atlas: https://www.proteinatlas.org/humanproteome/cell

Abbreviations:

N - nucleus; C – cytoplasm; NE – nuclear envelope (i.e. localization at the NPCs); n.d. –no data;

Recommended protein names and abbreviations for vertebrate transport receptors: Kapβ1 - karyopherin beta-1, Imp4 - importin-4, Imp5 - importin-5, Imp7 - importin-7, Imp8 – importin-8, Imp9 - importin-9, Imp11 - importin-11, Imp13 – importin-13, Exp1 - exportin-1, Exp2 - exportin-2, Exp4 - exportin-4, Exp5 - exportin-5, Exp6 - exportin-6, Exp7 - exportin-7. See the UniProtKB database (see https://www.uniprot.org/uniprot) for alternative protein names and gene names as indicated in the brackets.

For simplicity, yeast transport receptors are listed by gene name: KAP95 - karyopherin 95, KAP104 - karyopherin 104, KAP114 - karyopherin 114, KAP120 - karyopherin 120, KAP121 - karyopherin 121, KAP123 - karyopherin 123, CRM1 - chromosome region maintenance protein 1, CSE1 - chromosome segregation protein1, MSN5 - Protein MSN5, LOS1 - loss of suppression, MTR10 - mRNA transport defective 10; sal3 - Importin subunit beta-3.

1.4 The Nuclear Pore Complex

NPCs are massive complexes (~60 MDa in yeast (Rout and Blobel, 1993), ~110-125 MDa in *Xenopus laevis* (Reichelt et al., 1990)) that span across the NE and exert the primary means of control over NCT as the exclusive sites of nucleocytoplasmic exchange (Fig. 1.4). Each NPC is assembled from multiple copies of ~30 proteins known as nucleoporins (Nups) (Fig 1.5) (Cronshaw et al., 2002; Rout et al., 2000) that surround an aqueous central channel measuring ~40–60 nm in diameter (Eibauer et al., 2015; Kim et al., 2018; von Appen et al., 2015).

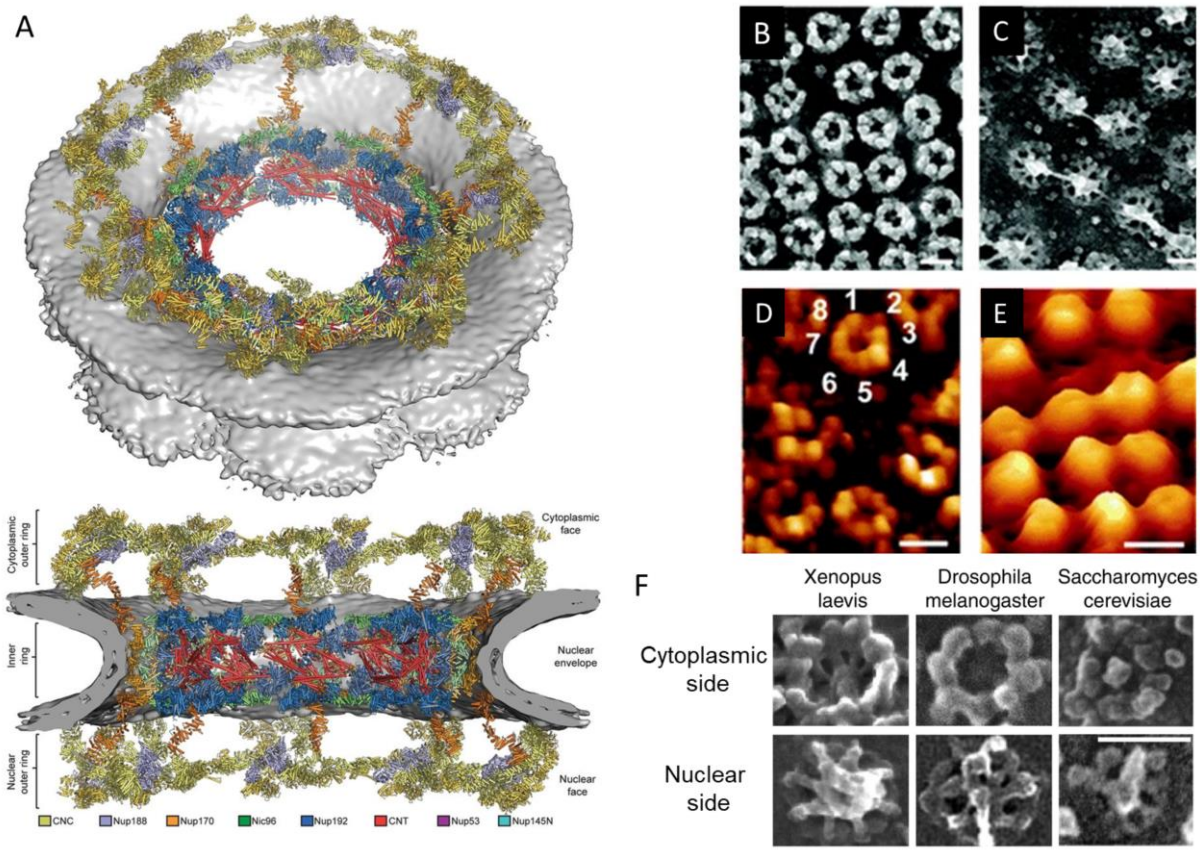

Figure 1.4 Overall structure of the NPC.

(A) Cryo-EM reconstruction of the NPC symmetric core. Top, detailed view of the cytoplasmic face; bottom, a cross-section of the NPC showing specific sub-structures. NE is shown in grey; proteins are color-coded according to the attached key. Reproduced from Lin et al., 2016. Transmission Electron Microscopy (TEM) images of cytoplasmic (B) and nuclear (C) sides of the NPCs embedded in the NE. The density distribution of the NPCs as well as the differences in the morphology of both NPC sides are clearly visible. Cytoplasmic (D) and nuclear (E) surfaces of the NPC as visualized by the Atomic Force Microscopy (AFM). Numbers in (D) indicate eight, rotationally symmetrical NPC sub-domains. Modified from (Lim et al., 2006). Scanning Electron Microscopy (SEM) micrographs of NPCs from various eukaryotes (F). The characteristic cytoplasmic and nuclear surface features are conserved across the species, as is the octagonal symmetry. Adapted from Brohawn et al., 2009.

Interestingly, only about 50% of the Nups by mass form structured domains, while the other half consists of FG-Nups (Fig. 1.5) (Wente and Rout, 2010). Despite differences in the copy number of Nups and NPC size across species, NPC's triple-ring structure with eight-fold symmetry is highly conserved (Fig. 1.4B-F) (Brohawn et al., 2009; Cronshaw et al., 2002). The following architectural sub-structures can be distinguished within each NPC (Fig. 1.5):

A) The cytoplasmic ring is formed by peripheral filamentous structures and consists of FG-rich Nups (in vertebrates Nup214, Nlp1, and Nup358 (RanBP2) (Fig. 1.4B, D, F and 1.5) (Grossman et al., 2012; Sakiyama et al., 2016). This NPC substructure is involved in e.g., docking of Kapβs (Sabri et al., 2007), RanGTP-cycle, and initiation of translation (Strambio-De-Castillia et al., 2010).

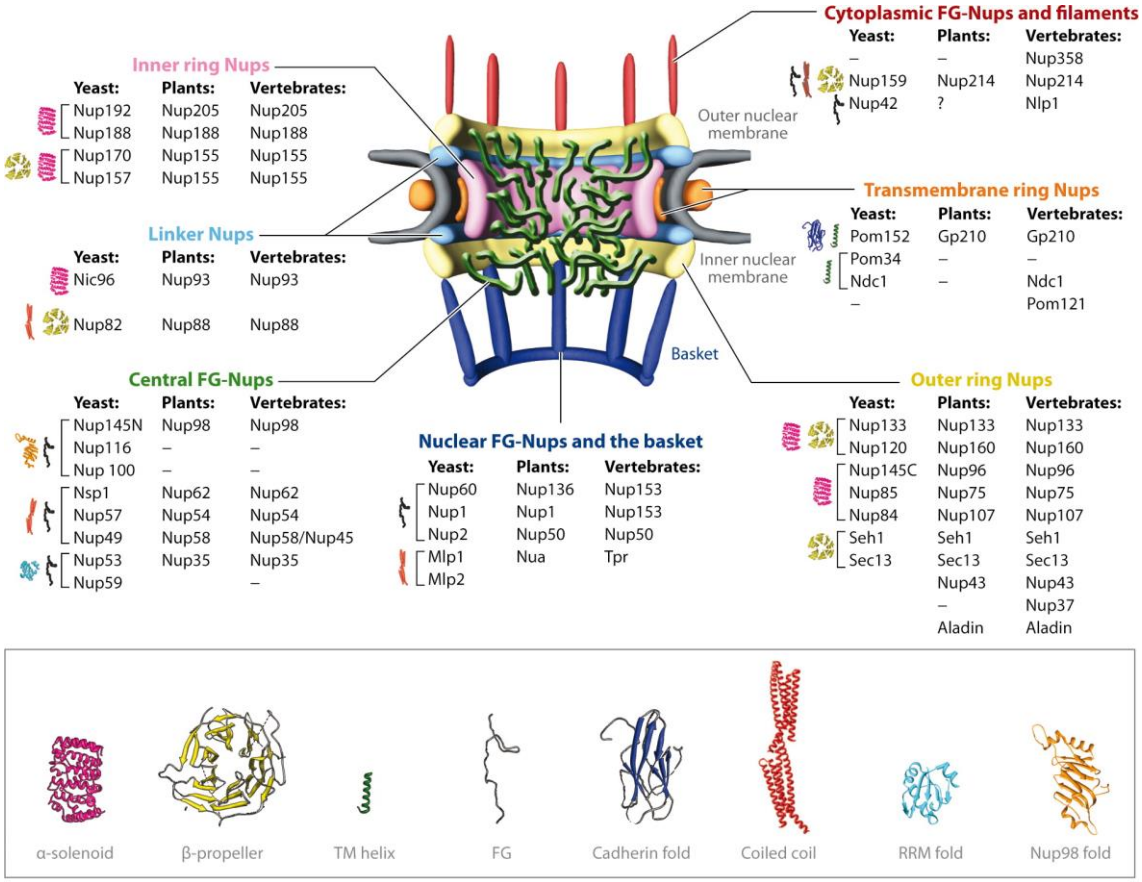

Figure 1.5 Diversity and localization of nucleoporins (Nups) within the NPC.

Structural components of the NPC, i.e., Nups grouped by their structural features and location. The inner core consists of symmetrically distributed outer ring Nups, transmembrane Nups, linker Nups, inner ring Nups, and FG Nups in the center. Nups and FG Nups that assemble into the nuclear basket and cytoplasmic ring are asymmetrically distributed along the main NPC axis. NE is shown in grey; the depictions of the predicted structural motifs are shown next to each Nup and explained in the legend. Figure reproduced from Grossman et al., 2012.

B) The nuclear ring consists of eight filaments formed by FG Nups (Nup153 and Nup50) and nucleoporin Trp (Beck et al., 2007; Grossman et al., 2012; Lim and Fahrenkrog, 2006). They extend into the nucleoplasm and fuse into the so-called nuclear basket (Fig. 1.4C, E, F, and 1.5) which is an interaction site for Kapβs (Sabri et al., 2007).

C) The central (inner) ring is located between two rings described above (Beck et al., 2004; Beck et al., 2007). This part is built from the inner ring Nups that form the structural core, transmembrane Nups that ensure NPC anchoring to the NE (Antonin et al., 2008), linker Nups that provide the physical connection between central and outer rings, and lastly, central FG Nups (Fig. 1.4 and Fig. 1.5) that are involved in transport selectivity and contribute to the prevention of the unrestricted mixing between nucleus and cytoplasm (Grossman et al., 2012; Strambio-De-Castillia et al., 2010).

1.5 Nature of the permeability barrier

Each NPC is equipped with ~200 FG-Nups that are thought to function as a filter-like permeability barrier that permits small molecules below ~40 kDa (or 5 nm in diameter) to passively diffuse through the NPC while suppressing the passage of larger non-specific cargoes, which are not recognized by Kapβs (Paine et al., 1975; Popken et al., 2015; Timney et al., 2016). Nevertheless, up to 50% of FG Nups can be deleted *in vivo* without a noticeable impact on NPC permeability (Strawn et al., 2004). However, the exact form of the NPC permeability barrier remains unclear (Huang and Szleifer, 2020; Lemke, 2016). This is due in part to the inherent flexibility and dynamic fluctuations of the FG-Nups (Sakiyama et al., 2016) which precludes structural characterization within NPCs. Consequently, NPC barrier models have mainly derived from studies with purified FG Nups whose behavior can vary depending on length scale and experimental design (See Chapter 1.4) (Hoogenboom et al., 2021). This ranges from tethered molecular layers (Eisele et al., 2012; Eisele et al., 2010; Kapinos et al., 2014; Schleicher et al., 2014; Schoch et al., 2012; Zahn et al., 2016), liquid droplets (Celetti et al., 2020), and gel-like (Frey et al., 2018; Schmidt and Görlich, 2015) to more solid-like hydrogels (Frey and Görlich, 2007, 2009; Milles et al., 2013). Findings provided by these studies motivated the formulation of multiple permeability barrier models:

A) The Selective Phase Model

This model assumes that the FG Nups form a sieve-like meshwork (hydrogel) established by their cohesive interactions (Fig. 1.6A) (Ribbeck and Görlich, 2001). Kapβs, by directly binding

to the FG repeats and dissolving the cross-links, can penetrate the barrier, while the permeation of unspecific cargos is restricted. However, this model does not account for distinct transport routes observed for Kapβ-dependent and passively diffusing cargoes (Hülsmann et al., 2012). Additionally, a saturation of the hydrogel with Kapβs hinders the motility of Kapβ-cargo complexes (Frey and Gorlich, 2009) which contradicts the finding that Kapβs saturation expedites transport rates (Schleicher et al., 2014; Yang and Musser, 2006).

B) Polymer Brush Model

Here, the FG Nups form a surface-tethered brush with extended conformations (Fig. 1.6B) (Lim et al., 2007). This is due to the small grafting distance of their anchoring points (i.e., surface density), which consequently leads to the size-exclusion and thus extension of FG Nups (Milner, 1991). Therefore, at the NPC periphery, FG Nups may form an entropic barrier that stops unsolicited entry, while Kapβs are allowed because of their direct interactions with FG Nups (Lim et al., 2006). However, such binding also causes a reversible collapse of the FG Nups which brings Kapβs and their complexes into the pore. The subsequent change of the Kapβ binding site releases previously occupied FG Nups and their re-extension, while newly bound FG Nups collapse. Since the relaxation of disordered domains is reversible and fast, the integrity of the entropic barrier is maintained (Chattopadhyay et al., 2005). Moreover, the conformational change of FG Nups may explain the Kapβ-dependent transport path along the NPC wall. However, this model is based on experiments that were performed below physiological Kapβ concentrations, while more recent studies show that the FG Nups collapse is rescued by increasing receptors concentration (Schoch et al., 2012).

C) Reduction of Dimensionality Model (ROD)

The ROD model is founded on the observation that FG Nups collapse upon Kapβ binding (Fig. 1.6C) (Peters, 2005). Thus, the NPC-anchored FG Nups would occupy a permanently collapsed state under saturating Kapβ conditions *in vivo* (Chapter 2.2) (Peters, 2009a; Peters, 2009b). As such, FG Nups create a hydrophobic lining of NPC, to which Kapβs can bind (Peters, 2009a). In the ROD model, Kapβs translocation along NPC is ensured by their transient multivalent interactions with FG Nups, however, their motility is restricted to a two-dimensional random walk. On the other hand, the movement of non-specific cargoes would resemble a three-dimensional

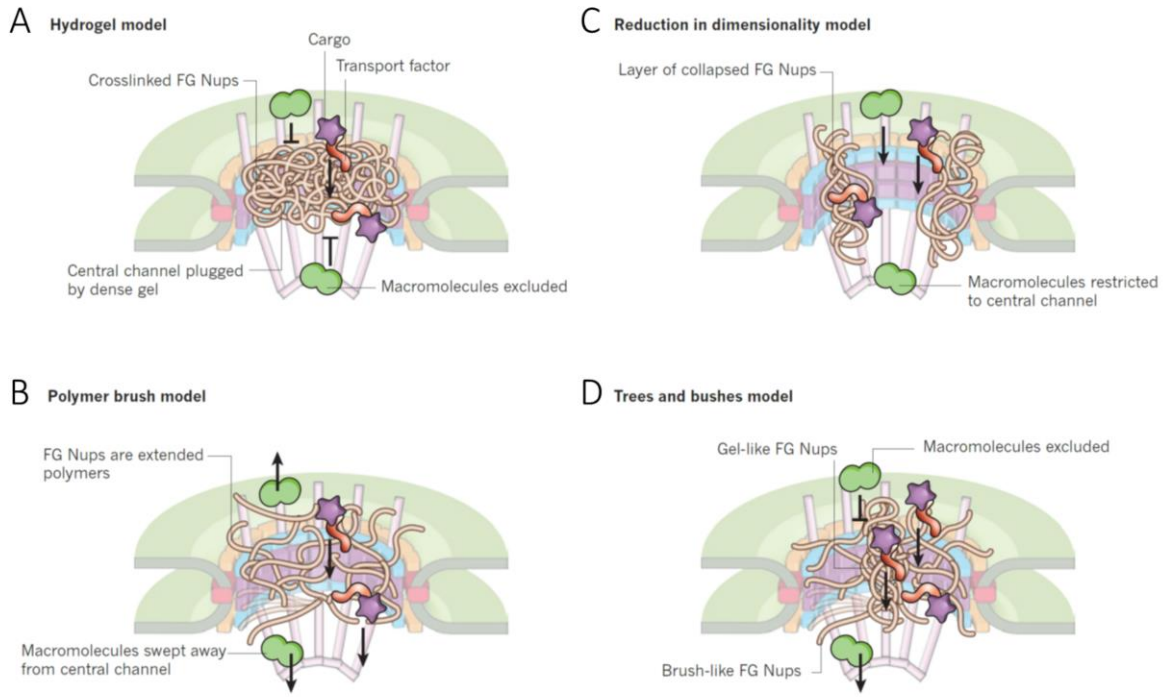

Figure 1.6 Models of NPC selective barrier.

(A) In the hydrogel model, FG Nups located in the central channel of the NPC form a gel-like meshwork that can be dissolved by the transport receptors due to their direct binding to the FG Nups. Non-specific molecules are halted by means of size exclusion. (B) The small grafting distance of FG Nups tethered at the NPC walls causes their extension and formation of a brush-like structure. Non-specific cargoes are entropically excluded from the translocation, while NCT factors bind to the FG Nups causing their reversible collapse. (C) Reduction of dimensionality envisions collapsed FG Nups as a sort of molecular velcro lining the NPC's inside walls. Here, NCT components slide along the FG Nups to which they can bind, while other molecules translocate through the middle of the pore, exploring the entire available volume (3D diffusion). (D) Forrest (trees and bushes model) assumes FG Nups in two conformational states, collapsed (gel-like) and extended (brush-like). In this model, Kapβs and their complexes translocate through both types of assemblies, while non-specific cargoes are more inclined to pass through the less dense regions. Figure adapted from Grünwald et al., 2011.

diffusion restricted by a narrow tube, i.e., NPC's inner channel. Moreover, this interpretation accounts for the observation that Kapβs seem to travel along the NPC walls, while non-specific cargoes are mostly found in the central channel (Ma et al., 2012).

D) Forest Model

In this model, three different conformations of the FG Nups are considered, namely (i) globular collapsed coil (cohesive), (ii) extended coil (non-cohesive), and (iii) FG Nups which combine both of the aforementioned conformations, thus approximated as the canopy and trunk of a tree (Fig. 1.6D) (Yamada et al., 2010). This approximation allows for conceptual separation of the NPC into two different regions: the central one surrounded by the cohesive 'canopies' that form a gel-like structure, and the peripheral one created

by the ''trunks' that are more brush-like (see "Polymer Brush Model"), but lined with shrubs (i.e., more cohesive FG Nups). As such, the model permits diffusion of non-specific cargo through both regions, while large, Kapβ-dependent cargoes travel along the central zone. Finally, the translocation of standalone Kapβs or their complexes with small cargoes proceeds through the peripheral region which acts as an entropic barrier. These assumptions, however, contradict experimental observations which show preferential localization of small non-specific cargos in the NPC's central channel (Hülsmann et al., 2012).

Regardless of the exact nature of the NPC permeability barrier, the role of the NPCs *in vivo* is to prevent unsolicited mixing between nucleus and cytoplasm, while favoring delivery of specific cargoes. However, studies have shown that NPCs lack a defined threshold for passively diffusing cargoes. Rather, its filtering ability can be described as a soft barrier that increases progressively as the molecular weight of the cargo increases (Timney et al., 2016). As such, cargoes larger than 60 kDa can diffuse across the NPC and equilibrate between compartments if given enough time (Popken et al., 2015; Wühr et al., 2015). Although the molecular mass seems to have the biggest impact on limiting passive translocation of cargoes, a recent study has demonstrated that surface properties of molecules can explain leakage of large cargoes and complexes into the nuclei (Frey et al., 2018). Therefore, one should consider how specific cargoes influence their own transport rates.

1.6 Aim of the Thesis

Over the last decade, our understanding of the NPC permeability barrier has evolved from models that rely almost exclusively on the properties of the FG Nups, to being perceived as a dense phase of Kapβs mixed with FG Nups and water (i.e., mixed ternary phase) (Kapinos et al., 2017; Kapinos et al., 2014; Lim et al., 2015; Schleicher et al., 2014; Schoch et al., 2012; Zilman, 2018). This so-called 'Kap-centric model' stipulates that although FG Nups are essential for establishing the permeability barrier, its complete functionality is achieved in cooperation with Kapβs. In this manner, the Kap-centric model addresses the mechanistic and kinetic aspects of the NPC barrier (see Chapter 2.2).

The cellular studies reported in this thesis reveal that certain Kapβs, specifically Kapβ1 and CRM1, display a distinct steady-state localization at the NE. This signifies that their binding to FG Nups facilitates their enrichment at the NPCs (Kalita et al., 2021) (Fig. 2.1 and Fig. 2.3).

The objective of this thesis is to investigate whether, how, and to what extent Kapβ1 and CRM1 regulate NPC barrier function in comparison to other Kapβs, such as Importin-5 (Imp5). Additionally, we aim to examine the ability of different Kapβs to co-exist at the NPC and the extent of their mutual influence on the occupancy of certain Kapβs. By experimenting across biophysical, *ex vivo,* and *in vivo* regimes, we show that Kapβ1 and CRM1 are essential for fortifying the NPC barrier against defective NCT and nuclear leakage *in vivo.* We demonstrate that other Kapβs are prone to displacement by Kapβ1 and CRM1 as a result of their faster dissociation rate from the FG Nups, as evidenced for Imp5. Taken together, our work sheds light on how Kapβ enrichment at the NPC is constrained by their size, cellular abundance, FG Nup binding affinity, and competition with other Kapβs. Finally, evidence of increased NPC permeability and nuclear leakage of both specific- and non-specific cargoes upon Kapβ1 reduction is presented. The experimental results described in this thesis show that Kapβ1 and CRM1 engage in a balancing act to reinforce NPC barrier function.

1.7 References

Aksu, M., Pleiner, T., Karaca, S., Kappert, C., Dehne, H.J., Seibel, K., Urlaub, H., Bohnsack, M.T., and Gorlich, D. (2018). Xpo7 is a broad-spectrum exportin and a nuclear import receptor. J Cell Biol *217*, 2329-2340.

Allen, N.P.C., Huang, L., Burlingame, A., and Rexach, M. (2001). Proteomic analysis of nucleoporin interacting proteins. J Biol Chem *276*, 29268-29274.

Antonin, W., Ellenberg, J., and Dultz, E. (2008). Nuclear pore complex assembly through the cell cycle: regulation and membrane organization. FEBS Lett *582*, 2004-2016.

Arnold, M., Nath, A., Wohlwend, D., and Kehlenbach, R.H. (2006). Transportin is a major nuclear import receptor for c-Fos: a novel mode of cargo interaction. J Biol Chem *281*, 5492-5499.

Baade, I., and Kehlenbach, R.H. (2019). The cargo spectrum of nuclear transport receptors. Curr Opin Cell Biol *58*, 1-7.

Bayliss, R., Kent, H.M., Corbett, A.H., and Stewart, M. (2000a). Crystallization and initial X-ray diffraction characterization of complexes of FxFG nucleoporin repeats with nuclear transport factors. J Struct Biol *131*, 240-247.

Bayliss, R., Littlewood, T., and Stewart, M. (2000b). Structural basis for the interaction between FxFG nucleoporin repeats and importin-beta in nuclear trafficking. Cell *102*, 99-108.

Beck, M., Forster, F., Ecke, M., Plitzko, J.M., Melchior, F., Gerisch, G., Baumeister, W., and Medalia, O. (2004). Nuclear pore complex structure and dynamics revealed by cryoelectron tomography. Science *306*, 1387-1390.

Beck, M., Lucic, V., Forster, F., Baumeister, W., and Medalia, O. (2007). Snapshots of nuclear pore complexes in action captured by cryo-electron tomography. Nature *449*, 611-615.

Boulikas, T. (1994). Putative nuclear-localization signals (NLS) in protein transcription factors. J Cell Biochem *55*, 32-58.

Brohawn, S.G., Partridge, J.R., Whittle, J.R.R., and Schwartz, T.U. (2009). The Nuclear Pore Complex Has Entered the Atomic Age. Structure (London, England : 1993) *17*, 1156-1168.

Cagatay, T., and Chook, Y.M. (2018). Karyopherins in cancer. Curr Opin Cell Biol *52*, 30-42.

Cardarelli, F., Lanzano, L., and Gratton, E. (2011). Fluorescence correlation spectroscopy of intact nuclear pore complexes. Biophys J *101*, L27-29.

Celetti, G., Paci, G., Caria, J., VanDelinder, V., Bachand, G., and Lemke, E.A. (2020). The liquid state of FG-nucleoporins mimics permeability barrier properties of nuclear pore complexes. J Cell Biol *219*.

Chachami, G., Paraskeva, E., Mingot, J.M., Braliou, G.G., Gorlich, D., and Simos, G. (2009). Transport of hypoxia-inducible factor HIF-1 alpha into the nucleus involves importins 4 and 7. Biochem Biophys Res Commun *390*, 235-240.

Chattopadhyay, K., Elson, E.L., and Frieden, C. (2005). The kinetics of conformational fluctuations in an unfolded protein measured by fluorescence methods. Proceedings of the National Academy of Sciences of the United States of America *102*, 2385-2389.

Chi, N.C., Adam, E.J.H., and Adam, S.A. (1995). Sequence and characterization of cytoplasmic nuclear-protein import factor p97 J Cell Biol *130*, 265-274.

Cho, U.H., and Hetzer, M.W. (2020). Nuclear Periphery Takes Center Stage: The Role of Nuclear Pore Complexes in Cell Identity and Aging. Neuron *106*, 899-911.

Chook, Y.M., and Suel, K.E. (2011). Nuclear import by karyopherin-betas: recognition and inhibition. Biochim Biophys Acta *1813*, 1593-1606.

Chou, C.C., Zhang, Y., Umoh, M.E., Vaughan, S.W., Lorenzini, I., Liu, F., Sayegh, M., Donlin-Asp, P.G., Chen, Y.H., Duong, D.M.*, et al.* (2018). TDP-43 pathology disrupts nuclear pore complexes and nucleocytoplasmic transport in ALS/FTD. Nat Neurosci *21*, 228-+.

Christie, M., Chang, C.W., Rona, G., Smith, K.M., Stewart, A.G., Takeda, A.A., Fontes, M.R., Stewart, M., Vertessy, B.G., Forwood, J.K.*, et al.* (2016). Structural biology and regulation of protein import into the nucleus. J Mol Biol *428*, 2060-2090.

Chua, G., Lingner, C., Frazer, C., and Young, P.G. (2002). The sal3(+) gene encodes an importin-beta implicated in the nuclear import of Cdc25 in Schizosaccharomyces pombe. Genetics *162*, 689-703.

Cingolani, G., Lashuel, H.A., Gerace, L., and Muller, C.W. (2000). Nuclear import factors importin alpha and importin beta undergo mutually induced conformational changes upon association. FEBS Lett *484*, 291-298.

Cingolani, G., Petosa, C., Weis, K., and Muller, C.W. (1999). Structure of importin-beta bound to the IBB domain of importin-alpha. Nature *399*, 221-229.

Clarke, P.R., and Zhang, C.M. (2008). Spatial and temporal coordination of mitosis by Ran GTPase. Nat Rev Mol Cell Biol *9*, 464-477.

Cokol, M., Nair, R., and Rost, B. (2000). Finding nuclear localization signals. EMBO Rep *1*, 411-415.

Conti, E., Muller, C.W., and Stewart, M. (2006). Karyopherin flexibility in nucleocytoplasmic transport. Curr Opin Struct Biol *16*, 237-244.

Cronshaw, J.A., Krutchinsky, A.N., Zhang, W.Z., Chait, B.T., and Matunis, M.J. (2002). Proteomic analysis of the mammalian nuclear pore complex. J Cell Biol *158*, 915-927.

D'Angelo, M.A., Raices, M., Panowski, S.H., and Hetzer, M.W. (2009). Age-Dependent Deterioration of Nuclear Pore Complexes Causes a Loss of Nuclear Integrity in Postmitotic Cells. Cell *136*, 284-295.

Dange, T., Grünwald, D., Grünwald, A., Peters, R., and Kubitscheck, U. (2008). Autonomy and robustness of translocation through the nuclear pore complex: A single-molecule study. J Cell Biol *183*, 77-86.

Davis, L.K., Saric, A., Hoogenboom, B.W., and Zilman, A. (2021). Physical modeling of multivalent interactions in the nuclear pore complex. Biophys J *120*, 1565-1577.

Dean, K.A., von Ahsen, O., Gorlich, D., and Fried, H.M. (2001). Signal recognition particle protein 19 is imported into the nucleus by importin 8 (RanBP8) and transportin. J Cell Sci *114*, 3479-3485.

Depping, R., Steinhoff, A., Schindler, S.G., Friedrich, B., Fagerlund, R., Metzen, E., Hartmann, E., and Kohler, M. (2008). Nuclear translocation of hypoxia-inducible factors (HIFs): Involvement of the classical importin alpha/beta pathway. Biochim Biophys Acta *1783*, 394-404.

Dickmanns, A., Kehlenbach, R.H., and Fahrenkrog, B. (2015). Nuclear Pore Complexes and Nucleocytoplasmic Transport: From Structure to Function to Disease. In International Review of Cell and Molecular Biology, Vol 320, K.W. Jeon, ed., pp. 171-233.

Dong, X., Biswas, A., Suel, K.E., Jackson, L.K., Martinez, R., Gu, H., and Chook, Y.M. (2009). Structural basis for leucine-rich nuclear export signal recognition by CRM1. Nature *458*, 1136-1141.

Eftekharzadeh, B., Daigle, J.G., Kapinos, L.E., Coyne, A., Schiantarelli, J., Carlomagno, Y., Cook, C., Miller, S.J., Dujardin, S., Amaral, A.S.*, et al.* (2018). Tau Protein Disrupts Nucleocytoplasmic Transport in Alzheimer's Disease. Neuron *99*, 925-940 e927.

Eibauer, M., Pellanda, M., Turgay, Y., Dubrovsky, A., Wild, A., and Medalia, O. (2015). Structure and gating of the nuclear pore complex. Nat Comm *6*.

Eisele, N.B., Andersson, F.I., Frey, S., and Richter, R.P. (2012). Viscoelasticity of thin biomolecular films: a case study on nucleoporin phenylalanine-glycine repeats grafted to a histidine-tag capturing QCM-D sensor. Biomacromolecules *13*, 2322-2332.

Eisele, N.B., Frey, S., Piehler, J., Görlich, D., and Richter, R.P. (2010). Ultrathin nucleoporin phenylalanine-glycine repeat films and their interaction with nuclear transport receptors. EMBO Rep *11*, 366-372.

Floch, A.G., Palancade, B., and Doye, V. (2014). Chapter 1 - Fifty Years of Nuclear Pores and Nucleocytoplasmic Transport Studies: Multiple Tools Revealing Complex Rules. In Methods in Cell Biology, V. Doye, ed. (Academic Press), pp. 1-40.

Fornerod, M., Ohno, M., Yoshida, M., and Mattaj, I.W. (1997). CRM1 is an export receptor for leucine-rich nuclear export signals. Cell *90*, 1051-1060.

Frey, S., and Gorlich, D. (2009). FG/FxFG as well as GLFG repeats form a selective permeability barrier with self-healing properties. EMBO J *28*, 2554-2567.

Frey, S., and Görlich, D. (2007). A saturated FG-repeat hydrogel can reproduce the permeability properties of nuclear pore complexes. Cell *130*, 512-523.

Frey, S., Rees, R., Schunemann, J., Ng, S.C., Funfgeld, K., Huyton, T., and Görlich, D. (2018). Surface properties determining passage rates of proteins through nuclear pores. Cell *174*, 202-217 e209.

Friedrich, B., Quensel, C., Sommer, T., Hartmann, E., and Kohler, M. (2006). Nuclear localization signal and protein context both mediate importin at specificity of nuclear import substrates. Mol Cell Biol *26*, 8697-8709.

Frieman, M., Yount, B., Heise, M., Kopecky-Bromberg, S.A., Palese, P., and Baric, R.S. (2007). Severe acute respiratory syndrome coronavirus ORF6 antagonizes STAT1 function by sequestering nuclear import factors on the rough endoplasmic Reticulum/Golgi membrane. J Virol *81*, 9812-9824.

Fukuhara, N., Fernandez, E., Ebert, J., Conti, E., and Svergun, D. (2004). Conformational variability of nucleo-cytoplasmic transport factors. J Biol Chem *279*, 2176-2181.

Fulcher, A.J., and Jans, D.A. (2011). Regulation of nucleocytoplasmic trafficking of viral proteins: An integral role in pathogenesis? Biochim Biophys Acta *1813*, 2176-2190.

Gaudet, P., Livstone, M.S., Lewis, S.E., and Thomas, P.D. (2011). Phylogenetic-based propagation of functional annotations within the Gene Ontology consortium. Brief Bioinform *12*, 449-462.

Goldfarb, D.S., Corbett, A.H., Mason, D.A., Harreman, M.T., and Adam, S.A. (2004). Importin alpha: a multipurpose nuclear-transport receptor. Trends Cell Biol *14*, 505-514.

Görlich, D., Dabrowski, M., Bischoff, F.R., Kutay, U., Bork, P., Hartmann, E., Prehn, S., and Izaurralde, E. (1997). A novel class of RanGTP binding proteins. J Cell Biol *138*, 65-80.

Görlich, D., and Kutay, U. (1999). Transport between the cell nucleus and the cytoplasm. Annu Rev Cell Dev Biol *15*, 607-660.

Görlich, D., Pante, N., Kutay, U., Aebi, U., and Bischoff, F.R. (1996). Identification of different roles for RanGDP and RanGTP in nuclear protein import. EMBO J *15*, 5584-5594.

Görlich, D., Seewald, M.J., and Ribbeck, K. (2003). Characterization of Ran-driven cargo transport and the RanGTPase system by kinetic measurements and computer simulation. EMBO J *22*, 1088-1100.

Görlich, D., Vogel, F., Mills, A.D., Hartmann, E., and Laskey, R.A. (1995). Distinct functions for the 2 importin subunits in nuclear-protein import. Nature *377*, 246-248.

Grima, J.C., Daigle, J.G., Arbez, N., Cunningham, K.C., Zhang, K., Ochaba, J., Geater, C., Morozko, E., Stocksdale, J., Glatzer, J.C.*, et al.* (2017). Mutant Huntingtin Disrupts the Nuclear Pore Complex. Neuron *94*, 93-+.

Grossman, E., Medalia, O., and Zwerger, M. (2012). Functional architecture of the nuclear pore complex. Annu Rev Biophys *41*, 557-584.

Grünwald, D., and Singer, R.H. (2010). In vivo imaging of labelled endogenous b-actin mRNA during nucleocytoplasmic transport. Nature *467*, 604-609.

Grünwald, D., Singer, R.H., and Rout, M. (2011). Nuclear export dynamics of RNA-protein complexes. Nature *475*, 333-341.

Gustin, K.E., and Sarnow, P. (2002). Inhibition of nuclear import and alteration of nuclear pore complex composition by rhinovirus. J Virol *76*, 8787-8796.

Guttinger, S., Muhlhausser, P., Koller-Eichhorn, R., Brennecke, J., and Kutay, U. (2004). Transportin2 functions as importin and mediates nuclear import of HuR. Proceedings of the National Academy of Sciences of the United States of America *101*, 2918-2923.

Gwizdek, C., Ossareh-Nazari, B., Brownawell, A.M., Evers, S., Macara, I.G., and Dargemont, C. (2004). Minihelix-containing RNAs mediate exportin-5-dependent nuclear export of the double-stranded RNA-binding protein ILF3. J Biol Chem *279*, 884-891.

Haasen, D., Kohler, C., Neuhaus, G., and Merkle, T. (1999). Nuclear export of proteins in plants: AtXPO1 is the export receptor for leucine-rich nuclear export signals in Arabidopsis thaliana. Plant J *20*, 695-705.

Hayes, L.R., Duan, L., Bowen, K., Kalab, P., and Rothstein, J.D. (2020). C9orf72 arginine-rich dipeptide repeat proteins disrupt karyopherin-mediated nuclear import. eLife *9*.

Hoogenboom, B.W., Hough, L.E., Lemke, E.A., Lim, R.Y.H., Onck, P.R., and Zilman, A. (2021). Physics of the nuclear pore complex: Theory, modeling and experiment. Physics Reports *921*, 1-53.

Hu, X.P., Kan, H.W., Boye, A., Jiang, Y.F., Wu, C., and Yang, Y. (2018). Mitogen-activated protein kinase inhibitors reduce the nuclear accumulation of phosphorylated Smads by inhibiting Imp 7 or Imp 8 in HepG2 cells. Oncology Letters *15*, 4867-4872.

Huang, K., and Szleifer, I. (2020). Modeling the nucleoporins that form the hairy pores. Biochem Soc Trans *BST20190941*.

Hülsmann, B.B., Labokha, A.A., and Görlich, D. (2012). The permeability of reconstituted nuclear pores provides direct evidence for the selective phase model. Cell *150*, 738-751.

Isgro, T.A., and Schulten, K. (2005). Binding dynamics of isolated nucleoporin repeat regions to importin-beta. Structure *13*, 1869-1879.

Izaurralde, E., Kutay, U., von Kobbe, C., Mattaj, I.W., and Görlich, D. (1997). The asymmetric distribution of the constituents of the Ran system is essential for transport into and out of the nucleus. EMBO J *16*, 6535-6547.

Jäkel, S., and Görlich, D. (1998). Importin beta, transportin, RanBP5 and RanBP7 mediate nuclear import of ribosomal proteins in mammalian cells. EMBO J *17*, 4491-4502.

Jans, D.A., Martin, A.J., and Wagstaff, K.M. (2019). Inhibitors of nuclear transport. Curr Opin Cell Biol *58*, 50-60.

Kalab, P., Weis, K., and Heald, R. (2002). Visualization of a Ran-GTP gradient in interphase and mitotic Xenopus egg extracts. Science *295*, 2452-2456.

Kalderon, D., Richardson, W.D., Markham, A.F., and Smith, A.E. (1984). Sequence requirements for nuclear location of simian virus-40 large t-antigen Nature *311*, 33-38.

Kalita, J., Kapinos, L.E., and Lim, R.Y.H. (2021). On the asymmetric partitioning of nucleocytoplasmic transport – recent insights and open questions. J Cell Sci *134*, jcs240382.

Kapinos, L.E., Huang, B., Rencurel, C., and Lim, R.Y.H. (2017). Karyopherins regulate nuclear pore complex barrier and transport function. J Cell Biol *216*, 3609-3624.

Kapinos, L.E., Schoch, R.L., Wagner, R.S., Schleicher, K.D., and Lim, R.Y. (2014). Karyopherin-centric control of nuclear pores based on molecular occupancy and kinetic analysis of multivalent binding with FG nucleoporins. Biophys J *106*, 1751-1762.

Kappel, C., Zachariae, U., Dölker, N., and Grubmüller, H. (2010). An Unusual Hydrophobic Core Confers Extreme Flexibility to HEAT Repeat Proteins. Biophysical Journal *99*, 1596-1603.

Kim, H.J., and Taylor, J.P. (2017). Lost in Transportation: Nucleocytoplasmic Transport Defects in ALS and Other Neurodegenerative Diseases. Neuron *96*, 285-297.

Kim, S.J., Fernandez-Martinez, J., Nudelman, I., Shi, Y., Zhang, W.Z., Raveh, B., Herricks, T., Slaughter, B.D., Hogan, J.A., Upla, P.*, et al.* (2018). Integrative structure and functional anatomy of a nuclear pore complex. Nature *555*, 475-+.

Kim, S.Y., Ryu, S.J., Ahn, H.J., Choi, H.R., Kang, H.T., and Park, S.C. (2010). Senescence-related functional nuclear barrier by down-regulation of nucleo-cytoplasmic trafficking gene expression. Biochem Biophys Res Commun *391*, 28-32.

Kimura, M., and Imamoto, N. (2014). Biological significance of the importin-beta family-dependent nucleocytoplasmic transport pathways. Traffic *15*, 727-748.

Klebe, C., Prinz, H., Wittinghofer, A., and Goody, R.S. (1995). The kinetic mechanism of Ran--nucleotide exchange catalyzed by RCC1. Biochemistry *34*, 12543-12552.

Kodiha, M., Chu, A., Matusiewicz, N., and Stochaj, U. (2004). Multiple mechanisms promote the inhibition of classical nuclear import upon exposure to severe oxidative stress. Cell Death Differ *11*, 862-874.

Kosugi, S., Hasebe, M., Matsumura, N., Takashima, H., Miyamoto-Sato, E., Tomita, M., and Yanagawa, H. (2009). Six Classes of Nuclear Localization Signals Specific to Different Binding Grooves of Importin alpha. Journal of Biological Chemistry *284*, 478-485.

Kosugi, S., Yanagawa, H., Terauchi, R., and Tabata, S. (2014). NESmapper: Accurate Prediction of Leucine-Rich Nuclear Export Signals Using Activity-Based Profiles. PLoS Comp Biol *10*.

Koyama, M., and Matsuura, Y. (2010). An allosteric mechanism to displace nuclear export cargo from CRM1 and RanGTP by RanBP1. EMBO J *29*, 2002-2013.

Kubitscheck, U., Grunwald, D., Hoekstra, A., Rohleder, D., Kues, T., Siebrasse, J.P., and Peters, R. (2005). Nuclear transport of single molecules: dwell times at the nuclear pore complex. J Cell Biol *168*, 233-243.

Kuersten, S., Arts, G.J., Walther, T.C., Englmeier, L., and Mattaj, I.W. (2002). Steady-state nuclear localization of exportin-t involves RanGTP binding and two distinct nuclear pore complex interaction domains. Mol Cell Biol *22*, 5708-5720.

Kutay, U., Bischoff, F.R., Kostka, S., Kraft, R., and Görlich, D. (1997). Export of importin alpha from the nucleus is mediated by a specific nuclear transport factor. Cell *90*, 1061-1071.

Kutay, U., Lipowsky, G., Izaurralde, E., Bischoff, F.R., Schwarzmaier, P., Hartmann, E., and Gorlich, D. (1998). Identification of a tRNA-specific nuclear export receptor. Mol Cell *1*, 359-369.

Lai, M.C., Kuo, H.W., Chang, W.C., and Tarn, W.Y. (2003). A novel splicing regulator shares a nuclear import pathway with SR proteins. EMBO J *22*, 1359-1369.

Lai, M.C., Lin, R.I., and Tarn, W.Y. (2001). Transportin-SR2 mediates nuclear import of phosphorylated SR proteins. Proc Natl Acad Sci U S A *98*, 10154-10159.

Lange, A., Mills, R.E., Lange, C.J., Stewart, M., Devine, S.E., and Corbett, A.H. (2007). Classical nuclear localization signals: definition, function, and interaction with importin alpha. J Biol Chem *282*, 5101-5105.

Lee, B.J., Cansizoglu, A.E., Suel, K.E., Louis, T.H., Zhang, Z.C., and Chook, Y.M. (2006). Rules for nuclear localization sequence recognition by karyopherin beta 2. Cell *126*, 543-558.

Lee, S.J., Sekimoto, T., Yamashita, E., Nagoshi, E., Nakagawa, A., Imamoto, N., Yoshimura, M., Sakai, H., Chong, K.T., Tsukihara, T.*, et al.* (2003). The structure of importin-beta bound to SREBP-2: Nuclear import of a transcription factor. Science *302*, 1571-1575.

Lemke, E.A. (2016). The Multiple Faces of Disordered Nucleoporins. J Mol Biol *428*, 2011-2024.

Lim, R.Y., and Fahrenkrog, B. (2006). The nuclear pore complex up close. Curr Opin Cell Biol *18*, 342-347.

Lim, R.Y., Fahrenkrog, B., Koser, J., Schwarz-Herion, K., Deng, J., and Aebi, U. (2007). Nanomechanical basis of selective gating by the nuclear pore complex. Science *318*, 640-643.

Lim, R.Y.H., Aebi, U., and Stoffler, D. (2006). From the trap to the basket: getting to the bottom of the nuclear pore complex. Chromosoma *115*, 15-26.

Lim, R.Y.H., Huang, B., and Kapinos, L.E. (2015). How to operate a nuclear pore complex by Kap-centric control. Nucleus *6*, 366-372.

Lim, R.Y.H., Huang, N.P., Koser, J., Deng, J., Lau, K.H.A., Schwarz-Herion, K., Fahrenkrog, B., and Aebi, U. (2006). Flexible phenylalanine-glycine nucleoporins as entropic barriers to nucleocytoplasmic transport. Proceedings of the National Academy of Sciences USA *103*, 9512-9517.

Lin, D.H., Stuwe, T., Schilbach, S., Rundlet, E.J., Perriches, T., Mobbs, G., Fan, Y., Thierbach, K., Huber, F.M., Collins, L.N.*, et al.* (2016). Architecture of the symmetric core of the nuclear pore. Science *352*, aaf1015.

Lipowsky, G., Bischoff, F.R., Schwarzmaier, P., Kraft, R., Kostka, S., Hartmann, E., Kutay, U., and Görlich, D. (2000). Exportin 4: a mediator of a novel nuclear export pathway in higher eukaryotes. EMBO J *19*, 4362-4371.

Lott, K., and Cingolani, G. (2011). The importin beta binding domain as a master regulator of nucleocytoplasmic transport. Biochim Biophys Acta *1813*, 1578-1592.

Lounsbury, K.M., and Macara, I.G. (1997). Ran-binding protein 1 (RanBP1) forms a ternary complex with Ran and karyopherin beta and reduces Ran GTPase-activating protein (RanGAP) inhibition by karyopherin beta. Journal of Biological Chemisry *272*, 551-555.

Lowe, A.R., Tang, J.H., Yassif, J., Graf, M., Huang, W.Y., Groves, J.T., Weis, K., and Liphardt, J.T. (2015). Importin-beta modulates the permeability of the nuclear pore complex in a Ran-dependent manner. Elife *4*.

Lund, E., Guttinger, S., Calado, A., Dahlberg, J.E., and Kutay, U. (2004). Nuclear export of microRNA precursors. Science *303*, 95-98.

Ma, J., Goryaynov, A., Sarma, A. and Yang, W. (2012). Self-regulated viscous channel in the nuclear pore complex. PNAS *109*, 7326–7331.

Macara, I.G. (2001). Transport into and out of the nucleus. Microbiol Mol Biol Rev *65*, 570.

Maertens, G.N., Cook, N.J., Wang, W., Hare, S., Gupta, S.S., Oztop, I., Lee, K., Pye, V.E., Cosnefroy, O., Snijders, A.P.*, et al.* (2014). Structural basis for nuclear import of splicing factors by human Transportin 3. Proc Natl Acad Sci U S A *111*, 2728-2733.

Mertens, J., Paquola, A.C.M., Ku, M.C., Hatch, E., Bohnke, L., Ladjevardi, S., McGrath, S., Campbell, B., Lee, H., Herdy, J.R.*, et al.* (2015). Directly Reprogrammed Human Neurons Retain Aging-Associated Transcriptomic Signatures and Reveal Age-Related Nucleocytoplasmic Defects. Cell Stem Cell *17*, 705-718.

Milles, S., Bui, K.H., Koehler, C., Eltsov, M., Beck, M., and Lemke, E.A. (2013). Facilitated aggregation of FG nucleoporins under molecular crowding conditions. EMBO Rep *14*, 178-183.

Milner, S.T. (1991). Polymer brushes. Science *251*, 905-914.

Mingot, J.M., Kostka, S., Kraft, R., Hartmann, E., and Görlich, D. (2001). Importin 13: a novel mediator of nuclear import and export. EMBO J *20*, 3685-3694.

Miorin, L., Kehrer, T., Sanchez-Aparicio, M.T., Zhang, K., Cohen, P., Patel, R.S., Cupic, A., Makio, T., Mei, M.H., Moreno, E.*, et al.* (2020). SARS-CoV-2 Orf6 hijacks Nup98 to block STAT nuclear import and antagonize interferon signaling. Proceedings of the National Academy of Sciences of the United States of America *117*, 28344-28354.

Mitrousis, G., Olia, A.S., Walker-Kopp, N., and Cingolani, G. (2008). Molecular basis for the recognition of snurportin 1 by importin beta. J Biol Chem *283*, 7877-7884.

Monecke, T., Haselbach, D., Voss, B., Russek, A., Neumann, P., Thomson, E., Hurt, E., Zachariae, U., Stark, H., Grubmuller, H.*, et al.* (2013). Structural basis for cooperativity of CRM1 export complex formation. Proc Natl Acad Sci USA *110*, 960-965.

Moore, M.S., and Blobel, G. (1993). The GTP-binding protein Ran/TC4 is required for protein import into the nucleus. Nature *365*, 661-663.

Neuwald, A.F., and Hirano, T. (2000). HEAT repeats associated with condensins, cohesins, and other complexes involved in chromosome-related functions. Genome Res *10*, 1445-1452.

O'Reilly, A.J., Dacks, J.B., and Field, M.C. (2011). Evolution of the karyopherin-beta family of nucleocytoplasmic transport factors; ancient origins and continued specialization. PLoS One *6*, e19308.

Okada, C., Yamashita, E., Lee, S.J., Shibata, S., Katahira, J., Nakagawa, A., Yoneda, Y., and Tsukihara, T. (2009). A high-resolution structure of the pre-microRNA nuclear export machinery. Science *326*, 1275-1279.

Ossareh-Nazari, B., Bachelerie, F., and Dargemont, C. (1997). Evidence for a role of CRM1 in signal-mediated nuclear protein export. Science *278*, 141-144.

Padavannil, A., Sarkar, P., Kim, S.J., Cagatay, T., Jiou, J., Brautigam, C.A., Tomchick, D.R., Sali, A., D'Arcy, S., and Chook, Y.M. (2019). Importin-9 wraps around the H2A-H2B core to act as nuclear importer and histone chperone. eLife *8*.

Paine, P.L., Moore, L.C., and Horowitz, S.B. (1975). Nuclear envelope permeability. Nature *254*, 109-114.

Paradise, A., Levin, M.K., Korza, G., and Carson, J.H. (2007). Significant Proportions of Nuclear Transport Proteins with Reduced Intracellular Mobilities Resolved by Fluorescence Correlation Spectroscopy. Journal of Molecular Biology *365*, 50-65.

Parikh, K., Cang, S., Sekhri, A., and Liu, D. (2014). Selective inhibitors of nuclear export (SINE)--a novel class of anti-cancer agents. Journal of hematology & oncology *7*, 78.

Pawlowski, R., Rajakyla, E.K., Vartiainen, M.K., and Treisman, R. (2010). An actin-regulated importin alpha/beta-dependent extended bipartite NLS directs nuclear import of MRTF-A. EMBO J *29*, 3448-3458.

Peters, R. (2005). Translocation through the nuclear pore complex: selectivity and speed by reduction-of-dimensionality. Traffic *6*, 421-427.

Peters, R. (2009a). Functionalization of a nanopore: the nuclear pore complex paradigm. Biochim Biophys Acta *1793*, 1533-1539.

Peters, R. (2009b). Translocation through the nuclear pore: Kaps pave the way. Bioessays *31*, 466-477.

Plafker, S.M., and Macara, I.G. (2000). Importin-11, a nuclear import receptor for the ubiquitin-conjugating enzyme, UbcM2. EMBO J *19*, 5502-5513.

Ploski, J.E., Shamsher, M.K., and Radu, A. (2004). Paired-type homeodomain transcription factors are imported into the nucleus by karyopherin 13. Mol Cell Biol *24*, 4824-4834.

Popken, P., Ghavami, A., Onck, P.R., Poolman, B., and Veenhoff, L.M. (2015). Size-dependent leak of soluble and membrane proteins through the yeast nuclear pore complex. Mol Biol Cell *26*, 1386-1394.

Port, S.A., Monecke, T., Dickmanns, A., Spillner, C., Hofele, R., Urlaub, H., Ficner, R., and Kehlenbach, R.H. (2015). Structural and Functional Characterization of CRM1-Nup214 Interactions Reveals Multiple FG-Binding Sites Involved in Nuclear Export. Cell Rep *13*, 690-702.

Pumroy, R.A., and Cingolani, G. (2015). Diversification of importin-alpha isoforms in cellular trafficking and disease states. Biochem J *466*, 13-28.

Quan, Y., Ji, Z.L., Wang, X., Tartakoff, A.M., and Tao, T. (2008). Evolutionary and transcriptional analysis of karyopherin beta superfamily proteins. Mol Cell Proteomics *7*, 1254-1269.

Reichelt, R., Holzenburg, A., Buhle, E.L., Jr, Jarnik, M., Engel, A., and Aebi, U. (1990). Correlation between structure and mass distribution of the nuclear pore complex and of distinct pore complex components. Journal of Cell Biology *110*, 883-894.

Rempel, I.L., Crane, M.M., Thaller, D.J., Mishra, A., Jansen, D.P., Janssens, G., Popken, P., Aksit, A., Kaeberlein, M., van der Giessen, E.*, et al.* (2019). Age-dependent deterioration of nuclear pore assembly in mitotic cells decreases transport dynamics. Elife *8*.

Rempel, I.L., Steen, A., and Veenhoff, L.M. (2020). Poor old pores-The challenge of making and maintaining nuclear pore complexes in aging. FEBS J *287*, 1058-1075.

Renault, L., Kuhlmann, J., Henkel, A., and Wittinghofer, A. (2001). Structural basis for guanine nucleotide exchange on Ran by the regulator of chromosome condensation (RCC1). Cell *105*, 245-255.

Ribbeck, K., and Görlich, D. (2001). Kinetic analysis of translocation through nuclear pore complexes. *20*, 1320-1330.

Ribbeck, K., Lipowsky, G., Kent, H.M., Stewart, M., and Görlich, D. (1998). NTF2 mediates nuclear import of Ran. EMBO J *17*, 6587-6598.

Robbins, J., Dilworth, S.M., Laskey, R.A., and Dingwall, C. (1991). 2 interdependent basic domains in nucleoplasmin nuclear targeting sequence - indentification of a class of bipartite nuclear targeting sequence. Cell *64*, 615-623.

Rout, M.P., Aitchison, J.D., Suprapto, A., Hjertaas, K., Zhao, Y., and Chait, B.T. (2000). The yeast nuclear pore complex: composition, architecture, and transport mechanism. J Cell Biol *148*, 635-651.

Rout, M.P., and Blobel, G. (1993). Isolation of the yeast nuclear pore complex. The Journal of cell biology *123*, 771-783.

Sabri, N., Roth, P., Xylourgidis, N., Sadeghifar, F., Adler, J., and Samakovlis, C. (2007). Distinct functions of the Drosophila Nup153 and Nup214 FG domains in nuclear protein transport. J Cell Biol *178*, 557-565.

Sakiyama, Y., Mazur, A., Kapinos, L.E., and Lim, R.Y.H. (2016). Spatiotemporal dynamics of the nuclear pore complex transport barrier resolved by high-speed atomic force microscopy. Nat Nanotechnol *11*, 719-723.

Schleicher, K.D., Dettmer, S.L., Kapinos, L.E., Pagliara, S., Keyser, U.F., Jeney, S., and Lim, R.Y.H. (2014). Selective transport control on molecular velcro made from intrinsically disordered proteins. Nature Nanotechnology *9*, 525-530.

Schmidt, H.B., and Görlich, D. (2015). Nup98 FG domains from diverse species spontaneously phase-separate into particles with nuclear pore-like permselectivity. eLife *4*.

Schoch, R.L., Kapinos, L.E., and Lim, R.Y. (2012). Nuclear transport receptor binding avidity triggers a self-healing collapse transition in FG-nucleoporin molecular brushes. Proceedings of the National Academy of Sciences of the United States of America *109*, 16911-16916.

Siomi, M.C., Eder, P.S., Kataoka, N., Wan, L.L., Liu, Q., and Dreyfuss, G. (1997). Transportin-mediated nuclear import of heterogeneous nuclear RNP proteins. J Cell Biol *138*, 1181-1192.

Smith, A.E., Slepchenko, B.M., Schaff, J.C., Loew, L.M., and Macara, I.G. (2002). Systems analysis of Ran transport. Science *295*, 488-491.

Spits, M., Janssen, L.J., Voortman, L.M., Kooij, R., Neefjes, A.C.M., Ovaa, H., and Neefjes, J. (2019). Homeostasis of soluble proteins and the proteasome post nuclear envelope reformation in mitosis. J Cell Sci *132*.

Stade, K., Ford, C.S., Guthrie, C., and Weis, K. (1997). Exportin 1 (Crm1p) is an essential nuclear export factor. Cell *90*, 1041-1050.

Stewart, M. (2007). Molecular mechanism of the nuclear protein import cycle. Nat Rev Mol Cell Biol *8*, 195-208.

Strambio-De-Castillia, C., Niepel, M., and Rout, M.P. (2010). The nuclear pore complex: bridging nuclear transport and gene regulation. Nat Rev Mol Cell Biol *11*, 490-501.

Strawn, L.A., Shen, T.X., Shulga, N., Goldfarb, D.S., and Wente, S.R. (2004). Minimal nuclear pore complexes define FG repeat domains essential for transport. Nat Cell Biol *6*, 197-206.

Terry, L.J., Shows, E.B., and Wente, S.R. (2007). Crossing the nuclear envelope: Hierarchical regulation of nucleocytoplasmic transport. Science *318*, 1412-1416.

Timney, B.L., Raveh, B., Mironska, R., Trivedi, J.M., Kim, S.J., Russel, D., Wente, S.R., Sali, A., and Rout, M.P. (2016). Simple rules for passive diffusion through the nuclear pore complex. J Cell Biol *215*, 57-76.

Tu, L.C., Fu, G., Zilman, A., and Musser, S.M. (2013). Large cargo transport by nuclear pores: implications for the spatial organization of FG-nucleoporins. EMBO J *32*, 3220-3230.

Twyffels, L., Gueydan, C., and Kruys, V. (2014). Transportin-1 and Transportin-2: protein nuclear import and beyond. FEBS Lett *588*, 1857-1868.

Vetter, I.R., Nowak, C., Nishimoto, T., Kuhlmann, J., and Wittinghofer, A. (1999). Structure of a Ran-binding domain complexed with Ran bound to a GTP analogue: implications for nuclear transport. Nature *398*, 39-46.

von Appen, A., Kosinski, J., Sparks, L., Ori, A., DiGuilio, A.L., Vollmer, B., Mackmull, M.T., Banterle, N., Parca, L., Kastritis, P.*, et al.* (2015). In situ structural analysis of the human nuclear pore complex. Nature *526*, 140-+.

Wagner, R.S., Kapinos, L.E., Marshall, N.J., Stewart, M., and Lim, R.Y.H. (2015). Promiscuous binding of Karyopherinbeta1 modulates FG nucleoporin barrier function and expedites NTF2 transport kinetics. Biophys J *108*, 918-927.

Watters, K., and Palmenberg, A.C. (2011). Differential Processing of Nuclear Pore Complex Proteins by Rhinovirus 2A Proteases from Different Species and Serotypes. J Virol *85*, 10874-10883.

Wei, Y., Li, L.M., Wang, D., Zhang, C.Y., and Zen, K. (2014). Importin 8 Regulates the Transport of Mature MicroRNAs into the Cell Nucleus. J Biol Chem *289*, 10270-10275.

Weis, K. (2003). Regulating access to the genome: Nucleocytoplasmic transport throughout the cell cycle. Cell *112*, 441-451.

Wente, S.R., and Rout, M.P. (2010). The nuclear pore complex and nuclear transport. Cold Spring Harb Perspect Biol *2*, a000562.

Wühr, M., Güttler, T., Peshkin, L., McAlister, Graeme C., Sonnett, M., Ishihara, K., Groen, Aaron C., Presler, M., Erickson, Brian K., Mitchison, Timothy J.*, et al.* (2015). The Nuclear Proteome of a Vertebrate. Current Biology *25*, 2663-2671.

Xu, D.R., Farmer, A., Collett, G., Grishin, N.V., and Chook, Y.M. (2012). Sequence and structural analyses of nuclear export signals in the NESdb database. Mol Biol Cell *23*, 3677-3693.

Yamada, J., Phillips, J.L., Patel, S., Goldfien, G., Calestagne-Morelli, A., Huang, H., Reza, R., Acheson, J., Krishnan, V.V., Newsam, S.*, et al.* (2010). A bimodal distribution of two distinct categories of intrinsically disordered structures with separate functions in FG nucleoporins. Mol Cell Proteomics *9*, 2205-2224.

Yang, W., Gelles, J., and Musser, S.M. (2004). Imaging of single-molecule translocation through nuclear pore complexes. Proc Natl Acad Sci USA *101*, 12887-12892.

Yang, W., and Musser, S.M. (2006). Nuclear import time and transport efficiency depend on importin beta concentration. J Cell Biol *174*, 951-961.

Yarbrough, M.L., Mata, M.A., Sakthivel, R., and Fontoura, B.M. (2014). Viral subversion of nucleocytoplasmic trafficking. Traffic *15*, 127-140.

Yi, R., Doehle, B.P., Qin, Y., Macara, I.G., and Cullen, B.R. (2005). Overexpression of exportin 5 enhances RNA interference mediated by short hairpin RNAs and microRNAs. RNA *11*, 220-226.

Yoon, J., Kim, S.J., An, S., Cho, S., Leitner, A., Jung, T., Aebersold, R., Hebert, H., Cho, U.S., and Song, J.J. (2018). Integrative Structural Investigation on the Architecture of Human Importin4_Histone H3/1-14_Asf1a Complex and Its Histone H3 Tail Binding. J Mol Biol *430*, 822-841.

Yoshimura, S.H., Kumeta, M., and Takeyasu, K. (2014). Structural mechanism of nuclear transport mediated by importin beta and flexible amphiphilic proteins. Structure (London, England : 1993) *22*, 1699-1710.

Zachariae, U., and Grubmuller, H. (2008). Importin-beta: structural and dynamic determinants of a molecular spring. Structure (London, England : 1993) *16*, 906-915.

Zahn, R., Osmanovic, D., Ehret, S., Callis, C.A., Frey, S., Stewart, M., You, C.J., Goerlich, D., Hoogenboom, B.W., and Richter, R.P. (2016). A physical model describing the interaction of nuclear transport receptors with FG nucleoporin domain assemblies. eLife *5*.

Zhang, W., Lu, Y., Li, X., Zhang, J., Lin, W., Zhang, W., Zheng, L., and Li, X. (2019). IPO5 promotes the proliferation and tumourigenicity of colorectal cancer cells by mediating RASAL2 nuclear transportation. J Exp Clin Cancer Res *38*, 296.

Zilman, A. (2018). Aggregation, Phase Separation and Spatial Morphologies of the Assemblies of FG Nucleoporins. Journal of Molecular Biology *430*, 4730-4740.

Chapter 2

In vivo localization and enrichment of Karyopherins in the NPC

Adapted from

On the asymmetric partitioning of nucleocytoplasmic transport – recent insights and open questions

Joanna Kalita, Larisa E. Kapinos and Roderick Y. H. Lim

Published in Journal of Cell Science, 134(7), jcs.240382 (2021)

&

Karyopherin enrichment and compensation fortifies the nuclear pore complex against nucleocytoplasmic leakage

Joanna Kalita, Larisa E. Kapinos, Tiantian Zheng, Chantal Rencurel, Anton Zilman and Roderick Y. H. Lim

Published in Journal of Cell Biology, 221(3), jcb.202108107 (2022)

2.1 Asymmetric partitioning of Kapβs

The asymmetric partitioning of Kapβs is one of the most striking and, perhaps least understood hallmarks of NCT. Kapβs freely translocate between cytoplasm and nucleus due to their direct interactions with FG Nups. Since Kapβs lack NLS or NES signals, intuitively their shuttling should lead to an equal distribution in both compartments. Yet, most importins tend to localize in the cytoplasm (except for importin-11 (Imp11, also known as IPO11)), whereas exportins reside in the nucleus, and transportins can be distributed in the nucleus or cytoplasm, depending on their primary function (Fig. 2.1A). Quantitative analysis by compartment-based mass spectrometry of *X. laevis* oocytes revealed that the nuclear-to-cytoplasmic ratio (N:C) of Kapβ1 is ~1:10, while the N:C ratio for both CAS and CRM1 is almost 2:1 (Fig. 2.1B) (Kirli et al., 2015). Presumably, the compartmentalization of Kapβs directly impacts their transport efficiency. For example, the prominent cytoplasmic presence of Kapβ1 ensures that all NLS- or IBB- cargos efficiently are targeted to the NPCs. The same logic applies to the assembly of export complexes in the nucleus, where a high concentration of exportins and RanGTP facilitates the formation of exportin-cargo-RanGTP triple assemblies. Sequestering transport-specific cargos is crucial, especially for small cargos (e.g., ribosomal proteins) whose size is below the NPC exclusion limit (<40 kDa) (Fig. 2.2). For example, Importin-5 (Imp5, also known as IPO5 or RANBP5) (Jäkel and Görlich, 1998; Swale et al., 2020) is responsible for the import of several ribosomal proteins, such as RPL23A (17.7 kDa), RPS7 (17.7 kDa), and RPL5 (34.4 kDa), and RNA binding proteins into the nucleus (see Table 1.1) (Chook and Süel, 2011). Theoretically, these proteins should be able to diffuse freely through the NPCs, but the high cytoplasmic concentration of Imp5 (also Importin-7 or Importin-9) (Jakel and Gorlich, 1998) (Table 1.1) may play a role in preventing their return into the cytoplasm (Fig. 2.2).

The mechanism(s) that regulates the partitioning of exportins in the nucleus remains elusive despite noted associations between exportins and cancer (Cagatay and Chook, 2018). For example, CRM1 is involved in the export of NES-cargos (Johnson et al., 2002) including mRNA complexes and ribosomal subunits (Chao et al., 2012; Jäkel and Görlich, 1998; Spits et al., 2019; Sutherland et al., 2015), as well as a tumor suppressor and regulatory proteins such as BRCA1 (Brodie and Henderson, 2012) and p53 (Kanai et al., 2007). In cancer, CRM1 overexpression enhances the nuclear export of such tumor suppressor proteins, resulting in

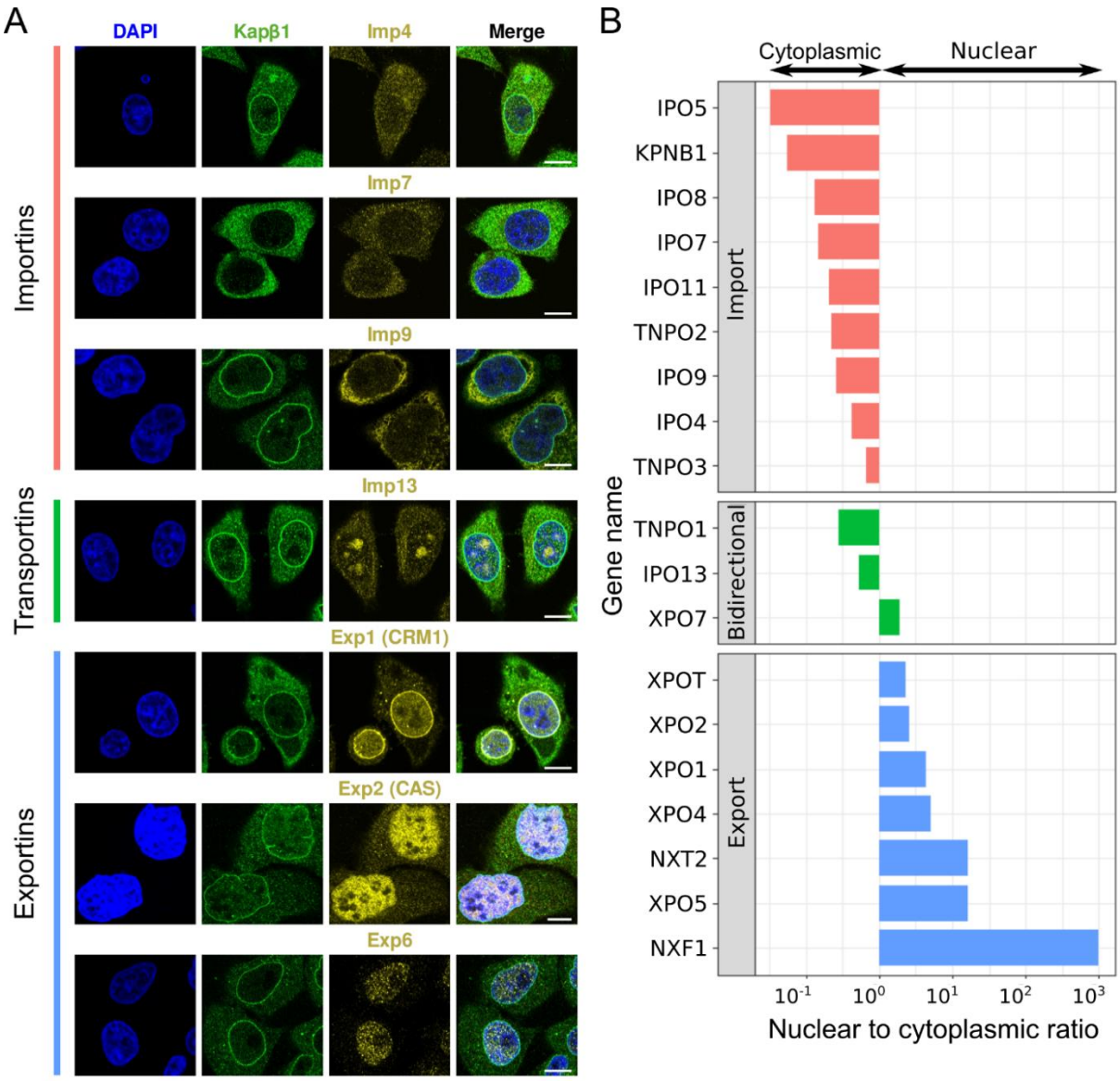

Figure 2.1 Asymmetric partitioning of Kapβs and their enrichment at NPCs in cells

(A) Immunofluorescence reveals that importins localize predominantly in the cytoplasm, while exportins are found in the nucleus. Nuclear rim stainings indicate that Kapβ1 and CRM1 are highly enriched at NPCs. Endogenous Kapβ1 was co-stained with Imp4, Imp7, Imp9, Imp13, Exp1 (CRM1), Exp2 (CAS), or Exp6 in HeLa cells using a standard protocol (Kapinos et al., 2017). The following antibodies were used: anti-Kapβ1 (abcam, Cat # ab2811), anti-Imp4 (abcam, Cat # ab 181046), anti-Imp7 (abcam, Cat # ab15840), anti-Imp9 (abcam, Cat # ab52605), anti-Imp13 (abcam, Cat # ab95993), anti-CRM1 (abcam, Cat # ab24189), anti-CAS (abcam, Cat # ab96755), anti-Exp6 (Bethyl, A301-205A). Scale bar is 5 µm. Courtesy of Dr. Larisa Kapinos. (B) Nuclear to cytoplasmic ratios of Kapβs obtained from quantitative mass spectrometric analysis of fractionated X. laevis oocytes correlate with the immunofluorescence shown in panel (A). The bar plot was created based on the mass spectrometry data from Kirli et. al., 2015 under the terms of a Creative Commons Attribution license (CC BY 4.0).

their mislocalization and functional inactivation in the cytoplasm (Azmi et al., 2021). This has led to the development of selective inhibitors of nuclear export (SINE) that prevent the binding of such NES-cargoes to CRM1 (Azizian and Li, 2020; Parikh et al., 2014; Sun et al., 2016). CAS, whose role is to export Kapα back to the cytoplasm to sustain nuclear import, is another exportin that is overexpressed during cancer progression and metastasis (Jiang, 2016). It is therefore pertinent to account for how exportins are asymmetrically partitioned in the nucleus and to address how impairing this behavior leads to downstream defects in NCT with relevance to disease. Thus far, only one study has linked the nuclear localization of exportin-T (Xpo-t) to the RanGTP gradient (Kuersten et al., 2002) whereby Xpo-t was mislocalized when its interactions with RanGTP were impaired.

2.2 Kapβ enrichment at NPCs supports the Kap-centric control model

Besides their partitioning characteristics, Kapβ1 and CRM1 exhibit a marked enrichment at the NPCs, which is visible as a distinct nuclear rim staining (Fig. 2.1 and Fig 2.3) (Heaton et al., 2019; Kalita et al., 2021; Kapinos et al., 2017; Lim et al., 2015; Lowe et al., 2015). In other words, NPCs are predominantly crowded with Kapβs that could potentially modulate FG Nup behavior to impact NPC function (Zilman, 2018). This observation supports the Kap-centric model, which argues that the NPC permeability barrier comprises of Kapβs, FG-Nups, and water (Vovk et al., 2016; Zilman, 2018). In this form, Kapβ occupancy in the NPCs could modulate the biophysical behavior of FG Nups and impact on permeability barrier function (Kapinos et al., 2014; Vovk et al., 2016; Zahn et al., 2016). Recent experimental results show to support this model, although the extent of how Kapβs might impose control in the NPC remains incompletely understood. As a case in point, *in vitro* FG Nup studies report permeability barrier properties that facilitate Kapβ passage but exclude non-specific cargoes irrespective of their different material characteristics. Moreover, it was shown that Kapβ1 depletion *ex vivo* abrogates NPC barrier function against non-specific cargoes, whereas adding back Kapβ1 rescues it (Kapinos et al., 2017).

Additionally, recent results suggest that the enriched pool of Kapβ1 at NPCs preserves the steep Ran gradient by binding freely diffusing RanGTP (Fig. 2.2, 'Recapture') (Barbato et al., 2020). Indeed, a substantial leakage of Ran from the nucleus was reported when NPCs lacked Kapβ1 enrichment. This Kapβ1-driven retention mechanism is biochemically specific for RanGTP, as passive molecules of a comparable (e.g., GFP) could still traverse the NPC (Barbato

et al., 2020). Such a retention mechanism might further explain the steady-state accumulation of Ran at NPCs (Abu-Arish et al., 2009; Smith et al., 2002; Yang and Musser, 2006). More generally, it was suggested that Kapβ1 enrichment at the NPCs increases the efficiency of NCT by minimizing RanGTP losses from the nucleus. In this manner, also small NLS-cargoes may be prevented from returning to the cytoplasm by binding to Kapβs that are enriched within the

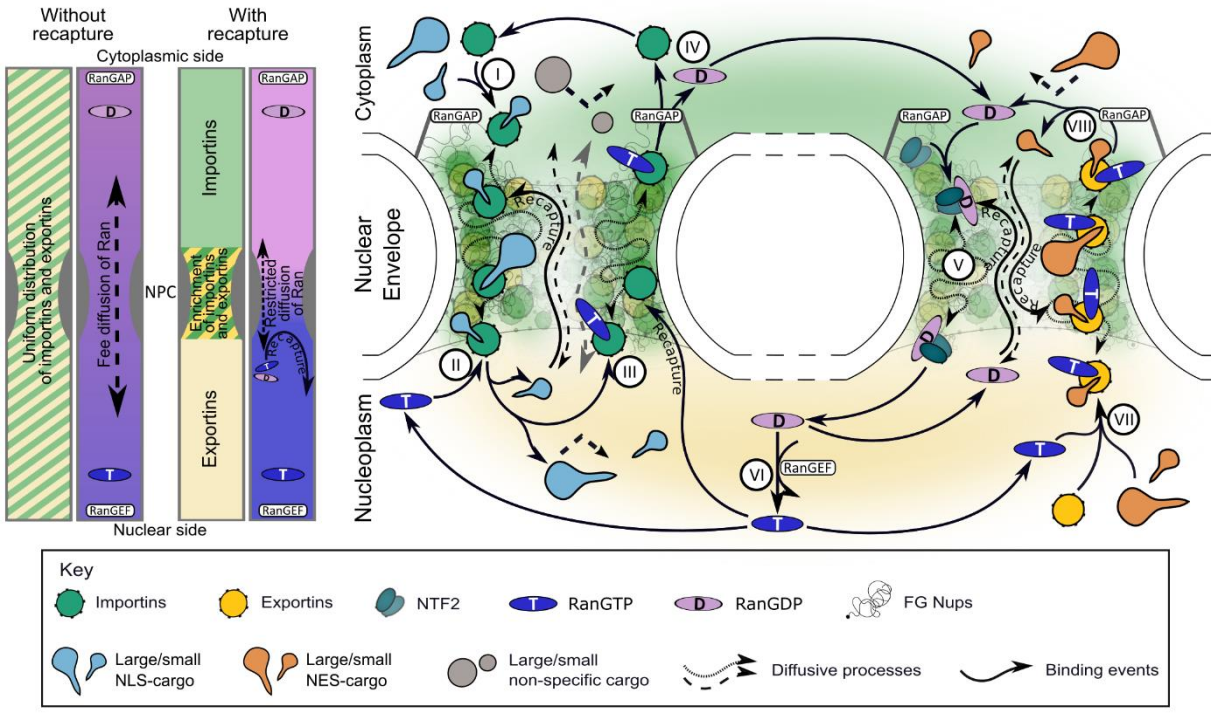

Figure 2.2 Recapture at NPCs facilitates nucleocytoplasmic partitioning

(A) Left - RanGAP1 and RanGEF activity in the absence of enriched Kapβs at NPCs results in a poor Ran gradient due to the leakage of RanGTP and RanGDP between compartments. Right - An enrichment of Kapβs at the NPC facilitates the recapture of RanGTP to minimize leakage and preserve the steep Ran gradient. (B) The mechanistic steps necessary for maintaining nucleocytoplasmic partitioning are as follows: I. Importins partition in the cytoplasm and shuttle NLS-cargoes through NPCs into the nucleus. II. NLS-cargo is released into the nucleus following RanGTP-importin binding at the NPC exit. III. RanGTP-importin complexes traverse NPCs to return to the cytoplasm. IV. RanGAP hydrolyses RanGTP into RanGDP, which frees the importin in the cytoplasm for another import cycle. V. RanGDP is returned to the nucleus through NPCs by NTF2. VI. RanGEF converts RanGDP back to RanGTP. VII. RanGTP enables the formation of NES-cargo-exportin-RanGTP complexes that circulate back through the NPC. VIII. Upon reaching the cytoplasm, RanGAP again hydrolyses RanGTP into RanGDP, which disassembles the NES-cargo-exportin-RanGTP complex. Additional remarks: 1. The partitioning of exportins in the nucleus results from an as yet unknown mechanism. 2. Both importins and exportins enrich at NPCs. 3. RanGDP, RanGTP, and other small cargoes are recaptured by Kapβs that are enriched inside the NPC to minimize non-specific leakage between compartments. 4. NCT translocation processes are diffusive. 5. NCT directionality is conferred by the RanGTP gradient. 6. Nucleocytoplasmic exchanges might occur in close spatial proximity to the NE so that Kapβs are rapidly re-circulated back through the NPC. 7. Large non-specific cargoes are repelled from the NPC.

NPC. One could speculate that a similar retention mechanism could be sustained by exportins for the prevention of leakage of small NES-cargoes (Fig. 2.2, 'Recapture'), however, no experimental evidence has been provided so far.

2.3 Subcellular localization of fluorescently-tagged Kapβs

Immunofluorescence (IF) staining (Fig. 2.1) is not applicable for *in vivo* experimentation. Moreover, it is limited by the ability of antibodies to permeate into cells and organelles. The final staining outcome also depends on the specificity and sensitivity of a given antibody, which can be a limiting factor, especially when working with samples of non-human origin. Thus, to overcome these limitations and confirm the subcellular localization of the Kapβs of interest, we created fluorescently tagged constructs of Kapβ1, CRM1, and Imp5 using the pcDNA3.1(-) vector suitable for mammalian expression. Indeed, the subcellular localization pattern of Kapβ1-EGFP, EGFP-CRM1, or Imp5-mCherry in transiently transfected MDCK cells matches IF results well (Fig. 2.1 and Fig. 2.3A). Both Kapβ1 and CRM1 exhibit a nuclear rim staining that coincides with the edges of the DAPI signal (Fig. 2.3B). This is also reflected in the NE to cytoplasm (NE:C) and NE to nucleus (NE:N) fluorescent ratios of Kapβ1 and CRM1, respectively, whose values reach above 1 (Fig. 2.3C, D). Imp5, on the other hand, has a NE:C ratio equal to 1, thereby indicating that it is predominantly cytoplasmic and does not substantially enrich NPCs (Fig. 2.3A-C). We note that the overexpression of Imp5 does not shift its steady-state distribution, which theoretically could lead to its partial accumulation in the NPCs.

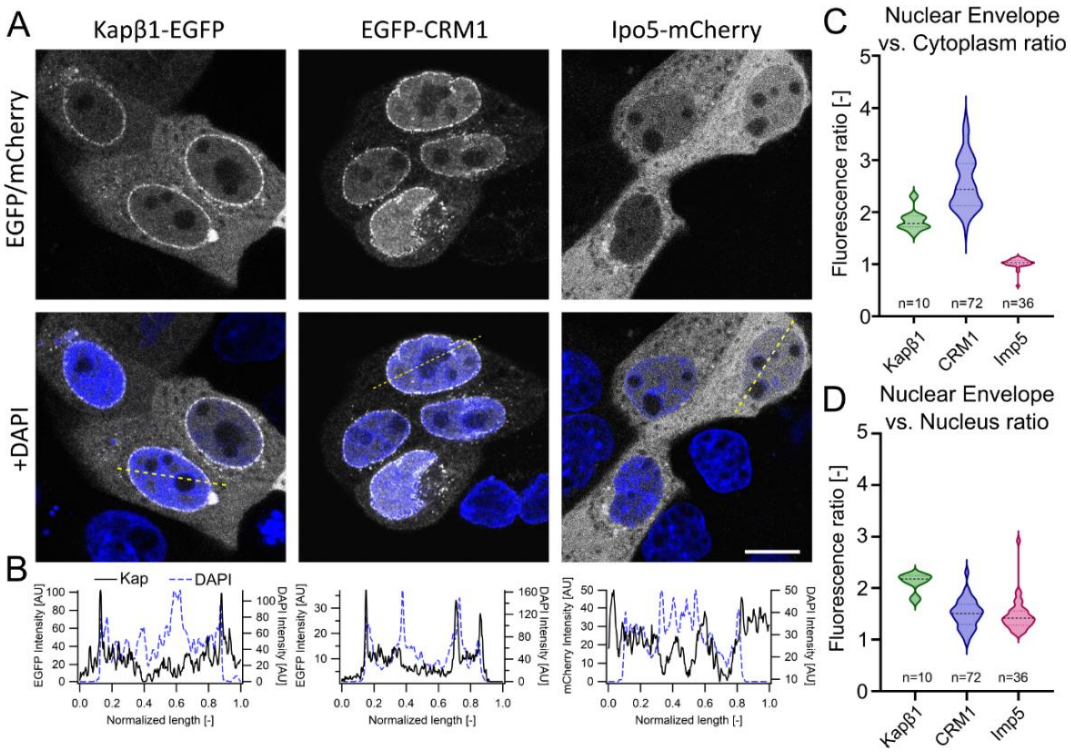

Figure 2.3 Kapβs enrichment in vivo

(A) Transient transfections of MDCK cells with Kapβ1-EGFP, EGFP-CRM1, and Imp5-mCherry constructs reveal the subcellular localization of Kapβs in vivo. Kapβ1 and CRM1 show visible nuclear rim staining indicating their enrichment at the NPCs whereas Imp5 does not. Scale bar, 10 µm. (B) Fluorescence profiles were obtained along the dashed lines shown in (A). Kapβ1-EGFP and EGFP-CRM1 show fluorescence spikes (black) that coincide with the edges of the nuclear DAPI staining (blue) whereas similar features are lacking in the Imp5-mCherry signal. Line plots were created using Fiji after smoothing the images with the median filter (2-pixel radius) to minimize signal noise. (C) NE to cytoplasm (NE:C) and (D) NE to nucleus (NE:N) fluorescence ratios of the constructs shown in (A). For importins and exportins, accumulation in the NPCs is indicated by NE:C>1 and NE:N>1, respectively.

2.4 Persistence of Kapβs at the NPCs

Next, we investigated the persistence of Kapβ1, CRM1, and Imp5 at the NPC. To do so, we permeabilized transiently transfected HeLa cells with digitonin followed by the application of Ran mix to deplete endogenously expressed Kapβs (i.e., fluorescent and native ones) from the NPCs (Fig. 2.4A) (Adam et al., 1990; Barbato et al., 2020; Kapinos et al., 2017; Pulupa et al., 2020). Subsequent quantification of the NE fluorescent signal reveals that only around 8% of Kapβ1-EGFP (Fig. 2.4B, E) and 3% of EGFP-CRM1 (Fig. 2.4C, F) remain at the NPCs after such treatment. In marked contrast, only a residual signal of Imp5-mCherry could be detected after the first incubation step (Fig. 2.4D).

Since the fluorescently tagged Kapβs serve as a proxy for the behavior of endogenous Kapβs, these experiments ultimately show to which extent Ran mix is able to remove Kapβs

from the NPCs and that Kapβ1 is even more persistent than CRM1. The long Kapβ1 residence time is consistent with *in vitro* measurements where at low concentrations, Kapβ1 departure from the FG Nup layers is characterized by small dissociation rates (Kapinos et al., 2014). It is also likely that a persistent fraction of Kapβ1-EGFP associates with a pool of karyopherinα2 (Kapα2; importinα1) that binds with Nup153 and Nup50 through non-FG repeat interactions (Makise et al., 2012; Ogawa et al., 2012).

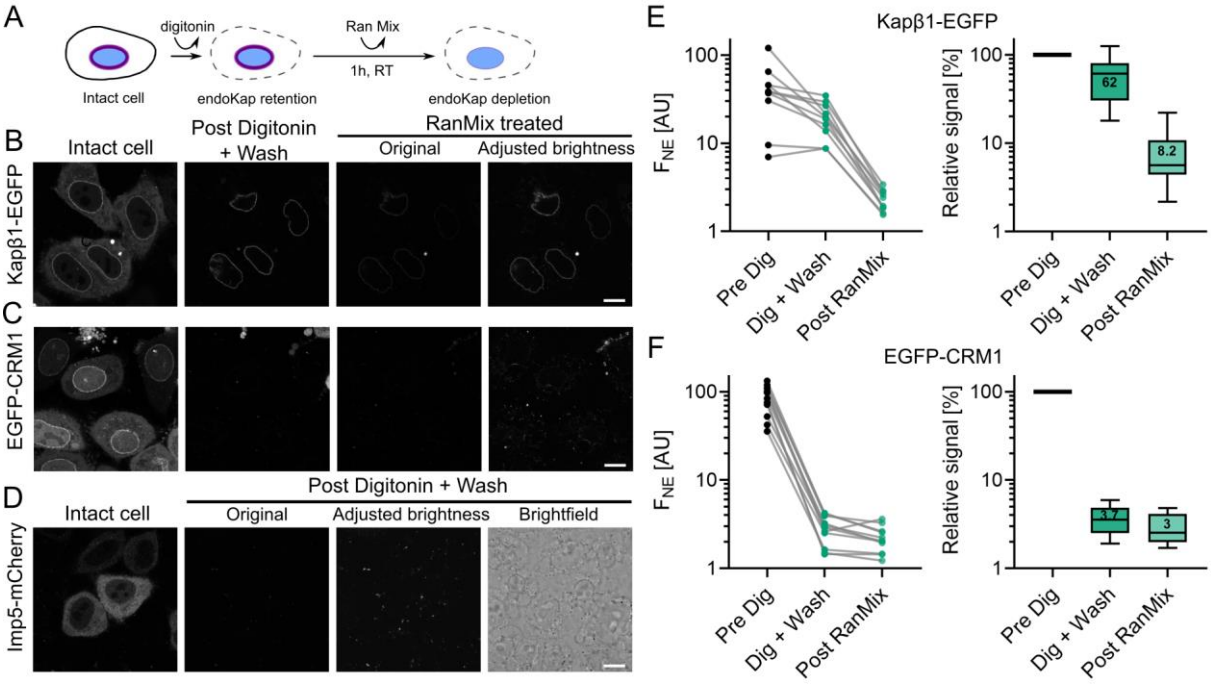

Figure 2.4 Retention of Kapβ1-EGFP, EGFP-CRM1, and Imp5-mCherry at NPCs following digitonin permeabilization and Ran mix treatments.

(A) Experimental sequence. (B) Images of intact and post-treatment HeLa cells transfected with Kapβ1-EGFP. Ran mix treated cells are shown with original and brightness-adjusted settings for improved visualization. (C) Pre- and post-digitonin treatment of HeLa cells transfected with EGFP-CRM1. Original as well as brightness-adjusted images of Ran mix treated cells are shown. (D) Any retention of Imp5-mCherry in digitonin-permeabilized HeLa cells lies below the detection limit as shown with brightness adjustment. The brightfield image confirms that cells were not removed from the field of view during the treatment. Further quantification of Imp5-mCherry has been omitted (E) Quantification of Kapβ1-EGFP fluorescence signal at the NE (F_{NE}). Each data point represents a single cell. Ran mix causes a ~90% reduction in the signal of Kapβ1-EGFP. Data points were normalized to the F_{NE} of each intact cell (F) EGFP-CRM1 fluorescence quantification at the NE. Ran mix reduces the EGFP-CRM1 signal by over 95%. Each series of images shown in (B), (C) and (D) was collected using the same imaging conditions. Error bars denote minimum and maximum measured values. Scale bar: 10 µm.

2.5 Cellular abundance of Kapβs in MDCK cells

Although not all Kapβ–FG-Nup interactions have been characterized, the known values of their apparent dissociation constant (K_D) typically fall in the sub-micromolar range (Kapinos et al., 2014; Schoch et al., 2012; Tan et al., 2018; Tetenbaum-Novatt et al., 2012). Hence, the amount of each Kapβ that populates the NPC should be proportional to its cellular concentration, which varies from the nanomolar to micromolar range (Kirli et al., 2015; Nguyen et al., 2019; Wang et al., 2015; Wühr et al., 2015). In MDCK cells, Kapβ1, Imp5, CRM1, Importin-7 (Imp7, IPO7), and Transportin-1 (TNPO1) are the five most abundant Kapβs (Fig. 2.5). Given that Kapβ1 and CRM1 colocalize at NPCs (Fig. 2.1 and Fig. 2.3) suggests that their presence might modulate the multivalent interactions between the FG-Nups and other Kapβs. Indeed, this so-called binding promiscuity is relevant to how intrinsically disordered proteins interact with multiple partners simultaneously (Uversky, 2013) as has been shown for the binding of Kapβ1 and NTF2 to the FG Nups (Wagner et al., 2015).

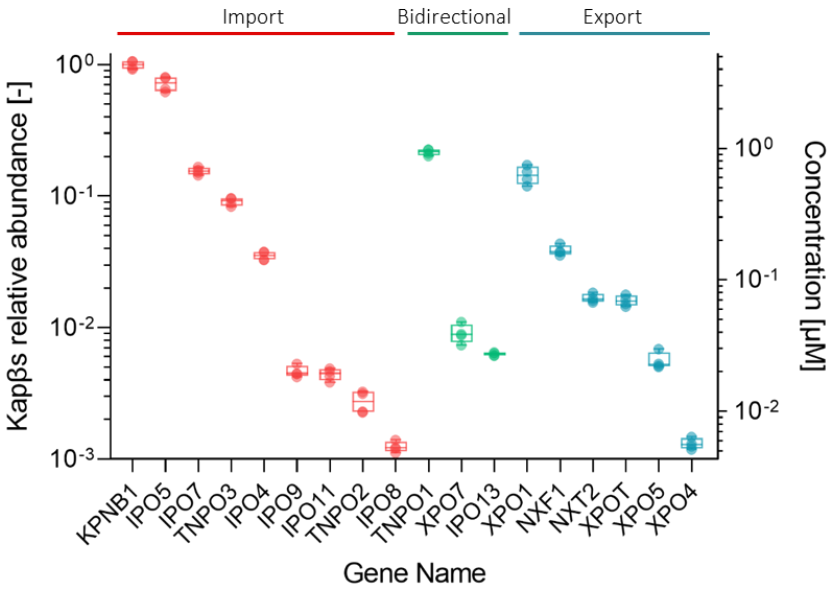

Figure 2.5 Absolute abundance of Kapβs in MDCK cells

Cellular concentration of Kapβs that govern import, export, or bidirectional transport was obtained via mass spectroscopy-based proteomics. (Abbreviations: KPNB1 – karyopherin beta-1, IPO5- importin-5, IPO7- importin-7, TNPO3- transportin-3, IPO4- importin-4, IPO9- importin-9, IPO11- importin-11, TNPO2- transportin-2, IPO8- importin-8, TNPO1- transportin-1, XPO7- exportin-7, IPO13- importin-13, XPO1- exportin-1, NXF1- nuclear RNA export factor 1, NXT2- NTF2-related export protein 2, XPOT- exportin-T, XPO5- exportin-5, XPO4- exportin-4).

2.6 Conclusions

The nature of NCT requires different Kapβs to traverse the NPCs in a continuous manner to transport their specific cargoes. Hence, *in vivo* NPCs are predominantly crowded with Kapβs, especially with Kapβ1 and CRM1 (Fig. 2.1 and Fig 2.3). This observation agrees with the ability of Kapβs to permeate and enrich within the FG Nups *in vitro* (Celetti et al., 2020; Frey and Görlich, 2007, 2009; Jovanovic-Talisman et al., 2009; Kapinos et al., 2014) and supports the Kap-centric model (Kapinos et al., 2017; Lim et al., 2015; Zahn et al., 2016). For example, Kapβ enrichment at the NPC may not only serve to facilitate signal-specific cargo transport but may also hinder the unsolicited entry of non-specific cargoes and prevent the leakage of Ran and other small specific cargoes between compartments (Barbato et al., 2020).

Still, it is not obvious why Imp5, being more abundant than CRM1 is less pronounced at the NPC (Fig. 2.3). Hence, it appears that the steady-state enrichment of Kapβs at the NPC is not purely concentration-driven. Subtler features such as FG Nup-binding characteristics, size of each Kapβs, the number of FG-repeat binding pockets, molecular flexibility, and shape (Christie et al., 2016; Conti et al., 2006) could also influence their binding. Finally, there exists a subset of persistent Kapβ1, and to a smaller extent CRM1, molecules, that remain at NPCs following Ran mix treatment. The mechanism that underlies competition of different Kapβs for FG Nup binding will be discussed in Chapter 3.

2.7 Materials and Methods

2.7.1 Cell culture

MDCK cells (a kind gift from I. N¨athke, University of Dundee, Dundee, UK) were cultured in Minimum Essential Medium (MEM; Sigma Aldrich, Cat. No. M4655) and HeLa S3 cells in high-glucose Dulbecco's Modified Eagle Medium (DMEM) with GlutaMAX™ Supplement (ThermoFisher Scientific, Cat. No. 61965026) both supplemented with 10% fetal bovine serum (FBS; ThermoFisher). Cells were maintained at 37°C with 5% CO2.

2.7.2 Mammalian cell transfection

Kapβ1-EGFP, EGFP-CRM1, and Imp5-mCherry constructs were cloned into the pcDNA3.1(-) vector. The transfections were carried out using jetPRIME reagent (Polyplus-transfection® SA) according to the manufacturer's instructions.

2.7.3 Immunofluorescence

MDCK cells were plated on the glass coverslips (#1.5) allowing them to adhere for ~24h. Afterward, cells were rinsed twice with PBS (Sigma Aldrich) and fixed in 4% paraformaldehyde (PFA) (Sigma Aldrich, Cat. No. HT501128) for 15 min at room temperature (RT). Next, samples were washed three times for 5 min with PBS and permeabilized with 0.2 % Triton-X (in PBS). After three more washes with 1% BSA (Sigma Aldrich, Cat. No. A9647) in PBS for 5 min each, coverslips were left for >1h in 1% BSA solution for blocking. Subsequently, the primary antibodies against Kapβ1 (abcam, Cat. No. ab2811 (3E9)) and CRM1 (rabbit antibody, kind gift from R. Kehlenbach, University of Göttingen, Göttingen, Germany) (in 1% BSA) were applied for 1h at RT. Following another triple washing step (3x5 min in 1 % BSA), the samples were incubated with secondary antibodies (goat anti-mouse Alexa-568 (Thermo Fisher Scientific, Cat. No. A11004); goat anti-rabbit Alexa-488 (Thermo Fisher Scientific, Cat. No. A11034) and DAPI (Thermo Fisher, Cat. No. 62248) solution in 1 % BSA for 1 h at RT and protected from light. After the last washing step (3x5 min in 1 % BSA), coverslips were mounted onto glass slides with Vectashield medium (H-1000, Vector Laboratories) and sealed with nail polish. A similar procedure was applied in the case of transiently transfected cells (Chapter 2.4), except Triton permeabilization and antibody incubation steps were omitted.

2.7.4 Permeabilized cell assay

HeLa cells were plated into 8-well ibidi dishes and transfected with the fluorescent constructs of Kapβ1-EGFP, EGFP-CRM1, or Imp5-mCherry one day before experimentation. On the day of the experiment, cells were washed twice with PBS and permeabilized for 5 min with 40 µg/ml digitonin as reported previously (Adam et al., 1990). After three 5 min washes with PBS, cells were incubated with Ran mix (2 mM GTP, 0.1 mM ATP, 4 mM creatine phosphate, 20 U/ml creatine kinase, 5 µM RanGDP, 4 µM NTF2, and 1 mM DTT) for 1h at RT to estimate the level of Kapβ retention at the NPCs. In the final step, cells were washed three times to remove Ran Mix and leftover Kapβs. At each step of the treatment, the fluorescence signal of exogenous Kapβs was monitored using confocal microscopy (Fig. 2.4).

2.7.5 Confocal microscopy, imaging, and analysis

Fluorescence images of fixed samples were obtained at RT using the LSM880 inverted confocal microscope with an oil-immersed 63×/1.4 NA PLAN APO objective. The system was equipped

with a widefield camera and an Airyscan detector (ZEISS). Fluorescence quantification of cells transfected with Kapβ constructs was performed using CellProfiler software (Kamentsky et al., 2011). DAPI channel was used for initial image segmentation and nuclear envelope, nucleus, and cytoplasm regions of interest (ROIs) were created by shrinking or expanding the original DAPI-defined regions. The ROIs were used to quantify the mean fluorescence intensity across all channels. The number of analyzed cells per condition is specified in the figures. The quantification of NE fluorescence intensity from the permeabilized cells assay was performed using hand-drawn ROIs.

2.7.7 Global proteome analysis

2.7.6.1 Cells collection for MS

Control and siRNA-treated MDCK cell samples were collected as in other experiments, 48 h after transfection. Cells were washed with PBS, trypsinized (Sigma Aldrich, Cat. No. T3924-100ML) and automatically counted (LUNA-FL™ Dual Fluorescence Cell Counter, Logos Biosystems) following the Tryptan Blue (Sigma Aldrich, Cat. No. T8154) staining protocol. Next, 200 000 cells from each sample were collected and washed twice with cold PBS followed by 5 min spin at 10000 x g at 4 °C. Cell pellets were frozen at -80 °C until needed.

2.7.7.2 Sample preparation

Once all necessary biological replicates were collected, samples were processed according to the whole cell lysis and digestion using SDC, CAA, and PreOmics Cartridges for LC-MS/MS protocol. MDCK cells were thawed on ice and lysed in 50 µl lysis buffer (1% sodium deoxycholate (SDC), 0.1 M TRIS, 10 mM TCEP, pH = 8.5) using strong ultra-sonication (10 cycles, Bioruptor, Diagnode). Protein concentration was determined by BCA assay (Thermo Fisher Scientific) using a small sample aliquot. Sample aliquots containing 50 µg of total proteins were reduced for 10 min at 95 °C and alkylated at 15 mM chloroacetamide for 30 min at 37 °C. Proteins were digested by incubation with sequencing-grade modified trypsin (1/50, w/w; Promega, Madison, Wisconsin) overnight at 37°C. Then, the peptides were purified *via* solid-phase extraction using PR-Sulfonate Cartridges (SDB-RPS, PreOmics). First, 5% TFA was added to the samples followed by the addition of the wash buffer 1 (1% TFA in 2-propanol). In the next step, samples were transferred into the cartridges, spun down, and washed two more times with wash buffer 1. Then two washes were performed with wash buffer 2 (0.2% TFA in water) and purified peptides were eluted in two steps with the elution buffer (1% (v/v)

ammonium hydroxide, 19% water, and 80% acetonitrile). Collected eluates were dried under vacuum and stored at -20°C until further use.

2.7.7.2 LC-MS/MS

Dried peptides were resuspended in 0.1% aqueous formic acid and subjected to LC-MS/MS analysis using an Orbitrap Fusion Lumos Mass Spectrometer fitted with an EASY-nLC 1200 (both Thermo Fisher Scientific) and a custom-made column heater set to 60°C. Peptides were resolved using an RP-HPLC column (75µm × 36cm) packed in-house with C18 resin (ReproSil-Pur C18–AQ, 1.9 µm resin; Dr. Maisch GmbH) at a flow rate of 0.2 µLmin-1. The following gradient was used for peptide separation: from 5% B to 12% B over 5 min to 35% B over 90 min to 50% B over 25 min to 95% B over 2 min followed by 18 min at 95% B. Buffer A was 0.1% formic acid in water and buffer B was 80% acetonitrile, 0.1% formic acid in water.

The mass spectrometer was operated in DDA mode with a cycle time of 3 seconds between master scans. Each master scan was acquired in the Orbitrap at a resolution of 120,000 FWHM (at 200 m/z) and a scan range from 375 to 1500 m/z followed by MS2 scans of the most intense precursors in the linear ion trap at a “Rapid” scan rate with an isolation width of the quadrupole set to 1.4 m/z. Maximum ion injection time was set to 50ms (MS1) and 35 ms (MS2) with an automatic gain control (AGC) target set to 1e6 and 1e4, respectively. Only peptide ions with charge states 2 – 5 were included in the analysis. Monoisotopic precursor selection (MIPS) was set to Peptide, and the Intensity Threshold was set to 5e3. Peptides were fragmented by HCD (Higher-energy collisional dissociation) with collision energy set to 35%, and one microscan was acquired for each spectrum. The dynamic exclusion duration was set to 30s.

The acquired raw files were imported into the Progenesis QI software (v2.0, Nonlinear Dynamics Limited), which was used to extract peptide precursor ion intensities across all samples applying the default parameters. The generated mgf-files were searched using MASCOT against a decoy database containing normal and reverse sequences of the predicted SwissProt entries of *Canis Lupus familiaris* (www.ebi.ac.uk, release date 2019/06/11) and commonly observed contaminants (in total 51,776 sequences) generated using the SequenceReverser tool from the MaxQuant software (Version 1.0.13.13). The search criteria were set as follows: full tryptic specificity was required (cleavage after lysine or arginine residues, unless followed by proline); 3 missed cleavages were allowed; carbamidomethylation (C) was set as fixed modification; oxidation (M) and acetylation (Protein N-term) were applied as variable modifications; mass tolerance of 10 ppm (precursor) and 0.6 Da (fragments).

The database search results were filtered using the ion score to set the false discovery rate (FDR) to 1% on the peptide and protein level, respectively, based on the number of reverse protein sequence hits in the datasets. The relative quantitative data obtained were further normalized, statistically analyzed, and translated to absolute protein estimates (iBAQ values) using our in-house script (PMID:27345528).

2.7.7.3 Targeted LC-MS analysis

Targeted MS quantification was carried out as recently described (PMID: 32870689). Parallel reaction-monitoring (PRM) (DOI: 22865924) assays were generated from a mixture containing 50 fmol of each proteotypic heavy reference peptide (VAAGLQIK* and VLANPGNSQVAR*, JPT Peptide Technologies GmbH). Therefore, the 100 fmol of peptides were analyzed using a Q-Exactive HF coupled to an EASY nano-LC 1000 system (both Thermo Fisher Scientific), equipped with a heated RP-HPLC column (75 µm x 30 cm) packed in-house with 1.9 µm C18 resin (Reprosil-AQ Pur, Dr. Maisch). Peptides were analyzed per LC-MS/MS run using a linear gradient ranging from 95% solvent A (0.15% formic acid, 2% acetonitrile) and 5% solvent B (98% acetonitrile, 2% water, 0.15% formic acid) to 30% solvent B over 60 minutes at a flow rate of 200 nl/min. Mass spectrometer was operated in DDA mode with a cycle time of 3 seconds between master scans. Each master scan was acquired in the Orbitrap at a resolution of 120,000 FWHM (at 200 m/z) and a scan range from 300 to 1600 m/z followed by MS2 scans of the most intense precursors in the orbitrap at 30,000 FWHM (at 200 m/z) resolution with an isolation width of the quadrupole set to 1.4 m/z. Maximum ion injection time was set to 50 ms (MS1) and 50 ms (MS2) with an AGC target set to 1e6 and 1e5, respectively. Only peptides with charge states 2 – 5 were included in the analysis. Peptides were fragmented by HCD (Higher-energy collisional dissociation) with collision energy set to 28%, and one microscan was acquired for each spectrum. The dynamic exclusion duration was set to 30s.

The acquired raw files were searched using the MaxQuant software (Version 1.6.2.3) against the same *Canis Lupus familiaris* database mentioned above using default parameters except for protein, peptide, and site FDR were set to 1, and Lys8 and Arg10 were added as variable modifications. The best 6 transitions for each peptide were selected automatically using an in-house software tool and imported into SpectroDive (version 10, Biognosys, Schlieren). An unscheduled mass isolation list containing all peptide ion masses was exported from SpectroDive and imported into the Orbitrap Lumos operating software for PRM analysis.

Here, to each peptide sample, an aliquot of a heavy reference peptide mix containing chemically synthesized proteotypic peptides (Spike-Tides, JPT, Berlin, Germany) was spiked into each sample at a concentration of 2 fmol of heavy reference peptides per 1µg of total endogenous protein mass.

Aliquots containing 1 ug of peptides were subjected to targeted LC-MS analysis using Q-Exactive HF coupled to an EASY nano-LC 1000 system (both Thermo Fisher Scientific), equipped with a heated RP-HPLC column (75 µm x 30 cm) packed in-house with 1.9 µm C18 resin (Reprosil-AQ Pur, Dr. Maisch). Peptides were analyzed per LC-MS/MS run using a linear gradient ranging from 95% solvent A (0.15% formic acid, 2% acetonitrile) and 5% solvent B (98% acetonitrile, 2% water, 0.15% formic acid) to 30% solvent B over 60 minutes at a flow rate of 200 nl/min. For MS2, the resolution of the orbitrap was set to 120,000 FWHM (at 200 m/z), the fill time was set to 250 ms to reach an AGC target of 3e6, the normalized collision energy was set to 28%, the ion isolation window was set to 0.4 m/z and the first mass was fixed to 100 m/z. An MS1 scan from 350-1600 m/z at 120,000 resolution (at 200 m/z), AGC target 3e6 and fill time of 100 ms were included in each MS cycle. All raw files were imported into SpectroDive for protein/peptide quantification using default settings. To control for variation in injected sample amounts, the total ion chromatogram (only comprising ions with two to five charges) of each sample was determined using Progenesis as described above and used for normalization. All follow-up peptide abundance calculations were performed in Microsoft Excel, given that MDCK cells contain ~20% proteins per cell volume (Erlinger and Saier, 1982) and that protein cellular concentration is 300 mg/ml (Wiśniewski et al., 2014).

2.8 References

Abu-Arish, A., Kalab, P., Ng-Kamstra, J., Weis, K., and Fradin, C. (2009). Spatial distribution and mobility of the Ran GTPase in live interphase cells. Biophys J *97*, 2164-2178.

Adam, S.A., Marr, R.S., and Gerace, L. (1990). Nuclear-protein import in permeabilized mammalian-cells requires soluble cytoplasmic factors J Cell Biol *111*, 807-816.

Barbato, S., Kapinos, L.E., Rencurel, C., and Lim, R.Y.H. (2020). Karyopherin enrichment at the nuclear pore complex attenuates Ran permeability. J Cell Sci.

Celetti, G., Paci, G., Caria, J., VanDelinder, V., Bachand, G., and Lemke, E.A. (2020). The liquid state of FG-nucleoporins mimics permeability barrier properties of nuclear pore complexes. J Cell Biol *219*.

Chook, Y.M., and Süel, K.E. (2011). Nuclear import by karyopherin-βs: Recognition and inhibition. Biochimica et Biophysica Acta (BBA) - Molecular Cell Research *1813*, 1593-1606.

Christie, M., Chang, C.W., Rona, G., Smith, K.M., Stewart, A.G., Takeda, A.A., Fontes, M.R., Stewart, M., Vertessy, B.G., Forwood, J.K.*, et al.* (2016). Structural biology and regulation of protein import into the nucleus. J Mol Biol *428*, 2060-2090.

Conti, E., Muller, C.W., and Stewart, M. (2006). Karyopherin flexibility in nucleocytoplasmic transport. Curr Opin Struct Biol *16*, 237-244.

Erlinger, S.U., and M.H. Saier Jr. (1982). Decrease in protein content and cell volume of cultured dog kidney epithelial cells during growth. In Vitro *18*, 196–202.

Frey, S., and Görlich, D. (2007). A saturated FG-repeat hydrogel can reproduce the permeability properties of nuclear pore complexes. Cell *130*, 512-523.

Frey, S., and Görlich, D. (2009). FG/FxFG as well as GLFG repeats form a selective permeability barrier with self-healing properties. EMBO J *28*, 2554-2567.

Heaton, S.M., Atkinson, S.C., Sweeney, M.N., Yang, S.N.Y., Jans, D.A., and Borg, N.A. (2019). Exportin-1-Dependent Nuclear Export of DEAD-box Helicase DDX3X is Central to its Role in Antiviral Immunity. Cells *8*.

Jakel, S., and Gorlich, D. (1998). Importin beta, transportin, RanBP5 and RanBP7 mediate nuclear import of ribosomal proteins in mammalian cells. EMBO J *17*, 4491-4502.

Jovanovic-Talisman, T., Tetenbaum-Novatt, J., McKenney, A.S., Zilman, A., Peters, R., Rout, M.P., and Chait, B.T. (2009). Artificial nanopores that mimic the transport selectivity of the nuclear pore complex. Nature *457*, 1023-1027.

Kalita, J., Kapinos, L.E., and Lim, R.Y.H. (2021). On the asymmetric partitioning of nucleocytoplasmic transport - recent insights and open questions. J Cell Sci *134*.

Kamentsky, L., Jones, T.R., Fraser, A., Bray, M.A., Logan, D.J., Madden, K.L., Ljosa, V., Rueden, C., Eliceiri, K.W., and Carpenter, A.E. (2011). Improved structure, function and compatibility for CellProfiler: modular high-throughput image analysis software. Bioinformatics *27*, 1179-1180.

Kapinos, L.E., Huang, B., Rencurel, C., and Lim, R.Y.H. (2017). Karyopherins regulate nuclear pore complex barrier and transport function. J Cell Biol *216*, 3609-3624.

Kapinos, L.E., Schoch, R.L., Wagner, R.S., Schleicher, K.D., and Lim, R.Y.H. (2014b). Karyopherin-centric control of nuclear pores based on molecular occupancy and kinetic analysis of multivalent binding with FG nucleoporins. Biophys J *106*, 1751-1762.

Kirli, K., Karaca, S., Dehne, H.J., Samwer, M., Pan, K.T., Lenz, C., Urlaub, H., and Gorlich, D. (2015). A deep proteomics perspective on CRM1-mediated nuclear export and nucleocytoplasmic partitioning. Elife *4*.

Kuersten, S., Arts, G.J., Walther, T.C., Englmeier, L., and Mattaj, I.W. (2002). Steady-state nuclear localization of exportin-t involves RanGTP binding and two distinct nuclear pore complex interaction domains. Mol Cell Biol *22*, 5708-5720.

Lim, R.Y.H., Huang, B., and Kapinos, L.E. (2015). How to operate a nuclear pore complex by Kap-centric control. Nucleus *6*, 366-372.

Lowe, A.R., Tang, J.H., Yassif, J., Graf, M., Huang, W.Y., Groves, J.T., Weis, K., and Liphardt, J.T. (2015). Importin-beta modulates the permeability of the nuclear pore complex in a Ran-dependent manner. Elife *4*.

Makise, M., Mackay, D.R., Elgort, S., Shankaran, S.S., Adam, S.A., and Ullman, K.S. (2012). The Nup153-Nup50 protein interface and its role in nuclear import. J Biol Chem *287*, 38515-38522.

Nguyen, T., Pappireddi, N., and Wuhr, M. (2019). Proteomics of nucleocytoplasmic partitioning. Curr Opin Chem Biol *48*, 55-63.

Ogawa, Y., Miyamoto, Y., Oka, M., and Yoneda, Y. (2012). The interaction between importin-alpha and Nup153 promotes importin-alpha/beta-mediated nuclear import. Traffic *13*, 934-946.

Pulupa, J., Prior, H., Johnson, D.S., and Simon, S.M. (2020). Conformation of the nuclear pore in living cells is modulated by transport state. Elife *9*.

Schoch, R.L., Kapinos, L.E., and Lim, R.Y.H. (2012). Nuclear transport receptor binding avidity triggers a self-healing collapse transition in FG-nucleoporin molecular brushes. Proc Natl Acad Sci USA *109*, 16911-16916.

Smith, A.E., Slepchenko, B.M., Schaff, J.C., Loew, L.M., and Macara, I.G. (2002). Systems analysis of Ran transport. Science *295*, 488-491.

Swale, C., Da Costa, B., Sedano, L., Garzoni, F., McCarthy, A.A., Berger, I., Bieniossek, C., Ruigrok, R.W.H., Delmas, B., and Crepin, T. (2020). X-ray Structure of the Human Karyopherin RanBP5, an Essential Factor for Influenza Polymerase Nuclear Trafficking. J Mol Biol *432*, 3353-3359.

Tan, P.S., Aramburu, I.V., Mercadante, D., Tyagi, S., Chowdhury, A., Spitz, D., Shammas, S.L., Grater, F., and Lemke, E.A. (2018). Two Differential Binding Mechanisms of FG-Nucleoporins and Nuclear Transport Receptors. Cell Rep *22*, 3660-3671.

Tetenbaum-Novatt, J., Hough, L.E., Mironska, R., McKenney, A.S., and Rout, M.P. (2012). Nucleocytoplasmic transport: a role for nonspecific competition in karyopherin-nucleoporin interactions. Mol Cell Proteomics *11*, 31-46.

Uversky, V.N. (2013). Unusual biophysics of intrinsically disordered proteins. Biochimica Et Biophysica Acta-Proteins and Proteomics *1834*, 932-951.

Vovk, A., Gu, C., Opferman, M.G., Kapinos, L.E., Lim, R.Y., Coalson, R.D., Jasnow, D., and Zilman, A. (2016). Simple biophysics underpins collective conformations of the intrinsically disordered proteins of the Nuclear Pore Complex. Elife *5*.

Wagner, R.S., Kapinos, L.E., Marshall, N.J., Stewart, M., and Lim, R.Y.H. (2015). Promiscuous binding of Karyopherinbeta1 modulates FG nucleoporin barrier function and expedites NTF2 transport kinetics. Biophys J *108*, 918-927.

Wang, M., Herrmann, C.J., Simonovic, M., Szklarczyk, D., and von Mering, C. (2015). Version 4.0 of PaxDb: Protein abundance data, integrated across model organisms, tissues, and cell-lines. Proteomics *15*, 3163-3168.

Wiśniewski, J.R., M.Y. Hein, J. Cox, and M. Mann. (2014). A "proteomic ruler" for protein copy number and concentration estimation without spike-in standards. Mol. Cell. Proteomics *13*, 3497–3506.

Wühr, M., Guttler, T., Peshkin, L., McAlister, G.C., Sonnett, M., Ishihara, K., Groen, A.C., Presler, M., Erickson, B.K., Mitchison, T.J.*, et al.* (2015). The Nuclear Proteome of a Vertebrate. Curr Biol *25*, 2663-2671.

Yang, W., and Musser, S.M. (2006). Nuclear import time and transport efficiency depend on importin beta concentration. J Cell Biol *174*, 951-961.

Zahn, R., Osmanovic, D., Ehret, S., Araya Callis, C., Frey, S., Stewart, M., You, C., Gorlich, D., Hoogenboom, B.W., and Richter, R.P. (2016). A physical model describing the interaction of nuclear transport receptors with FG nucleoporin domain assemblies. Elife *5*.

Zilman, A. (2018). Aggregation, Phase Separation and Spatial Morphologies of the Assemblies of FG Nucleoporins. J Mol Biol *430*, 4730-4740.

Chapter 3

Binding of Kapβs *in vitro* and *ex vivo*

Adapted from

Karyopherin enrichment and compensation fortifies the nuclear pore complex against nucleocytoplasmic leakage

Joanna Kalita, Larisa E. Kapinos, Tiantian Zheng, Chantal Rencurel, Anton Zilman and Roderick Y. H. Lim

Published in Journal of Cell Biology, 221(3), jcb.202108107 (2022)

3.1 Surface Plasmon Resonance (SPR)

Surface Plasmon Resonance (SPR) is an analytical biosensing technique that allows for real-time monitoring of molecular binding events that occur in proximity to the sensor surface (Homola, 2008). As such, SPR is routinely used to measure multivalent binding of Kapβs to surface-tethered FG Nups and the corresponding conformational changes of the FG Nup layer (Kapinos et al., 2014; Schoch et al., 2012). This approach allows for the measurement of FG Nup surface density, conformational height change, as well as Kapβ-FG Nup equilibrium constants and their binding kinetics. In this work, we utilized SPR to compare CRM1 and Imp5 binding to the FG Nups from different sites of NPC, namely, cytoplasmic Nup214 (cNup214), central Nup62, and Nup98 (cNup62 and cNup98), and nucleoplasmic Nup153 (cNup153). The data for Kapβ1 has been reproduced from Kapinos et al., 2017.

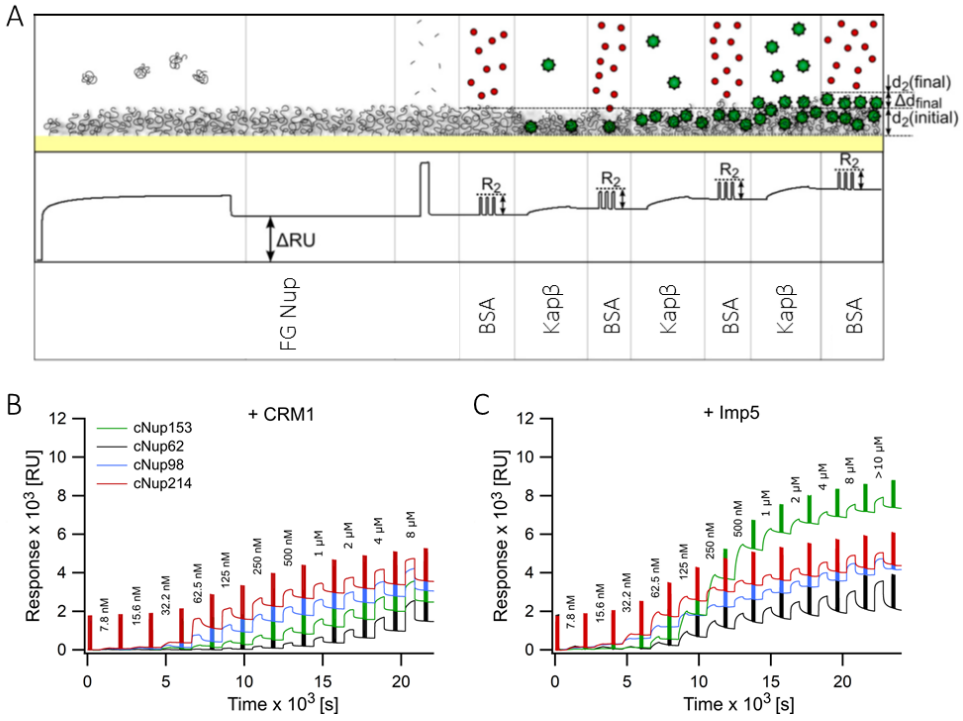

***Figure 3.1** Binding of CRM1 and Imp5 to FG Nup layers.*

(A) SPR experimental design. Kapβ binding and the corresponding FG Nup height changes were measured by recording the SPR signal (RU) upon incubation of FG Nups with increasing concentrations of the analyte (Kapβ). After each titration step BSA solution was injected into the flow chamber in order to monitor the changes in the FG Nup layer height (Δd). SPR response curves obtained for (B) CRM1 and (C) Imp5 binding to cNup153 (green), cNup62 (black), cNup98 (blue) and cNup214 (red). Vertical jumps in the signal correspond to triple BSA injections used to measure FG Nup layer height. RU, resonance units. Panel A was adapted from Schoch et al., 2012.

3.2 Measurement of Kapβ binding constants

The apparent equilibrium binding constant ($K_{D,SPR}$) was obtained by monitoring the SPR response (RU) in the channels with immobilized FG Nups upon CRM1 or Imp5 titration (Fig. 3.1). Considering that the Kapβ-FG Nup equilibrium binding response strongly depends on the initial FG Nup surface density (Kapinos et al., 2014; Schoch et al., 2012), we restricted the analysis to the measurements obtained in the closed-packed FG Nup regime, as indicated by grafting distance calculations (Chapter 3.9.8.1).

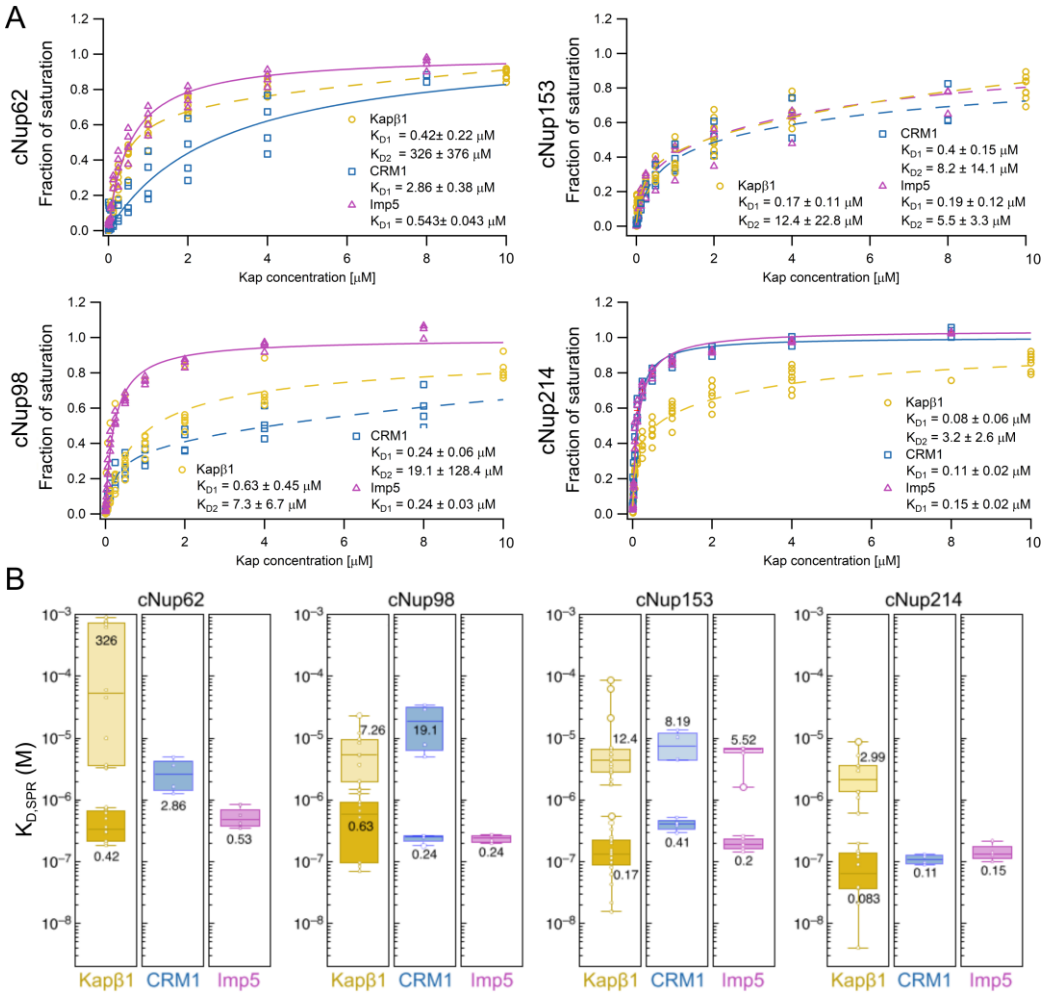

Figure 3.2 Equilibrium analysis of Kapβ-FG Nup binding.

(A) Equilibrium binding analysis of Kapβ1 (yellow), CRM1 (blue), and Imp5 (magenta) to cNup62, cNup98, cNup153, and cNup214. Lines represent single- (solid) or two-component (dashed) Langmuir isotherm fits to the average SPR equilibrium response (R_{eq}). The mean apparent dissociation constant calculated from n≥4 replicates was used for the fitting. For each replicate, data points were normalized to the maximum response value (R_{max}) or their sum (R_{max1} and R_{max2}) obtained from the equilibrium fit. (B) Equilibrium dissociation constants for Kapβ1 (yellow), CRM1 (blue), and Imp5 (magenta) binding to cNup62, cNup98, cNup153, and cNup214. Boxplots denote the median, first and third quartiles. $K_{D,SPR}$s correspond to the mean values from n≥4 measurements at each condition. Error bars denote standard deviation. Note: The Kapβ1 data was reproduced from Kapinos et al., 2017.

For each tested Kapβ-FG Nup pair, the $K_{D,SPR}$ values were obtained by fitting the SPR equilibrium response (R_{eq}) with a single- or two-component Langmuir isotherm (Fig. 3.2A). Such equilibrium analysis reveals that CRM1 exhibits two phase-binding to cNup98 and cNup153 with $K_{D,SPR}$ comparable to Kapβ1, while single phase-binding is characteristic for interactions with cNup62 and cNup214. Additionally, CRM1 binding to cNup62 is significantly weaker ($K_{D,SPR}$ = 2.86 ± 0.38 µM) than the strong phase of Kapβ1 ($K_{D,SPR}$ = 0.42 ± 0.022 µM), whereas the binding of CRM1 to cNup214 is comparable (CRM1 $K_{D,SPR}$ = 0.11 ± 0.02 µM vs. Kapβ1 $K_{D,SPR}$= 0.08 ± 0.06 µM) being consistent with previous reports (Port et al., 2015) (Fig. 3.2B). Moreover, Imp5 exhibits single phase-binding to the tested FG Nups except for cNup153. Nevertheless, all $K_{D,SPR}$ values of Imp5 are comparable with the strong binding phase of Kapβ1 and CRM1.

3.3 Analysis of Kapβ binding kinetics

Next, we analyzed the kinetic association (k_{on}) and dissociation (k_{off}) rate constants of CRM1 and Imp5 to and from the FG Nup layers and compared their behavior against Kapβ1 (Fig. 3.3A). The resulting kinetic maps show a distribution of K_Ds (where $K_D = k_{off}/k_{on}$) that manifest from a constellation of k_{on} and k_{off} values, being characteristic of multivalent binding (Fig. 3.3B) (Svitel et al., 2003; Svitel et al., 2007). Both CRM1 and Imp5 exhibit kinetic behavior that commences with a high avidity slow-phase (✱, Fig. 3.3) at low concentrations that is characterized by fast k_{on} (~10^3 to 10^4 $s^{-1}M^{-1}$) and slow k_{off} (10^{-5} to 10^{-4} s^{-1}). Increasing CRM1/Imp5 concentration towards the 10^{-6} M range brings about a steady reduction in k_{on} towards 10 $s^{-1}M^{-1}$ (○, Fig. 3.3), which indicates a decrease in binding avidity (increasing K_D). This is accompanied by the emergence of a fast-binding phase (▲, Fig. 3.3) that coincides with an increase in k_{on} (>10^3 $s^{-1}M^{-1}$) and a fast k_{off} (>10^{-1} s^{-1}). Indeed, the slow and fast phases are constrained by half-lives ($t_{1/2}$) that span a range of between 20 h and 7 s, respectively, where $t_{1/2} = \ln(2)/k_{off}$. Hence, a key result is that Imp5 exhibits a higher propensity to depart from the FG Nups in the slow phase than Kapβ1 and CRM1 given its faster k_{off} as evidenced by its low enrichment *in vivo* (Fig. 2.1 and Fig. 2.3). Otherwise, the transient binding fast phase that follows is qualitatively similar across all Kapβs although with a slight increase in the transient fraction of Imp5 over Kapβ1 and CRM1.

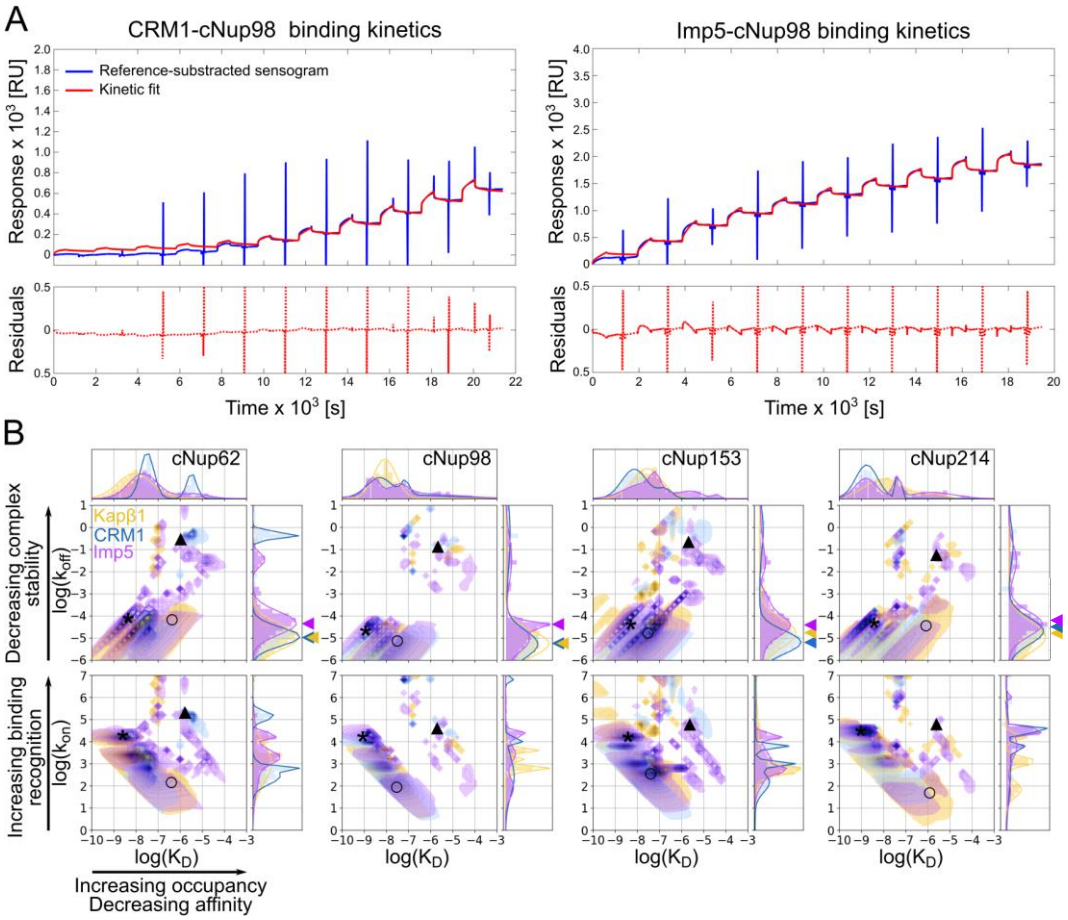

Figure 3.3 Kinetic analysis of Kapβ-FG Nup interactions

(A) Examples of kinetic analysis of CRM1 and Imp5 binding to cNup98. Reference-subtracted traces (blue) and corresponding kinetic fits (red) are visualized. Bottom panels show fit residuals. (B) Kinetic maps of Kapβ1 (yellow), CRM1 (blue), and Imp5 (magenta) binding to cNup62, cNup98, cNup153, and cNup214. Each map was constructed by averaging over at least four sensograms for every Kapβ-FG Nup pair. The color intensity indicates the fractional abundance of different kinetic states. All Kapβs exhibit multivalent binding and their kinetic behavior is characterized by different kinetic phases: high-affinity (✱), low-affinity fast (◢), and low-affinity slow (○). Arrowheads point to the mean fitted k_{off} value for each Kapβ. The data for Kapβ1 has been reproduced from Kapinos et al., 2017.

3.4 Molecular occupancy of Kapβs within FG Nup layers

As mentioned, the SPR response increases proportionally to the mass of the molecules adsorbed on the sensor's surface. With the prior knowledge of the SPR calibration factor (1300 RU = 1 ng/mm^2 for proteins directly tethered to the gold surface), molecular weight (M.W.), and size obtained by dynamic light scattering (DLS) and Small-angle X-ray scattering (SAXS) (Feigin and Svergun, 1987; Schoch et al., 2012) it is possible to estimate the number of Kapβ molecules bound per unit area. Therefore, in the context of our SPR measurements, we were able to calculate the effective number of layers that each Kapβ forms

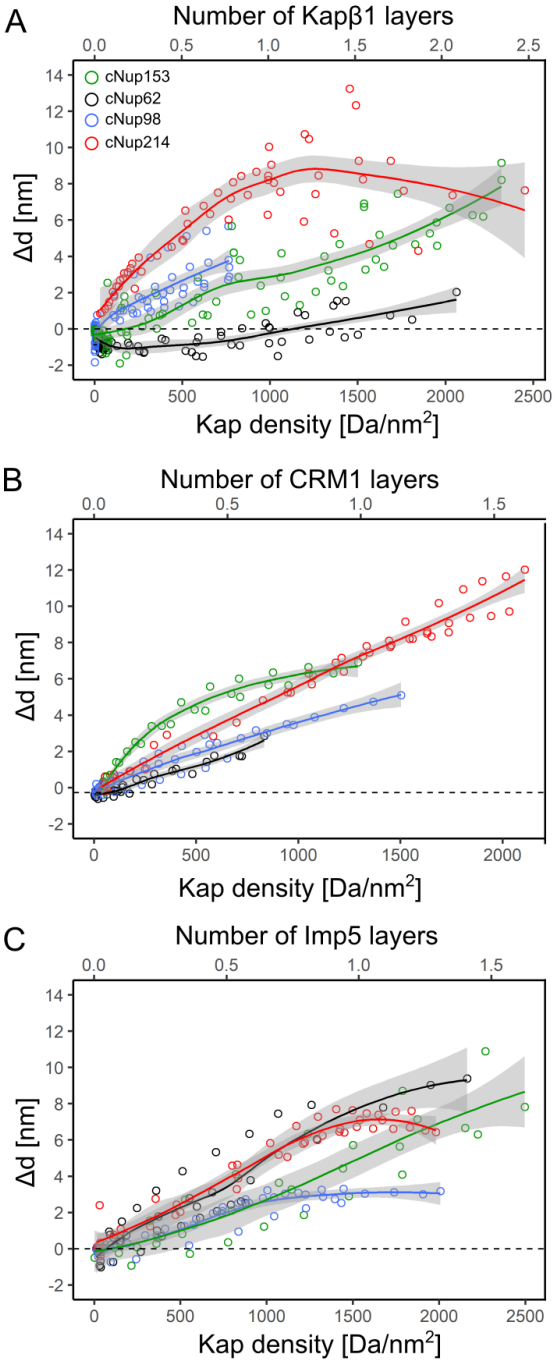

Figure 3.4 FG Nup layer height is determined by the interacting Kapβ

Changes in FG Nup layer height as a function of (A) Kapβ1, (B) CRM1 and (C) Imp5 surface density for cNup153 (green), cNup62 (black), cNup98 (blue), and cNup214 (red). The full range of obtained data points is shown for CRM1 and Imp5, while for Kapβs only points <2500 Da/nm² are plotted. For the full data set see Kapinos et al., 2014 from where the data for Kapβ1 has been reproduced. All data points were smoothed using the Loess method with span = 0.7 and confidence interval set to 0.95 (grey).

upon binding to the FG Nups at a given concentration. In parallel, we monitored the changes in the FG Nup layer height *via* triple BSA injections after each Kapβ titration step (methodology described in detail in (Kapinos et al., 2014; Schoch et al., 2012; Schoch and Lim, 2013).

The change in the FG Nup layer thickness (Δd) shown as a function of bound Kapβ surface density, reveals differences in the degree of FG Nup expansion and the ability of Kapβs to permeate into each respective FG Nup layer. The most striking observation is that at low occupancy (<1000 Da/nm^2), only Kapβ1 causes a significant collapse of the cNup62 layer (Fig. 3.4A, black trace), while CRM1 and Imp5 binding results exclusively in the increase of the FG Nup height. Additionally, unlike Kapβ1 and Imp5, CRM1 does not seem to efficiently permeate into the cNup62 layer accumulating below 800 Da/nm^2 surface density (Fig. 3.4B), still causing FG Nup expansion comparable to Kapβ1 at 2000 nm^2. Moreover, Kapβ1 and Imp5 binding to cNup153 shows an almost linear correlation between Kapβ occupancy and FG Nup layer height change (Fig. 3.4A, C, green trace, for Kapβ1 this also holds above 2500 Da/nm^2 (data not shown, see Kapinos et al., 2014), whereas cNup153 expands by a maximum 6 nm already before CRM1 accumulation at ~1 layer.

Interestingly, the reverse situation appears to take place for cNup214 (Fig. 3.4B). Increasing CRM1 density increases cNup214 height, while height expansion caused by Kapβ1 and Imp5 ceases once one layer of these Kapβs is formed. Moreover, a slight collapse of cNup214 height is observed upon further addition of Kapβ1 or Imp5. In the case of cNup98, the amount corresponding to ~1 level of each Kapβ permeates into this FG Nup layer causing its expansion by a maximum of 5 nm (~3 nm for Imp5).

3.5 Concentration-dependent binding of exoKapβs to NPCs *ex vivo*

Differences in Kapβ binding affinity and their kinetic rates may be amplified by the presence of specific and unspecific competitors within the cell milieu (Tetenbaum-Novatt et al., 2012). This aspect, however, cannot be easily resolved using SPR technology. Instead, we extended a permeabilized cell assay (Adam et al., 1990) as a novel approach to study the binding and competition of various Kapβs to the NPCs. First, HeLa cells were permeabilized with digitonin and treated with Ran mix to deplete endogenous Kapβs (endoKapβs) from the NPCs (Fig. 2.4) (Barbato et al., 2020; Kapinos et al., 2017; Pulupa et al., 2020). Subsequently, these permeabilized endoKapβ-depleted cells were incubated in separate solutions, or mixtures of thereof, containing fluorescently labeled exogenous Kapβ1, CRM1, or Imp5 (denoted exoKapβ1, exoCRM1, and exoImp5) (Fig. 3.5A).

Initially, we sought to examine standalone Kapβ1, CRM1, and Imp5 *ex vivo* binding affinities to NPCs. Thus, we incubated endoKapβ-depleted cells with mixtures containing increasing concentrations of Kapβ1-Alexa Fluor 488, CRM1-Alexa Fluor 647, or Imp5-Alexa Fluor 647 (Fig. 3.5B-D). Despite the molecular complexity of the NPC, incubation with each Kapβ yielded characteristic binding curves based on their respective fluorescence signals ($F_{NPC,norm}$), which indicated concentration-dependent enrichment at the NPCs (Fig. 3.5B-E). Although the behavior of exoKapβ1 and exoCRM1 was consistent with *in vivo* observations (Fig. 2.1 and Fig. 2.3), the strong rim-staining of exoImp5 was rather surprising, though, based on the SPR results (Fig. 3.2), not completely unexpected. Consistent with the SPR equilibrium binding analysis, the apparent binding constant of each exoKapβ to the NPC ($K_{D,NPC}$) was determined by fitting the Langmuir isotherm yielding 3.1 ± 1.2 µM, 0.50 ± 0.15 µM, and 0.68 ± 0.10 µM for exoKapβ1, exoCRM1, and exoImp5, respectively.

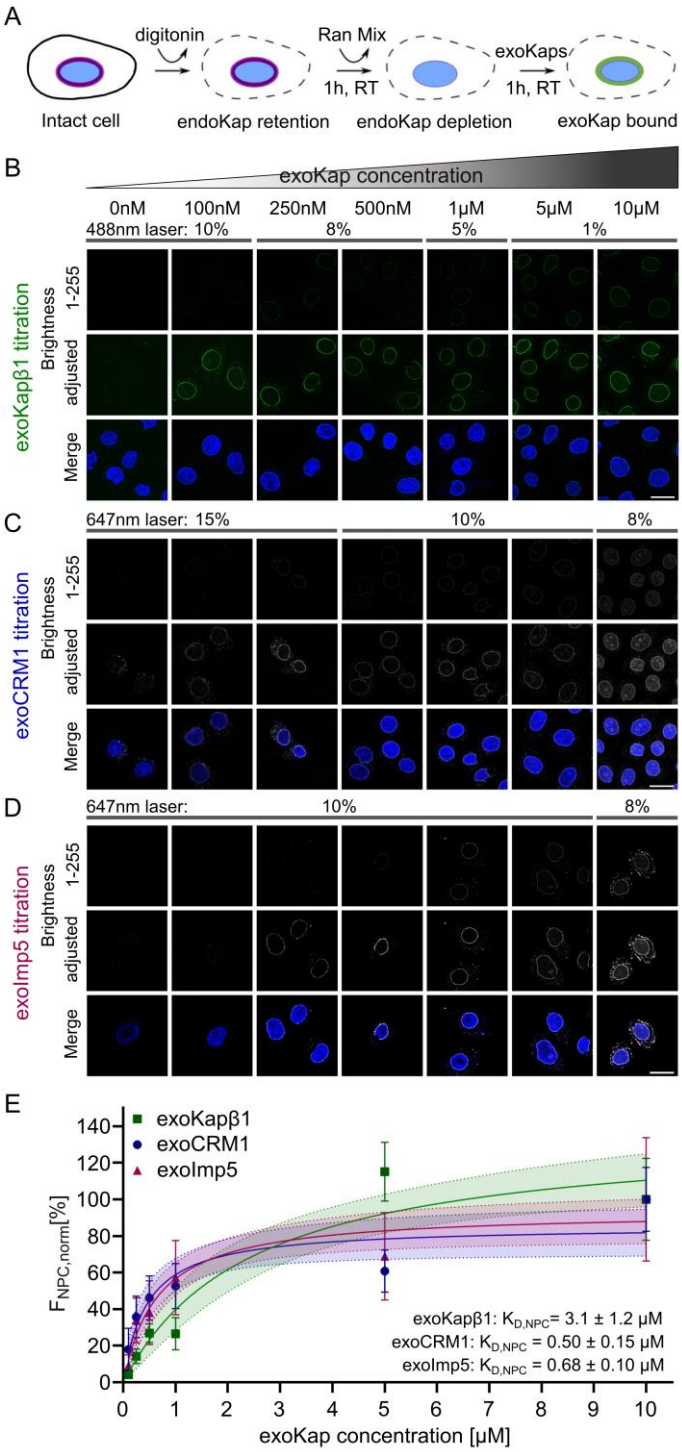

Figure 3.5 Kapβ1, CRM1, and Imp5 bind to NPCs in a concentration-dependent manner

(A) Experimental sequence. (B-D) Representative images of permeabilized HeLa cells incubated in increasing concentrations of (B) exoKapβ1, (C) exoCRM1, and (D) exoImp5. The concentration-dependent accumulation of each exoKapβ is measured from their respective nuclear rim stainings. Cells in the first row are shown with the same dynamic range settings. The brightness is adjusted in the second row to improve the visibility of the nuclear rim. Percentages indicate the laser power used to image the cells. Representative images were chosen from the same dataset. (E) Quantification of exoKapβ1 (green), exoCRM1 (blue), and exoImp5 (magenta) at the NPCs and normalized by the maximum fluorescence measured for each Kapβ at 10 µM. The apparent binding affinities were obtained by fitting a single-component Langmuir isotherm to each respective dataset. Data points, error bars, and $K_{D,NPC}$ values were obtained by propagating means and errors across all replicates (n ≥ 3). Scale bars: 20 µm.

Noting that in this assay exoKapβ1 gave the weakest $K_{D,NPC}$ value, we asked if the remaining 8% of endoKapβ1 at the NPC (Fig. 2.4) could have impacted these measurements. Using SPR data (Kapinos et al., 2017), we simulated a similar scenario by assigning the initial condition for Langmuir isotherm analyses at ~10% Kapβ1 pre-loading (Fig. 3.6). This is justified as the initial condition in a typical SPR measurement comprises of a pristine FG Nup layer. The offset simulation that uses Kapβ1 binding to the mix FG Nup layer demonstrates that pre-loading indeed shifts Kapβ1 $K_{D,SPR}$ to weaker values from $K_{D1,SPR}$ = 0.416 μM to K_D = 1.11 μM. This observation is consistent with decreasing Kapβ1 avidity upon the increase of its occupancy shown in SPR measurements (Fig. 3.3B) (Kapinos et al., 2017; Kapinos et al., 2014; Schoch et al., 2012; Wagner et al., 2015) and in FG Nup-tethered nanopores (Malekian et al., 2018).

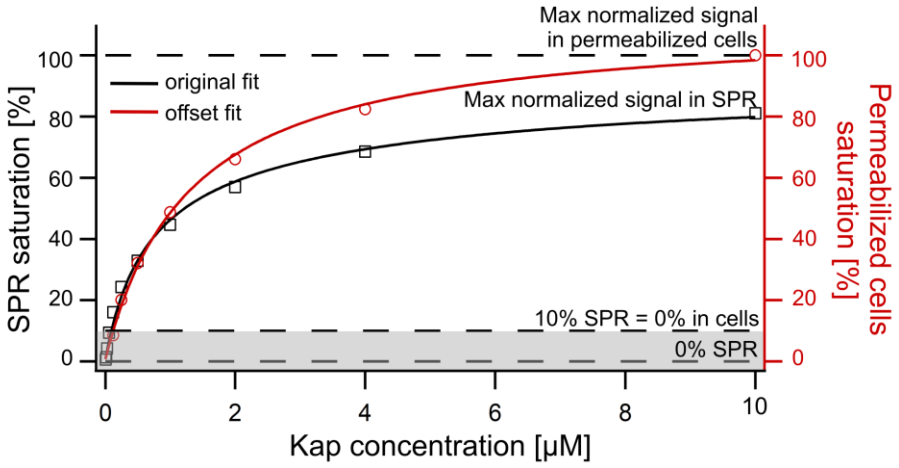

Figure 3.6 Kapβ1 pre-loading shifts K_D to weaker values

Effect of 10% Kapβ1 occupancy on Langmuir isotherm analysis simulated using SPR data. This simulation utilizes SPR data of Kapβ1 binding to a mixed FG Nup layer comprising of cNup62, cNup98, cNup153, and cNup214. The Langmuir fit to the original data (black) gives $K_{D1,SPR}$ = 0.416 μM and $K_{D2,SPR}$ = 393 μM. This data is then offset by 10% occupancy to simulate the effect of 10% pre-loading in permeabilized cells (see Fig. 3.5E). The Langmuir fit to the offset data (red) gives K_D = 1.11 μM. The original data (black) was taken from Kapinos et al., 2017.

3.6 Competitive binding of Kapβs to NPCs in permeabilized cells

Given that Kapβ1 and CRM1 co-enrich at NPCs (Fig. 2.1 and Fig. 2.3), we decided to test for their pairwise binding in endoKapβ-depleted HeLa cells. Knowing the binding characteristics of standalone exoCRM1 (Fig. 3.5E) allowed us to evaluate changes to its binding at NPCs within a constant background of 10 μM exoKapβ1. Conversely, changes in exoKapβ1 occupancy with respect to exoCRM1-binding were also monitored. However, only comparisons between their relative occupancies were considered because the fluorescence signals of exoKapβ1

and exoCRM1 were: (i) derived from different fluorophores and labeling efficiencies; and (ii) independently normalized.

At 10 µM concentrations, the relative occupancy of exoCRM1 reduced by 51 ± 23 % from its standalone value and was coupled to a 62 ± 23 % relative occupancy for exoKapβ1. This was accompanied by an increase (weakening) in exoCRM1 binding which $K_{D,NPC}$ shifted to 2.8 ± 1.5 µM being ~6-fold weaker than when exoKapβ1 was absent (Fig. 3.7A, B). Separately, a pairwise binding of exoImp5 and exoKapβ1 resulted in an 84 ± 34 % reduction in the relative occupancy of exoImp5 while the final occupancy of exoKapβ1 stabilized at 72 ± 14 %. In this case of Kapβ competition, $K_{D,NPC}$ for exoImp5 increased to 5.2 ± 2.5 µM which is ~8-fold weaker than its standalone value (Fig. 3.7C, D). Moreover, the pairwise binding of exoImp5 and 10 µM exoCRM1 led to a 56 ± 35 % decrease in the relative occupancy of exoImp5 and equilibration of exoCRM1 at 59 ± 26 % of its maximal occupancy. CRM1 vs. Imp5 competition resulted in lowering $K_{D,NPC}$ for exoImp5 to 2.0 ± 0.6 µM, which is ~3-fold weaker than exoImp5 standalone value.

Close inspection of the collected data also indicates that for all tested Kapβ pairs, their co-accumulation causes a reduction in the relative occupancy of the background exoKapβ. Using a Langmuir-like decay constant (K_{decay}), we identified the concentrations of CRM1 and Imp5 at which 50% of the maximum decay of exoKapβ1 had occurred. This gave 0.04 ± 0.03 µM and 0.03 ± 0.01 µM for CRM1 and Imp5, respectively. Furthermore, the value of 0.06 ± 0.04 µM was obtained for exoCRM1 decay during exoImp5 titration. Hence, already small concentrations of CRM1 or Imp5 are sufficient to displace 30- 40% of Kapβ1 from the NPC.

The *ex vivo* experiments performed in the permeabilized cells provided a global view of the promiscuous interactions of Kapβ1, CRM1, and Imp5 at NPCs. Moreover, the qualitative trends suggest that exoKapβ1 exhibits a higher propensity to outcompete against exoImp5 than exoCRM1, which is comparable to the competition between exoImp5 and exoCRM1.

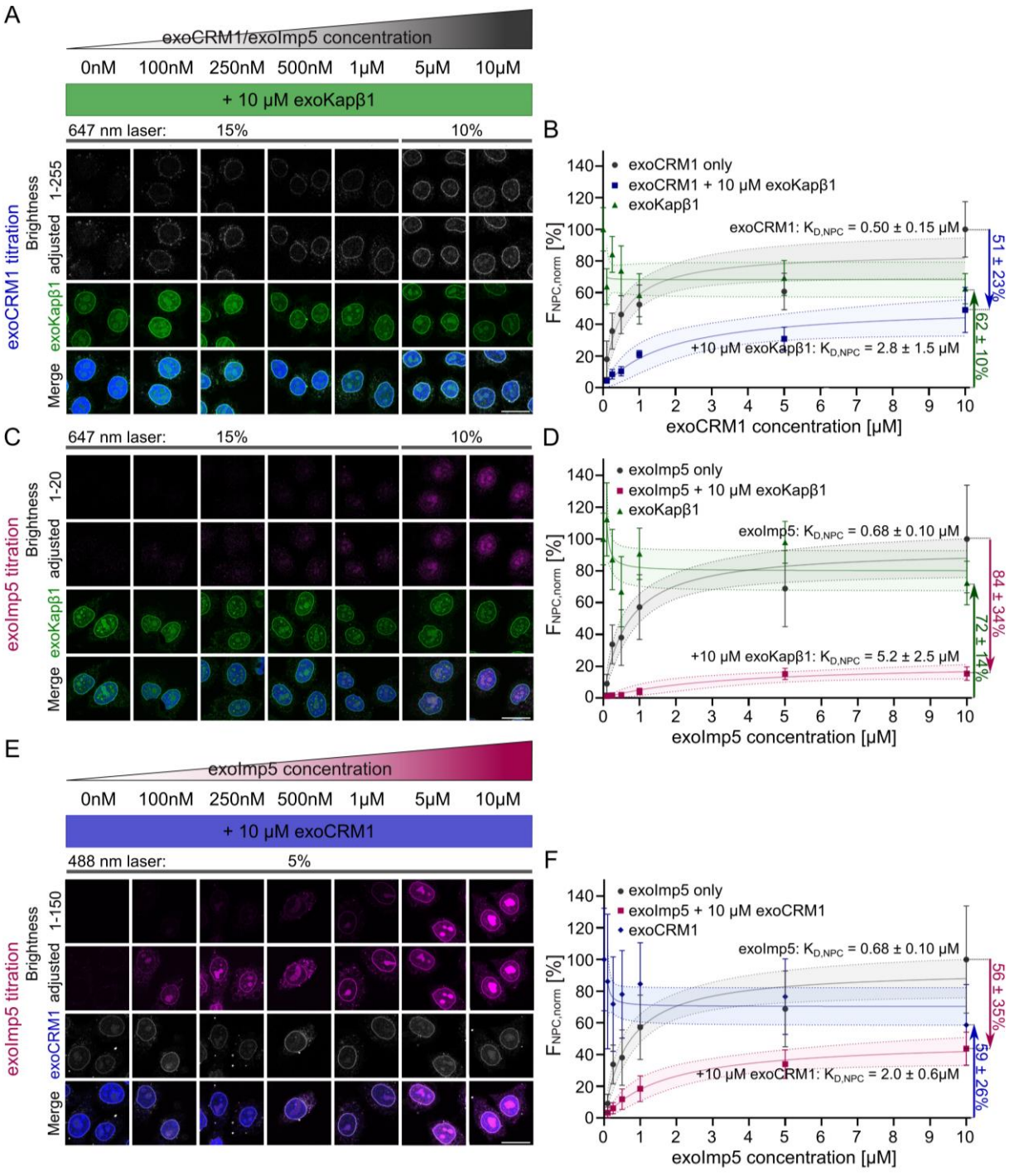

Figure 3.7 Pairwise binding reveals the relative occupancies for different Kapβs *(see the next page)*

3.7 Biophysical basis of Kapβ competition at the NPC

Note to reader: This section is a kind contribution from Tiantian Zheng and Anton Zilman

To complement our experimental results, we sought a more detailed understanding of how the relative occupancies of different Kapβ pairs are influenced by their promiscuous binding with the FG Nups. This was not possible to measure by SPR due to similarities in mass and K_Ds for Kapβ1, CRM1, and Imp5, i.e., compare with Kapβ1 and NTF2 (Wagner et al., 2015). Hence, we adopted a minimal theoretical model that is able to capture and explain the experimentally observed behavior of Kapβ partitioning into FG Nup assemblies (Vovk et al., 2016). In brief, the molecular details of Kapβ-FG Nup binding are subsumed into a phenomenological free energy parameter ϵ, which accounts for the free energy upon the entry of a single Kapβ molecule into the NPC. This term implicitly accounts for multivalent binding between the Kapβs and FG Nups, as well as the internal cohesiveness and the density of the FG Nups (see Chapter 3.9.11 for details). Then by specifying the volume ratios (Voss and Gerstein, 2010) of the Kapβs (Kapβ1 : CRM1 : Imp5 = 1 : 1.3 : 1.2; PDB: 3nd2, 4fgv, 3w3t, respectively) and including the free energy cost of competition for space inside the NPC between Kapβ molecules, we could compute changes in the relative occupancy of Kapβs (i.e., Δ) during pairwise binding.

Interestingly, the model correctly predicts the Δ values for CRM1 and Imp5 during pairwise binding with Kapβ1 within the range of $K_{D,SPR}$ values measured for each particular Kapβ

Figure 3.7 Pairwise binding reveals the relative occupancies for different Kapβs

(A) exoCRM1 titration in the presence of 10 μM exoKapβ1. (B) Normalized fluorescence signals of exoCRM1 and exoKapβ1 plotted as a function of exoCRM1 concentration. The maximal observed change in the relative occupancy of exoCRM1 is obtained by subtracting its titration value (blue) from its standalone value (gray) at the highest concentration (i.e., 10 μM exoCRM1; blue arrow). The relative occupancy of exoKapβ1 obtained in the presence of 10 μM exoCRM1 is also shown (green arrow). A single-component Langmuir isotherm fit provides the $K_{D,NPC}$ of exoCRM1 in the presence of 10 μM exoKapβ1. (C) exoImp5 titration in the presence of 10 μM exoKapβ1. (D) Normalized fluorescence signals of exoImp5 and exoKapβ1 plotted as a function of exoImp5 concentration. The maximal observed change in the relative occupancy of exoImp5 is obtained by subtracting its titration value (magenta) from its standalone value (gray) at 10 μM exoImp5 (magenta arrow). The relative occupancy of exoKapβ1 obtained in the presence of 10 μM exoImp5 is also shown (green arrow). (E) Titration of exoImp5 in the presence of 10 μM exoCRM1. (F) Normalized fluorescence signals of exoImp5 and exoCRM1 plotted as a function of exoImp5 concentration. The maximal observed change in the relative occupancy of exoImp5 is obtained by subtracting its titration value (magenta) from its standalone value (gray) at 10 μM exoImp5 (magenta arrow). The relative occupancy of exoCRM1 obtained in the presence of 10 μM exoImp5 is also shown (blue arrow). Cells in the first row are visualized within the dynamic range shown. The brightness has been adjusted in each second row to better visualize the nuclear rim. Percentages above the panels indicate the laser power used to image the cells. Data points, error bars, and $K_{D,NPC}$ values were obtained by propagating means and errors across all replicates ($n \geq 3$). Scale bars, 20 μm.

(Fig. 3.8A, B). The same is true for the pairwise binding of Imp5 and CRM1 (Fig. 3.8C). Likewise, the model also predicts the corresponding relative changes in Kapβ1 occupancy with respect to the experimental results of its pairwise binding with Imp5 and CRM1 (Fig. 3.9) and serves as a "boot-strapping" verification of the model. Hence, this coarse-grained model complements and consolidates our experimental findings (Fig. 3.7), where exoKapβ1 efficiently outcompetes exoImp5 but not exoCRM1, and exoCRM1 does not seem to exclude exoImp5. Taken together, the relative occupancy of different Kapβs at the NPC is balanced by Kapβ size, Kapβ abundance, and their binding affinity to the FG Nups and provides a basis for more detailed modeling.

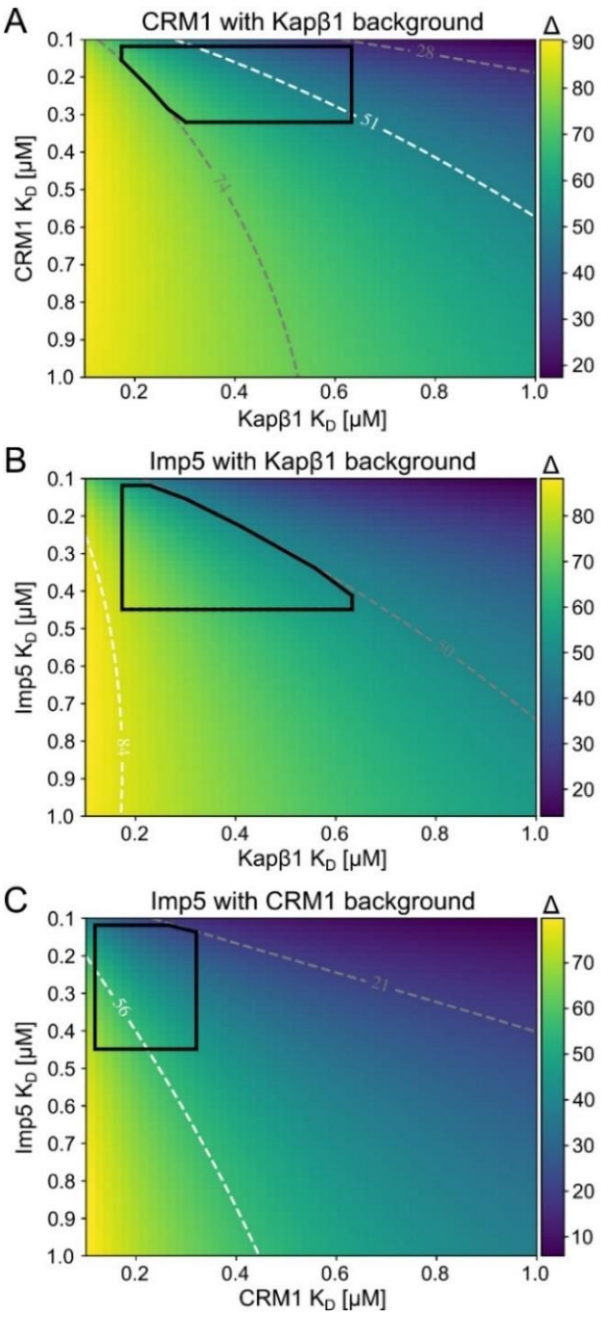

Figure 3.8 Promiscuous binding is balanced by Kapβ size, binding affinity, and abundance
(A) Theoretically predicted shift in the occupancy of CRM1 from its standalone value at 10 μM CRM1 compared to the presence of 10 μM Kapβ1 background (blue arrow in Fig. 3.7B), as a function of CRM1 and Kapβ1 K_D values.
(B) Theoretically predicted shift in the pore occupancy of Imp5 from its standalone value at 10 μM Imp5 to when a background of 10 μM Kapβ1 is present (magenta arrow in Fig. 3.7D), as a function of Imp5 and Kapβ1 K_D values.
(C) Theoretically predicted shift in the relative occupancy of Imp5 from its standalone value at 10 μM Imp5 to when a background of 10 μM CRM1 is present (magenta arrow in Fig. 3.7F), as a function of Imp5 and CRM1 K_D values. The bounded regions (black) indicate the K_D values which are consistent with SPR measurements and are within one standard deviation of experimentally measured occupancy shifts. Dashed contour lines indicate the K_D values that result in the average experimentally measured shift (white), and the K_D values that result in one deviation from these relative occupancy values (grey). Note: The color scale of each heatmap is different.

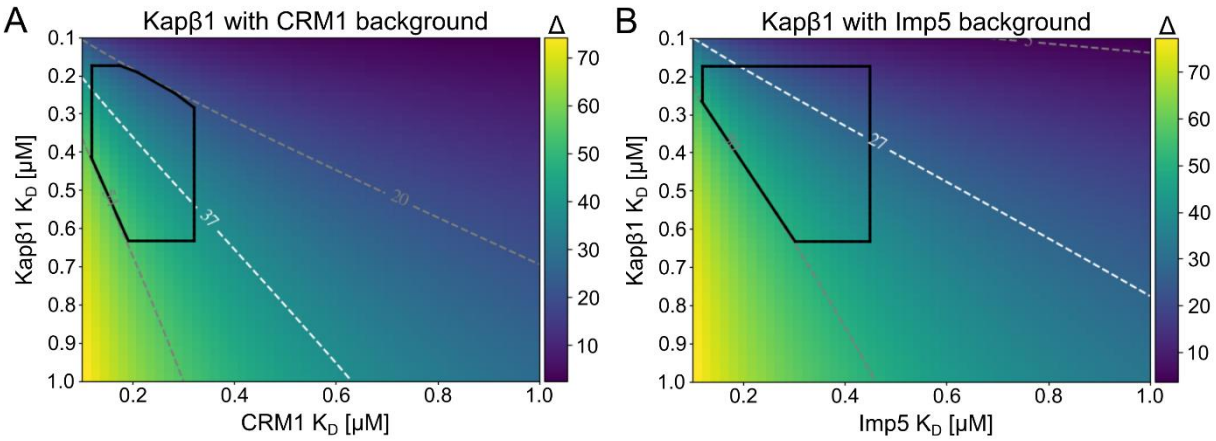

Figure 3.9 Reduction of Kapβ1 occupancy in response to CRM1 and Imp5 binding

(A) Theoretically predicted shift in the occupancy of Kapβ1 calculated between its standalone value at 10 μM Kapβ1 and in the presence of 10 μM CRM1 background (Fig. 3.7B, green trace), as a function of Kapβ1 and CRM1 K_D values. (B) Same as (A), except a background of 10 μM Imp5 is assumed (Fig. 3.7D, green trace). The marked region (black) indicates the K_D values, which are consistent with SPR measurements and are within one standard deviation of experimentally measured occupancy shifts. Dashed contour lines indicate the pairs of K_D values that result in the average experimentally measured shift (white), and the K_D pairs that correspond to the one standard deviation from the values of the average relative occupancy (grey). Note: The color scale in each heatmap is different.

3.8 Conclusions

So far biophysical characterization of Kapβs was mainly focused on Kapβ1. Using various methods (e.g., bead/solution binding assays, SPR) (Kapinos et al., 2017; Kapinos et al., 2014; Pyhtila and Rexach, 2003; Tetenbaum-Novatt et al., 2012), it has been shown that Kapβ1-FG Nup binding falls within the low range of the $K_{D,SPR}$ values, indicating strong binding (Fig. 3.2). This is also the case for Imp5 and CRM1 interactions with the FG Nups measured here. Therefore, the binding affinity, with the notable exception of weaker CRM1-cNup62 interactions, does not differentiate between Kapβs sufficiently to explain or predict their prevalence within the FG Nups. Nevertheless, the differences in the dissociation rates (k_{off}) (Fig. 3.3B) indicate that Imp5 is more inclined to leave the FG Nup layer. We hypothesize that this provides an opportunity for other Kapβs to bind and replace faster departing molecules. Such differences in Kapβ binding properties likely arise from subtle variations in FG-repeat binding pockets, molecular flexibility and shape. Interestingly, the binding capacity of a given FG Nup varies depending on the interacting Kapβ, which can also be interpreted as the ability of the particular Kapβ to penetrate into the FG Nup layer (Fig. 3.4). Overall, amongst the tested Kapβs, Kapβ1 has the highest permeation capability, and as such might accumulate within FG Nups most efficiently.

Though highly sensitive, SPR does not allow for differentiating between Kapβs upon their simultaneously binding to the FG Nups. That is because of Kapβs' comparable molecular weights and similar kinetic binding rates. Therefore, we adapted a well-established permeabilized cell assay to study the binding of Kapβs to the NPCs and their competition *ex vivo*. Obtained binding affinity values closely correspond to the *in vitro* measurements and confirm the negligible impact of the geometrical constraints (i.e., planar vs. cylindrical arrangement of the FG Nups) (Kapinos et al., 2014; Malekian et al., 2018) and post-translational modifications of the FG Nups (Davis and Blobel, 1987; Yoo and Mitchison, 2021). The only discrepancy concerning Kapβ1 binding affinity arises from the multivalent nature of Kapβ-FG Nup interactions that explain the existence of the long-living fraction of Kapβ1 in the NPCs (Fig. 3.3 and Fig 3.6) (Kapinos et al., 2017; Kapinos et al., 2014). Indeed, this assay is limited by the inherent persistence of residual Kapβs against Ran mix treatment (see Chapter 2.5).

Despite comparable binding affinity values acquired for all tested Kapβs, Kapβ1 prevails over Imp5 at the NPCs *ex vivo.* On the contrary, simultaneous binding of Kapβ1 and CRM1 or CRM1 and Imp5 is observed. We postulate that the differences in Kapβs ability to permeate into certain FG Nups (Fig. 3.4) may significantly contribute to this outcome. Furthermore, there is a possibility that the co-existence of different Kapβs at NPCs and their competition correlates with their preferential binding to distinct combinations of FG Nups (Strawn et al., 2004; Terry and Wente, 2007). Nevertheless, we were able to resolve this conundrum by using the mean-field model which indicates that Kapβs occupancy at the NPC is balanced by their molecular size, abundance, and binding affinity to the FG Nups. These findings highlight the fine molecular details that dictate Kapβ competition *in vivo*.

3.9 Materials and Methods

3.9.1 Protein expression and purification

Cysteine-tagged FG Nups of human Nup62 (1-240 aa; cNup62), Nup98 (1-498 aa; cNup98), Nup153 (874-1475 aa; cNup153), and Nup214 (1809-2090 aa; cNup214), were expressed and purified as described previously (Kapinos et al., 2014). Briefly, additional cysteine residues were added (3xCys at the N-termini of cNup98 and cNup153, 1xCys at the N-terminus of cNup214, 1xCys at the C-terminus of cNup62) to enable covalent binding to gold sensor surfaces during SPR. The constructs were cloned into pPEP-TEV (cNup62, cNup98 and cNup153) or PETM11 (cNup214) vectors. Recombinant N-terminal His-tagged FG Nups were expressed in *E.coli* BL21

(DE3) upon the addition of 0.5 mM IPTG. All four FG Nups were purified under denaturing conditions (8 M urea, 100 mM NaH_2PO_4, 10 mM Tris Base, pH 8.0) using a HisTrap HP column (GE Healthcare), followed by His-tag removal with TEV protease and a second run on the HisTrap HP column. The purity of the collected fractions was verified using gel electrophoresis (12% PAGE at 0.1% SDS). Selected fractions were combined, concentrated, and frozen until further use.

All karyopherins were expressed in E. coli BL21 (DE3) upon induction with 0.5 mM IPTG (Kapβ1 and Imp5) or 0.1 mM IPTG (CRM1) at 20-22°C. Kapβ1 (1-876 aa) was purified with a N-terminal His-tag (10 mM Tris pH 7.5, 100 mM NaCl, 1 mM DTT, 10 mM imidazole; eluted with 500 mM imidazole) from pETM-11 vector followed by gel filtration (Superdex 200, GE Healthcare). Imp5 (1-1097 aa) (OriGene, SC118726) was purified following the same procedure, except a pPEP-TEV expression vector was used. Full-length codon-optimized CRM1 (1-1071 aa) was a kind gift from A. Dickmanns (University of Göttingen, Göttingen, Germany). CRM1 with a C-terminal His-tag was purified from the pET21a vector as described before (Shaikhqasem et al., 2020). Briefly, cleared protein lysate was first applied onto a HisTrap HP column (GE Healthcare) (50 mM HEPES pH 7.5, 500 mM NaCl, 10 mM imidazole; 2 mM $MgCl_2$, 10% glycerol, 4 mM β-mercaptoethanol) and eluted by a step-wise increase of imidazole concentration up to 500 mM. After that, the collected fractions were desalted *via* dialysis (50 mM HEPES pH 7.5, 50 mM NaCl, 2 mM $MgCl_2$, 5% glycerol, 4 mM β-mercaptoethanol) with the remaining impurities being removed by anion exchange chromatography (HiTrap Q HP Column, GE Healthcare). Protein elution was performed in a 0-70% gradient of low (50 mM HEPES pH 7.8, 50 mM NaCl, 2 mM $MgCl_2$, 6 mM β-mercaptoethanol) to high salt buffer (50 mM HEPES pH 7.8, 400 mM NaCl, 2 mM $MgCl_2$, 6 mM β-mercaptoethanol). Purified Kapβ1, Imp5, and CRM1 were analyzed by gel electrophoresis (12% PAGE at 0.1% SDS). Selected fractions were then pooled together, concentrated, and stored at -80 °C until needed. The concentration of the recombinant proteins was determined by absorption measurements at 280 nm ($A^{0.1\%}_{Kap\beta1}$ = 0.810, $A^{0.1\%}_{Imp5}$ = 0.918, $A^{0.1\%}_{CRM1}$ = 0.940).

3.9.2 Fluorescent labeling

Recombinant Kapβ1 was labeled with Alexa Fluor 488 C5 maleimide dye (A10254, Invitrogen), CRM1 with Alexa Fluor 647 N-hydroxysuccinimide ester (A20006, Invitrogen) dye, and Imp5 with either Alexa Fluor 488 C5 maleimide or Alexa Fluor 647 C2 maleimide (A20347, Invitrogen)

dyes depending on its final usage. For Kapβ1 and Imp5, dyes were added in 10-fold excess and the reaction was incubated overnight at 4°C, while a 2-fold excess of the dye and 2 h incubation at room temperature was optimal for CRM1 labeling. CENTRI-SEP spin columns (Princeton Separations) were used to remove the free dye. Protein concentration and labeling efficiency were calculated following Nanodrop UV-Vis spectrometry to measure the respective dye and protein absorptions. If needed, labeled proteins were concentrated further using Pierce Protein Concentrators PES of 10 kDa MWCO. Labeled Kapβs were snap-frozen and stored at -80 °C until further usage.

3.9.3 Dynamic Light Scattering (DLS)

The hydrodynamic diameters of Kapβ1, CRM1, and Imp5 were measured at 0.1 mg/mL in PBS using the Zetasizer Nano instrument (Malvern). This gave the following radii values: $s_{Kap\beta1}$ = 5.6 ± 1 nm (n= 3), s_{CRM1}= 6.3 ± 1.3 nm (n= 5), and s_{Imp5}= 7.1 ± 0.7 nm (n= 3). The values of n = 1.45 and n = 1.330 were used as the refractive indices for proteins and dispersant (i.e., water; T = 25.0°C, viscosity = 0.8882 cP), respectively.

3.9.4 Reagents

BSA (Sigma–Aldrich) was dissolved in filtered and degassed PBS (Gibco™ by Life Technologies) to a final concentration of 1% (wt/vol). $C_{17}H_{36}O_4S$ (hydroxyl-terminated tri[ethylene glycol] undecane thiol, HS-[CH2]-[OCH2CH2]3-OH, abbreviated as PUT; Sigma Aldrich Cat. No. 673110) was dissolved in ethanol to obtain 100 mM stock, which was then diluted in ethanol to 10 mM concentration and further in PBS to 1 mM prior to the experimentation.

3.9.5 SPR Sensor Chip Preparation

SPR gold sensor chips (SIA Kit Au, GE Healthcare) were stored under a vacuum. Before usage, chips were sequentially sonicated in acetone, 2-propanol, and high-purity ethanol for 15 min each followed by immediate drying in a nitrogen gas stream. Sensors were then UV ozone-cleaned for 40 min (Model 42A-220; Jelight Company Inc.) and sonicated again for 15 min in ethanol. The gold sensors were mounted on the sample holder immediately after drying under a nitrogen gas stream and kept protected from contamination.

3.9.6 SPR measurements

The SPR measurements were performed at 25°C in a four-flow cell Biacore T200 (GE Healthcare) instrument as described before (Kapinos et al., 2014; Schoch et al., 2012).

Briefly, PUT and cysteine-modified FG Nups were immobilized on a gold sensor surface using thiol chemistry. Flow chambers 1 and 2 were used as a reference, while chambers 3 and 4 were used for the binding measurement. Measurements were performed in filtered and degassed PBS buffer, pH 7.2 (GIBCO, Life Technologies). Before the experimentation, all proteins were dialyzed against PBS and diluted to the desired concentrations. The resulting solutions were centrifuged for 15 min at 15,000 g to remove particles and bubbles.

3.9.7 SPR protocol

Frist, FG Nups were immobilized in the measurement channels (2µl/min for 40min) and reference channels were passivated with PUT3 (2 µl/min for 30 min). Afterward, all flow channels were incubated with PUT3 (2 min, 2 µl/min) to minimize the effect of the analyte's unspecific binding to the sensor's surface. The binding of a Kapβ to FG Nups was monitored by titration with increasing concentrations of Kapβ, specifically 0.00078, 0.016, 0.031, 0.625, 0,125, 0.25,0.5, 1, 2, 4, 8, and stock solution >10 µM. Due to the low purification efficiency of CRM1 and its low stability, the maximum CRM1 concertation used for SPR measurements was 8 µM. Each association and dissociation phase was recorded for 10 min and 7 min, respectively, at a 10 µl/min flow rate. At the end of every Kapβ binding step, three consecutive BSA injections (10µl/min, 30 sec) were performed to measure the FG Nup layer height change. In the last cycle, all Kapβ molecules were removed from the surface by treatment with 0.2 M NaOH solution (10µl/min for 10 min) followed by a 30 min buffer wash. This regeneration step ensured that all Kapβs could bind reversibly to the FG Nups.

3.9.8 SPR analysis

3.9.8.1 Grafting distance calculation

Grafting distance for each FG Nup was calculated according to the following formula:

$$g[nm] = \sqrt{\frac{10^{12} \cdot 1300 \cdot 10^{3} \cdot MW}{N_A \cdot \Delta RU}},$$

where:

g – grafting distance [nm]

MW- molecular weight of the FG Nup [Da]

N_A- Avogadro number ($6.02 \bullet 10^{23}$ molecules/mol)

ΔRU- a difference in the SPR response due to the FG Nup binding to the sensor surface.

Number 1300 RU comes from the SPR response to binding 1 ng/mm^2 of protein.

3.9.8.2 Kapβs surface density and number of layers within FG Nups

First, the Kapβs grafting distance ($g_{Kap\beta}$) was calculated by applying the same formula as for FG Nups (See Chapter 3.9.8.1) using molecular weights of 97, 126, and 130 kDa for Kapβ1, CRM1, and Imp5, respectively. Subsequently, Kapβ surface density ($\rho_{Kap\beta}$) in Da/nm^2 was determined using the following formula:

$$\rho_{Kap} = \frac{MW}{(g_{Kap})^2}$$

Next Kapβs were approximated as ellipsoids and the semi-minor axis was calculated based on the SAXS data (parameters summarized in Table 3.1) according to:

$$R_g = [a^2 + b^2 + c^2]/5,$$

where:

R_g – radius of gyration (hydrodynamic radius measured by DLS)

a, b, c - two semi-minor axes and the semi-major axis of an ellipsoid, respectively (Feigin & Svergun, 1987). Using SAXS and calculated parameters, volumes of the corresponding ellipsoids were estimated, followed by the calculation of the diameters of the spheres with equivalent volumes (Table 3.1). This allowed us to estimate the number of monolayers Kapβs form within each FG Nups layer:

$$No.\ Kap\ layers = \frac{{d_{Kap}}^2}{{g_{Kap}}^2}$$

Table 3.1 Summary of the literature and experimental parameters obtained from the DLS measurements of Kapβ1, CRM1, and Imp5 used to calculate the spheres with equivalent molecular volumes.

Parameter	*Kapβ1*	*CRM1*	*Imp5*
a,b [nm]	4.5	4.6	3.8
c [nm]	6	5.5	6.8
R_g [nm]	3.9	3.8	3.88
Volume of ellipsoid [nm^3]	503	483	413
Sphere diameter ($d_{Kap\beta}$) [nm]	4.9	4.87	4.6
Reference	(Forwood et al., 2010)	(Dölker et al., 2013)	(Swale et al., 2016)

3.9.8.3 FG Nup layer height

After each immobilization step of the increasing concertation of the NTR, a triple BSA injection was recorded. The SPR response obtained after each of those injections allows for the detection

of conformational changes that FG Nups undergo upon NTRs binding and in the result for the calculation of the FG Nup layer height as presented below:

$$d_{2,j} = \frac{l_d}{2} ln\left(\frac{R_{1,j} \cdot m_2}{R_{2,j} \cdot m_1}\right) + d_1$$

where:

$d_{2,j}$ - FG Nup layer thickness in flow cell 2 at the j-th NTR injection

d_1 - thickness of the reference layer in flow cell 1 (for PUT d_1 = 2 nm)

$R_{1,j}$ or $R_{2,j}$ – measured SPR responses to the BSA injection in the flow cells 1 (reference) or 2 (sample) at each j-step

l_d - decay length of the evanescent field (350 nm)

m_1/m_2 - calibration constants. If the sensor surface is the same in channels 1 and 2, $m_1/m_2 = 1$

3.9.8.4 Determining apparent equilibrium dissociation constants

Steady-state equilibrium response (R_{eq}) was extracted from the sensograms at each NTR concentration used in the experiments. By plotting R_{eq} value versus NTR concentration (C_A) and fitting data points to a Langmuir adsorption isotherm given by the following equation, maximum surface binding capacity ($R_{max,i}$) and equilibrium binding constant ($K_{D,i}$) can be obtained.

$$R_{eq}(C_A) = \sum_{i=1}^{n} \frac{R_{max,i} \cdot C_A}{K_{D,i} + C_A},$$

It is important to point out that for NTR typically n=1,2.

3.9.8.5 Kinetic analysis of multivalent interactions

A detailed description of the Kapβs kinetic binding analysis can be found in Kapinos et al., 2014, here only a shorter description is provided. The understanding of the multivalent nature of Kapβs•FG Nups binding can be facilitated by applying the idea of surface heterogeneity (Svitel et al., 2003; Svitel et al., 2007). This approach allows to calculate two-dimensional representation of kinetic rates (k_{on} or k_{off}) versus binding constants (K_D) from the SPR experiments. As the result, the fractional abundance of ligand binding sites or analyte molecules possessing different binding properties can be revealed at a much higher detail level than regular SPR kinetic analysis.

The kinetic maps were created by modeling the binding sites as a discrete set of k_{on} and k_{off} pairs ($P_i(k_{on,i}, k_{off,i})$) of total N= $N_{kon,i}$ x $N_{koff,i}$, in this case 36 x 36, binding states. The total measured signal of analyte binding is given by the following equation:

$$s_{total}(c,t) = \sum_{i=1}^{N} P_i(k_{off,i}, k_{on,i}) s_i(k_{off,i}, k_{on,i}, c, t) \Delta k_{off} \Delta\, k_{on}$$

where c is analyte concentration, t is time and ($P_i(k_{on,i}, k_{off,i})$) stands for the fractional abundance of each binding state. The calculated values can be then represented on a k_{on} versus K_D or k_{off} versus K_D grid, where the underlying binding states distribution is visualized by a contour plot. To obtain such a map, for each $k_{on,i}$ and $k_{off,i}$ pair a full sensogram $s_i(k_{on,i}, k_{off,i}, c, t)$ is created. For this step, pseudo-first-order reaction kinetics was used to model Kapβs binding to the FG Nups layer.

$$L + A_s \underset{k_{off,i}}{\overset{k_{on,i}}{\rightleftarrows}} LA_1 + A_s \underset{k_{off,i}}{\overset{k_{on,i}}{\rightleftarrows}} LA_2 + A_s \underset{k_{off,i}}{\overset{k_{on,i}}{\rightleftarrows}} \dots \underset{k_{off,i}}{\overset{k_{on,i}}{\rightleftarrows}} LA_n$$

Where L stands for the free binding sites, As is the analyte concentration in solution and LA_n are already occupied binding sites at each (n) assumed layer. Once the differential equations resulting from this model are numerically solved, the final sensogram $s_i(k_{on,i}, k_{off,i}, c, t)$ is constructed by linearly superimposing the concentrations LA_1+ 2 x LA_2+ 3 x LA_3. The weight ($P_i(k_{on,i}, k_{off,i})$) of each discrete binding site is then calculated by comparison of the calculated sensogram with the experimental data. Finally, the regularization step was applied to obtain a parsimonious distribution of ($P_i(k_{on,i}, k_{off,i})$) and a contour plot of the interaction map was created.

3.9.9 Kapβ binding in permeabilized cells

HeLa cells were plated on glass coverslips (#1.5) 1 day before experimentation. Cells were washed twice with PBS (Sigma Aldrich) and permeabilized for 5 min with 40 µg/ml digitonin as reported previously (Adam et al., 1990). After three 5 min washes with PBS, cells were incubated with Ran mix (2 mM GTP, 0.1 mM ATP, 4 mM creatine phosphate, 20 U/ml creatine kinase, 5 µM RanGDP, 4 µM NTF2, and 1 mM DTT) for 1h at room temperature to deplete endogenous Kapβs. Following another triple washing step in PBS of 5 min each, cells were incubated for 1 h in varying concentrations of fluorescently-labeled Kapβ1, CRM1, and Imp5 or their combinations to study their repopulation at the NPCs. After a triple-washing step in PBS of 5 min each, cells were fixed with 4% formalin for 15 min and stained with DAPI. Then, cells underwent a final triple washing step in PBS before being mounted in the Vectashield medium mixed with fluorescent calibration beads (InSpeck Green Fluorescent beads, ThermoFisher Scientific; MESF Alexa Fluor-647 beads, Bang Laboratories).

3.9.10 Confocal microscopy, imaging, and analysis

Fluorescence images of fixed samples were obtained at room temperature using an LSM880 inverted confocal microscope and ZEN 2.3 software. The system was equipped with an oil-immersed 63×/1.4 NA PLAN Apochromat objective, a widefield camera, and an Airyscan detector (Zeiss). The NE fluorescence intensity from the permeabilized cells assay was quantified using custom Fiji macros. First, images were smoothed (median filter of 10-pixel radius) and automatically segmented based on the DAPI signal using the Otsu method. The region corresponding to NE (NE ROI) was defined by the combined enlarging and shrinking of the originally segmented DAPI signal. In some cases, NE ROIs had to be manually adjusted by translation and/or removal of nonfluorescent subsegments due to small but not negligible chromatic shift and discontinuities in NE. Because of a broad range of Kapβ concentrations used in the permeabilized cell assays, laser power had to be adjusted for each Kapβ titration condition. To correct for these variations, Green InSpeck beads (ThermoFisher Scientific) and MESF Alexa Fluor-647 beads (Bang Laboratories) were premixed with the samples and imaged with increasing laser power settings. Changes in bead fluorescence were then used to obtain calibration curves (Fig. 3.10), which allowed for the normalization of the Kapβ fluorescent signal at the NE.

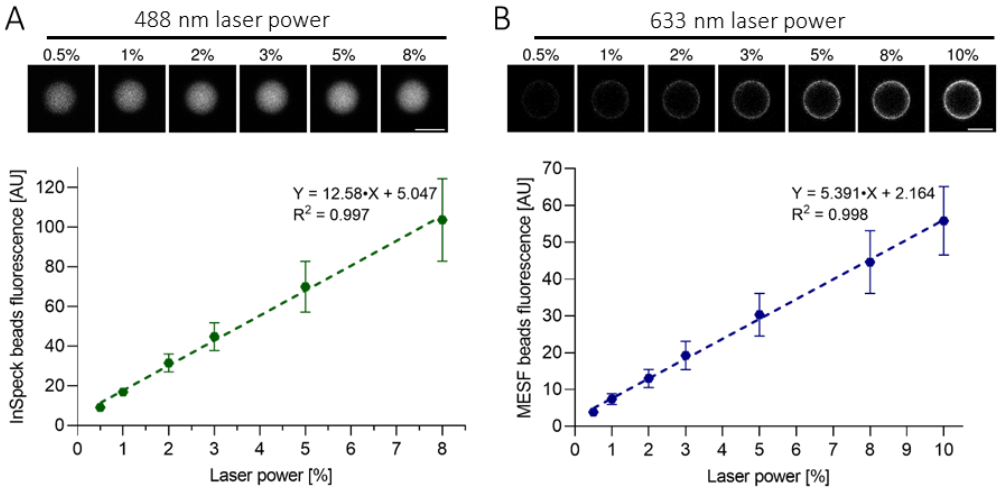

Figure 3.10 Fluorescence calibration curves.

Examples of the fluorescence images and calibration curves obtained by imaging Green InSpeck (A) or MESF (B) beads at different power levels of 488 nm and 633 nm lasers, respectively. Mean fluorescent values and standard deviations of multiple beads measurements (n>10) from a given dataset were fitted with simple linear regression. The fitting parameters and the coefficient of determination (R^2) are displayed on the plots. As the laser power might fluctuate over an extended time, calibration curves were prepared separately for each experimental replicate. Scale bar: 5 µm.

3.9.11 Mean-field model of Kapβ accumulation within a pore

Here, we present a minimal model of Kapβ accumulation in the FG Nup assembly of the NPC, based on the models developed by Opferman et al., 2013 and Vovk et al., 2016. As explained below, these minimal models take into account only the most salient features of the system, such as the average interaction of the Kapβs with the FG Nup milieu and competition for space and binding sites within the NPC, subsuming a multitude of molecular interactions into a small number of coarse-grained parameters. These minimal models have been successful in explaining the spatial morphology and specificity of Kapβ accumulation in FG Nup assemblies in various geometries and can be extended to take into account more detailed microscopic variables such as the sequence heterogeneity and the discrete nature of the binding sites on the Kapβs.

To gain insights into the experimental results (Fig. 3.7), for each pairwise competition experiment, we represent the two different Kapβs, with respective volumes v_1 and v_2 where $v_1 > v_2$. The interactions of a Kapβ of type i with the FG Nup milieu inside the NPC are represented by a phenomenological free energy gain ϵ_i within the pore (which is affected by the multivalent binding between the Kapβ and FG Nups, the internal cohesiveness, and the density of FG Nups in the pore). This phenomenological parameter is related to the equilibrium dissociation constant K_D of Kapβs interacting with the FG Nups, and can be estimated from *in vitro* SPR experiments (Fig. 3.2). Once within the pore, the Kapβs compete for space inside it, represented *via* excluded volume interactions.

3.9.11.1 Accumulation of a single type of particle:

Under these assumptions, the grand canonical free energy per unit volume of a system with a single type of Kapβ inside the pore (coupled to a dilute solution outside), is, for Kapβ type i (Opferman et al., 2013; Vovk et al., 2016):

$$\mathrm{F} = \frac{1}{v_i}\phi_i \ln\phi_i + \frac{1}{v_i}(1-\phi_i)ln(1-\phi_i) + \frac{1}{v_i}\epsilon_i\phi_i - \frac{1}{v_i}\mu_i\phi_i,$$

where ϕ_i is the volume fraction of the Kapβs inside the pore given by $\frac{\mathrm{N_i}v_i}{V}$ where N_i is the number of type i Kapβs inside the pore, V is the volume of the pore, and $\mu_i = ln(c_i v_i)$ is the chemical potential of the particle solution outside of concentration c_i. The first term represents the translational entropy of the Kapβs, the second term represents the entropic cost of

competition for space, the third term represents the interaction of Kapβs with the pore, and the last term is the coupling to the solution outside the pore.

The equilibrium solution is obtained by minimizing the free energy over the particle concentration within the pore by setting $\frac{dF}{d\phi_i} = 0$, which gives: $\phi_i^S = \frac{e^{\mu_i - \epsilon_i}}{1+e^{\mu_i-\epsilon_i}} = \frac{c_i}{c_i+K_{D_i}}$, where the last equality arises from the definition of μ_i, and defines the effective dissociation constant $K_{D_i} \equiv \frac{1}{v_i} e^{\epsilon_i}$. The superscript s indicates that it is a solution for single-particle species.

3.9.11.2 Accumulation of two types of particles:

When we combine two different types of Kapβs within the same pore, the grand canonical energy per volume (measured in units of v_2) for this mixture is given by (Opferman et al., 2013; Vovk et al., 2016):

$$F = \frac{1}{v_1}[\phi_1 \, ln\, \phi_1 + v\phi_2 \, ln\, \phi_2 + (1-v)(1-\phi_1)\, ln(1-\phi_1) + v(1-\phi_1-\phi_2)\, ln(1-\phi_1-\phi_2)] + \frac{1}{v_1}(\epsilon_1 - \mu_1)\phi_1 + \frac{v}{v_1}(\epsilon_2 - \mu_2)\phi_2,$$

where $v = \frac{v_1}{v_2}$. As before, the first two terms represent the translational entropy of the particles, the next two terms represent the entopic costs of competition for space, and the last two terms describe the interaction of the particles with the pore and coupling to the external solution. The equilibrium state is found by the minimization $\frac{\partial F}{\partial \phi_1} = 0$ and $\frac{\partial F}{\partial \phi_2} = 0$, giving two equations that can be solved numerically:

$$\frac{\phi_1^M (1-\phi_1^M)^{v-1}}{\left[(1-\phi_1^M)\left(1-\frac{c_2}{c_2+K_{D_2}}\right)\right]} = \frac{c_1}{K_{D_1}}$$

$$\phi_2^M = (1-\phi_1^M)\frac{c_2}{c_2+K_{D_2}}.$$

The superscript M indicates that this is a solution when multiple particle types are present.

The experimentally measured quantity Δ (Fig. 3.7) is given by $\phi_1^S - \phi_1^M$ for CRM1 and Imp5 on a background of Kapβ1 (where Kapβ1 is the smaller Kapβ), respectively and $\phi_2^S - \phi_2^M$ for Imp5 on a background of CRM1 (where CRM1 is the larger Kapβ), computed at the endpoint of the experimental concentration range where both $c_1$and c_2 are 10 μM. The volume of each

different Kapβ was calculated from its known crystal structure (PDB: Kapβ1 - 3nd2, CRM1 - 4fgv, and Imp5 - 3w3t). The results are shown in Fig. 3.8 and 3.9.

To test the robustness of the model predictions concerning the choice of the model and its assumptions, we investigated several other models of the same family (not shown). We found that our results are robust with respect to the model choice, as long as a model accounts for the same salient physical variables – attractive interaction of the Kapβs with the FG Nup milieu inside the pore and the competition for space. These models provide a foundation for more detailed descriptions that will include spatial inhomogeneity of the FG Nup assembly in the pore and specifics of the binding sites distributions on the FG Nups and the Kapβs.

3.10 References

Adam, S.A., Marr, R.S., and Gerace, L. (1990). Nuclear-protein import in permeabilized mammalian-cells requires soluble cytoplasmic factors J Cell Biol *111*, 807-816.

Barbato, S., Kapinos, L.E., Rencurel, C., and Lim, R.Y.H. (2020). Karyopherin enrichment at the nuclear pore complex attenuates Ran permeability. J Cell Sci *133*.

Davis, L.I., and Blobel, G. (1987). Nuclear pore complex contains a family of glycoproteins that includes p62: glycosylation through a previously unidentified cellular pathway. *84*, 7552-7556.

Dölker, N., Blanchet, Clement E., Voß, B., Haselbach, D., Kappel, C., Monecke, T., Svergun, Dmitri I., Stark, H., Ficner, R., Zachariae, U.*, et al.* (2013). Structural Determinants and Mechanism of Mammalian CRM1 Allostery. Structure (London, England : 1993) *21*, 1350-1360.

Feigin, L.A., and Svergun, D.I. (1987). Structure Analysis by Small-Angle X-Ray and Neutron Scattering. Springer US.

Forwood, J.K., Lange, A., Zachariae, U., Marfori, M., Preast, C., Grubmuller, H., Stewart, M., Corbett, A.H., and Kobe, B. (2010). Quantitative structural analysis of importin-beta flexibility: paradigm for solenoid protein structures. Structure (London, England : 1993) *18*, 1171-1183.

Homola, J. (2008). Surface plasmon resonance sensors for detection of chemical and biological species. Chem Rev *108*, 462-493.

Kapinos, L.E., Huang, B., Rencurel, C., and Lim, R.Y.H. (2017). Karyopherins regulate nuclear pore complex barrier and transport function. J Cell Biol *216*, 3609-3624.

Kapinos, L.E., Schoch, R.L., Wagner, R.S., Schleicher, K.D., and Lim, R.Y. (2014). Karyopherin-centric control of nuclear pores based on molecular occupancy and kinetic analysis of multivalent binding with FG nucleoporins. Biophys J *106*, 1751-1762.

Malekian, B., Schoch, R.L., Robson, T., del Castillo, G.F.D., Xiong, K.L., Emilsson, G., Kapinos, L.E., Lim, R.Y.H., and Dahlin, A. (2018). Detecting Selective Protein Binding Inside Plasmonic Nanopores: Toward a Mimic of the Nuclear Pore Complex. Frontiers in Chemistry *6*.

Opferman, M.G., Coalson, R.D., Jasnow, D., and Zilman, A. (2013). Morphology of Polymer Brushes Infiltrated by Attractive Nanoinclusions of Various Sizes. Langmuir *29*, 8584-8591.

Port, S.A., Monecke, T., Dickmanns, A., Spillner, C., Hofele, R., Urlaub, H., Ficner, R., and Kehlenbach, R.H. (2015). Structural and Functional Characterization of CRM1-Nup214 Interactions Reveals Multiple FG-Binding Sites Involved in Nuclear Export. Cell Rep *13*, 690-702.

Pulupa, J., Prior, H., Johnson, D.S., and Simon, S.M. (2020). Conformation of the nuclear pore in living cells is modulated by transport state. Elife *9*.

Pyhtila, B., and Rexach, M. (2003). A gradient of affinity for the karyopherin Kap95p along the yeast nuclear pore complex. J Biol Chem *278*, 42699-42709.

Schoch, R.L., Kapinos, L.E., and Lim, R.Y. (2012). Nuclear transport receptor binding avidity triggers a self-healing collapse transition in FG-nucleoporin molecular brushes. Proceedings of the National Academy of Sciences of the United States of America *109*, 16911-16916.

Schoch, R.L., and Lim, R.Y. (2013). Non-interacting molecules as innate structural probes in surface plasmon resonance. Langmuir *29*, 4068-4076.

Shaikhqasem, A., Dickmanns, A., Neumann, P., and Ficner, R. (2020). Characterization of Inhibition Reveals Distinctive Properties for Human and Saccharomyces cerevisiae CRM1. J Med Chem *63*, 7545-7558.

Strawn, L.A., Shen, T.X., Shulga, N., Goldfarb, D.S., and Wente, S.R. (2004). Minimal nuclear pore complexes define FG repeat domains essential for transport. Nat Cell Biol *6*, 197-206.

Svitel, J., Balbo, A., Mariuzza, R.A., Gonzales, N.R., and Schuck, P. (2003). Combined affinity and rate constant distributions of ligand populations from experimental surface binding kinetics and equilibria. Biophys J *84*, 4062-4077.

Svitel, J., Boukari, H., Van Ryk, D., Willson, R.C., and Schuck, P. (2007). Probing the functional heterogeneity of surface binding sites by analysis of experimental binding traces and the effect of mass transport limitation. Biophys J *92*, 1742-1758.

Swale, C., Monod, A., Tengo, L., Labaronne, A., Garzoni, F., Bourhis, J.M., Cusack, S., Schoehn, G., Berger, I., Ruigrok, R.W.*, et al.* (2016). Structural characterization of recombinant IAV polymerase reveals a stable complex between viral PA-PB1 heterodimer and host RanBP5. Sci Rep *6*, 24727.

Terry, L.J., and Wente, S.R. (2007). Nuclear mRNA export requires specific FG nucleoporins for translocation through the nuclear pore complex. J Cell Biol *178*, 1121-1132.

Tetenbaum-Novatt, J., Hough, L.E., Mironska, R., McKenney, A.S., and Rout, M.P. (2012). Nucleocytoplasmic Transport: A Role for Nonspecific Competition in Karyopherin-Nucleoporin Interactions. *11*, 31-46.

Voss, N.R., and Gerstein, M. (2010). 3V: cavity, channel and cleft volume calculator and extractor. Nucleic Acids Res *38*, W555-W562.

Vovk, A., Gu, C., Opferman, M.G., Kapinos, L.E., Lim, R.Y.H., Coalson, R.D., Jasnow, D., and Zilman, A. (2016). Simple biophysics underpins collective conformations of the intrinsically disordered proteins of the Nuclear Pore Complex. eLife *5*.

Wagner, R.S., Kapinos, L.E., Marshall, N.J., Stewart, M., and Lim, R.Y.H. (2015). Promiscuous binding of Karyopherinbeta1 modulates FG nucleoporin barrier function and expedites NTF2 transport kinetics. Biophys J *108*, 918-927.

Yoo, T.Y., and Mitchison, T.J. (2021). O-GlcNAc modification of nuclear pore complexes accelerates bidirectional transport. J Cell Biol *220*.

Chapter 4

Kapβs are integral constituents of the NPC *in vivo*

Adapted from

Karyopherin enrichment and compensation fortifies the nuclear pore complex against nucleocytoplasmic leakage

Joanna Kalita, Larisa E. Kapinos, Tiantian Zheng, Chantal Rencurel, Anton Zilman and Roderick Y. H. Lim

Published in Journal of Cell Biology, 221(3), jcb.202108107 (2022)

4.1 Kap-centric control in living cells

The role of Kapβs as transport receptors is evident, however, according to the Kap-centric control model (Chapter 2.2) (Kapinos et al., 2014; Lim et al., 2015; Lowe et al., 2015; Wagner et al., 2015; Zilman, 2018), new non-transport roles of Kapβs emerge. In fact, recent findings indicate that Kapβs occupancy at the NPC may reinforce the permeability barrier and even affect NPC structure (Barbato et al., 2020; Kapinos et al., 2017; Pulupa et al., 2020).

The Kap-centric model rests on a basis of FG Nup saturation with Kapβs. Yet, as discussed in Chapter 2, not all Kapβs show the same steady-state enrichment at the NPC (Kalita et al., 2021). The strong nuclear rim staining observed for Kapβ1 and CRM1 may set them apart from other importins and exportins *in vivo.* This is particularly interesting as all Kapβs exhibit high structural similarity (Chapter 1.3) (Christie et al., 2016; Conti et al., 2006) and presumably all bind to the FG Nups with high affinities, comparable to already characterized Kapβs (i.e., Kapβ1, CRM1, and Imp5) (Chapter 3.2) (Ben-Efraim and Gerace, 2001; Kapinos et al., 2017; Kapinos et al., 2014) and Kapβ yeast homologs (i.e., Kap95, Kap121, Kap123) (Pyhtila and Rexach, 2003; Tan et al., 2018; Tetenbaum-Novatt et al., 2012).

So far, studies that investigated the effect of Kapβs on the permeability barrier were performed *in vitro* (Kapinos et al., 2014; Malekian et al., 2018; Schoch et al., 2012) or *ex vivo* (Kapinos et al., 2017; Lowe et al., 2015) and focused predominantly on Kapβ1. These experiments lack the competition and compensation effects that could arise from the presence of the other Kapβs and in this aspect do not resemble the situation *in vivo*. Therefore, all Kapβs may contribute to the maintenance of the NPC permeability barrier and compensate for the loss of certain Kapβs, in particular as their cumulative concentration in a cell reaches a micromolar value (Fig 2.5) (Kirli et al., 2015). Nevertheless, the question about the Kapβs contribution to the NPC permeability barrier *in vivo* remains. In this chapter, we test the validity of the Kap-centric model and the interchangeability of Kapβs as permeability barrier contributors.

4.2 Evidence of Kapβ compensation at the NPC

Competition experiments in permeabilized cells indicate that Kapβs can indeed coexist in the NPCs and that the level of their accumulation depends on the nature of the given Kapβ and their competitor (Chapter 3.6). These observations led us to question if one Kapβ could compensate for another Kapβ following a reduction of the latter at the NPC. To address this

problem, we used three different silencing conditions (denoted as Kapβ1 siRNA1 55 pmol, Kapβ1 siRNA2 55pmol, and Kapβ1 siRNA2 110 pmol) to deplete endoKapβ1 and two additional conditions (denoted as CRM1 siRNA2 55pmol and CRM1 siRNA2 110 pmol) to reduce endoCRM1 in MDCK cells (Fig. 4.1A). Verification of Kapβ silencing efficiency *via* Western Blotting (WB) revealed that over 80% of endoKapβ1 was depleted in comparison to control siRNA treated cells (Fig. 4.1A). Additionally, the concentration of other Kapβs was not affected as shown by global proteome analysis, confirming the specificity of the Kapβ1 siRNA oligos (Fig. 4.1B). The maximum level of CRM1 silencing was ~60% for treatment with 110 pmol of CRM1-specific siRNA2 (Fig. 4.1C). Incubation with higher amounts of siRNA2 did not improve the silencing efficiency, but rather promoted cellular death.

For immunofluorescence staining, we used Cy5-modified oligos to ensure that only siRNA-treated cells were analyzed. Depending on the specific siRNA condition, we found that the signal of Kapβ1 at the NE had reduced to 82-88% in silenced cells, accompanied by a ~30% increase in its NE-to-cytoplasm ratio (NE/C) (Fig. 4.2). Interestingly, this coincided with an increase in the NE signal of CRM1 of up to 121%, together with a ~14% increase in its NE-to-nucleus (NE/N) ratio. These observations suggest that the available pool of soluble Kapβ1 in the cytoplasm was deployed to replenish and reinforce the NPCs, resulting in a higher NE/C ratio. Still, the resulting enrichment of Kapβ1 is limited by the reduction in its abundance and thus is not able to return to pre-silencing levels. Moreover, the increase in the NE/N ratio for CRM1 suggests that additional CRM1 molecules were recruited from within the nucleus to fortify the NPC upon Kapβ1 depletion.

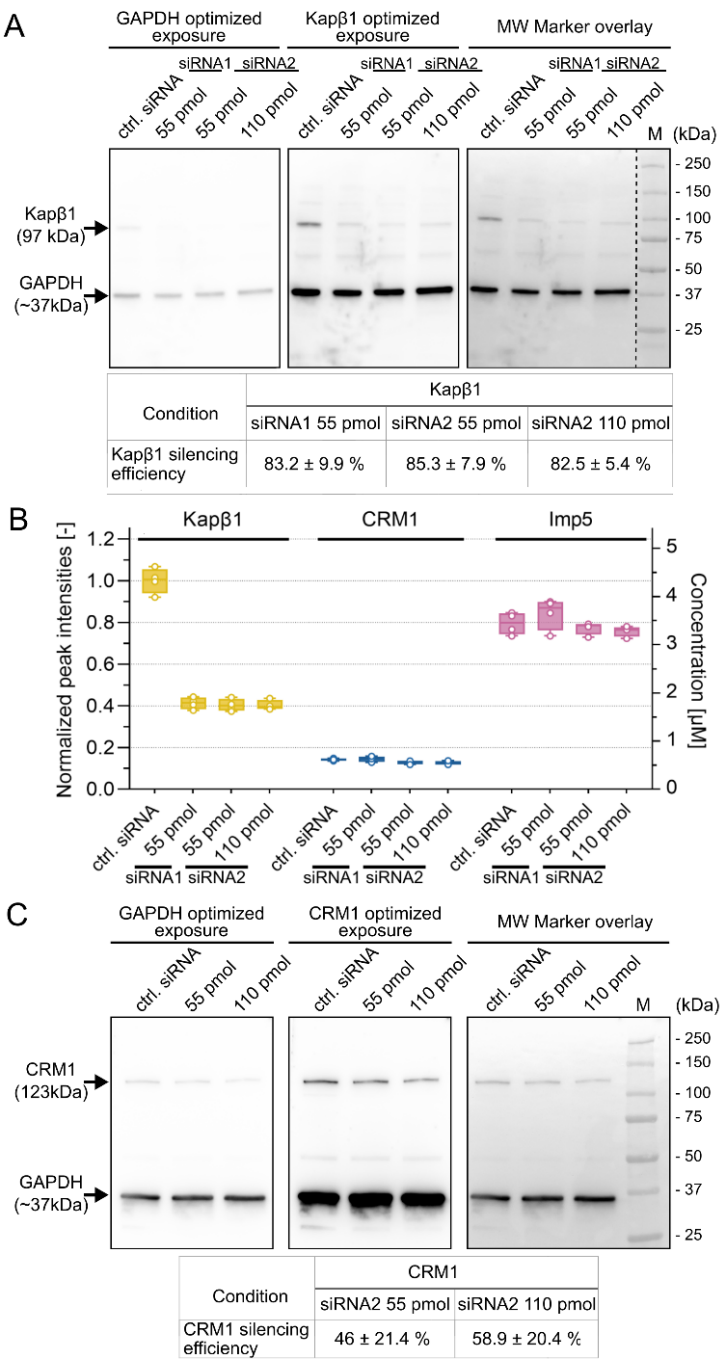

Figure 4.1 Quantitative analysis of Kapβs after siRNA treatment

(A) Quantification of Kapβ1 silencing in MDCK cells after treatment with Kapβ1-specific siRNA1 or siRNA2 at the amounts shown. The dashed line indicates the removal of unrelated sample lanes that were probed on the same membrane. (B) Proteomic analysis of Kapβ1, CRM1, and Imp5 cellular abundance before and after Kapβ1 silencing. Only Kapβ1 was significantly reduced in MDCK cells whereas CRM1 and Imp5 levels were not affected. All data points were normalized to the mean value of Kapβ1 abundance in control siRNA cells (n=4). (C) Analysis of CRM1 silencing efficiency in MDCK cells after treatment with CRM1-specific siRNA. See Materials and Methods in the main text for details. Note: In all cases, the chemiluminescence signal was recorded using different exposure times to optimally visualize GAPDH or a given Kapβ. For quantification, CRM1 and Kapβ1 signals were normalized to the corresponding GAPDH signal from the same lane. MW, molecular weight; M, marker.

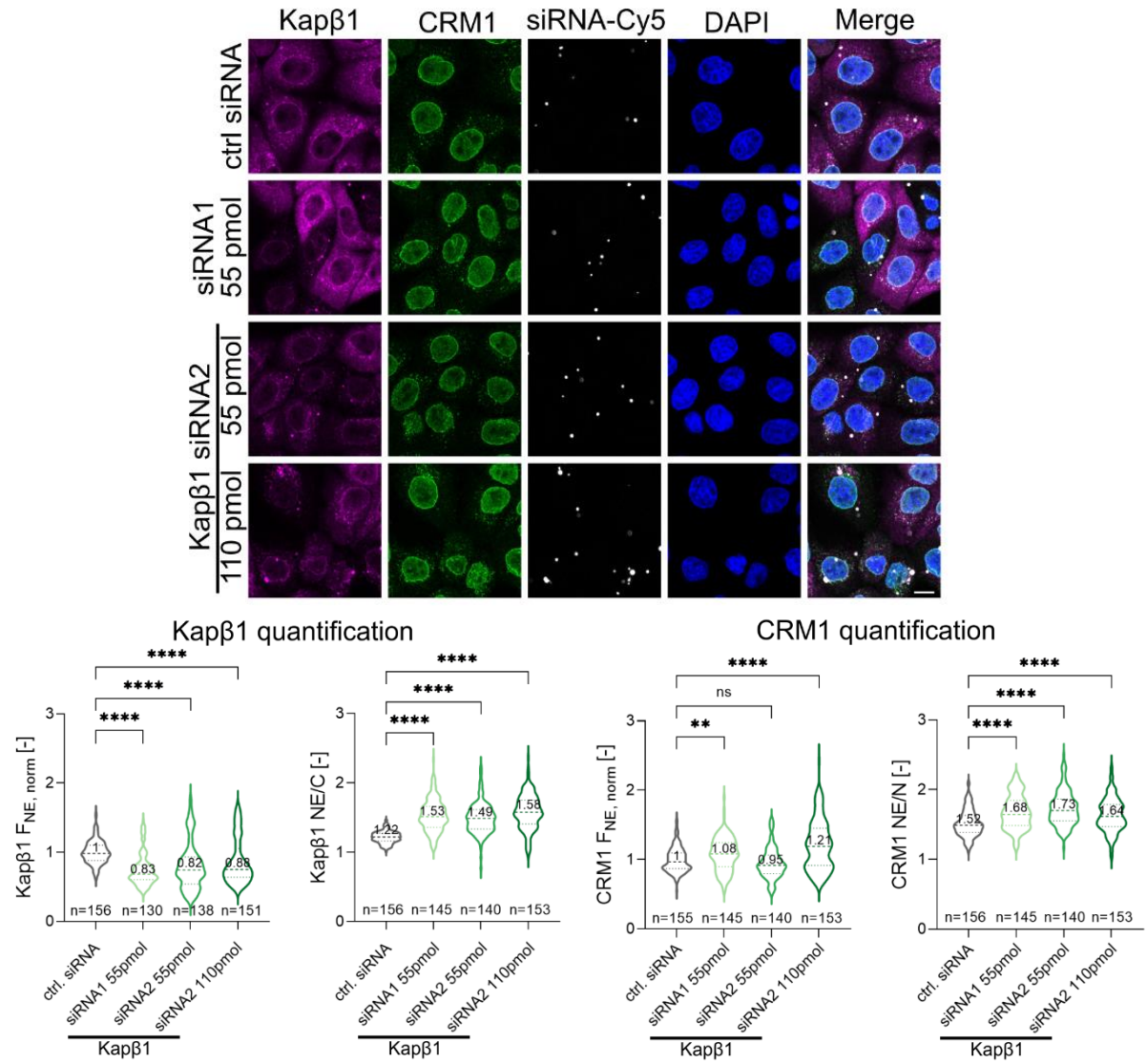

Figure 4.2 NE occupancy of CRM1 increases upon Kapβ1 silencing

*Immunofluorescence staining of MDCK cells reveals that a significant fraction of Kapβ1 is depleted from the NE following Kapβ1 silencing. This correlates with (i) an increased enrichment of CRM1 at the NE, and (ii) increases in both the NE/C and NE/N ratios of Kapβ1 and CRM1, respectively. This suggests that the cytoplasmic pool of Kapβ1, together with the nuclear pool of CRM1 have been recruited to compensate for the depleted Kapβ1 molecules at the NPCs. Statistical analysis was performed using the Kruskal-Wallis test. P adjusted values were calculated using Benjamini-Hochberg procedure (****= 0.0001, ** = 0.0021, ns = 0.1). Scale bar: 10 µm.*

Given that the binding of Kapβ1 and CRM1 to the FG Nups is comparable (Chapter 3.2), we rationalized that their observed behaviors might stem from differences in their cellular abundances. Indeed, the average cellular concentration of Kapβ1 was determined to be 4.3 ± 2.5 µM by quantitative mass spectrometry, from which its quantity was approximately 1.7 µM after knockdown (with 60% silencing efficiency) (Fig. 4.1B). This is consistent with previous cellular concentration estimates of Kapβ1, although their exact quantities depend on the organism and cell type (Quan et al., 2008; Wang et al., 2015). Importantly, Kapβ1 silencing

did not affect the cellular concentrations of CRM1 and Imp5, which remained at 0.61 ± 0.02 µM and 3.4 ± 0.2 µM, respectively. Considering final concentrations of all Kapβs of interest, we find that Kapβ1 outnumbers CRM1 within the NPC under wildtype conditions i.e., before silencing. After silencing, the remaining pool of Kapβ1 is sufficient to partially replenish the NPC, however with a larger fraction of CRM1 due to a shift in their binding equilibrium that follows from changes in their concentrations.

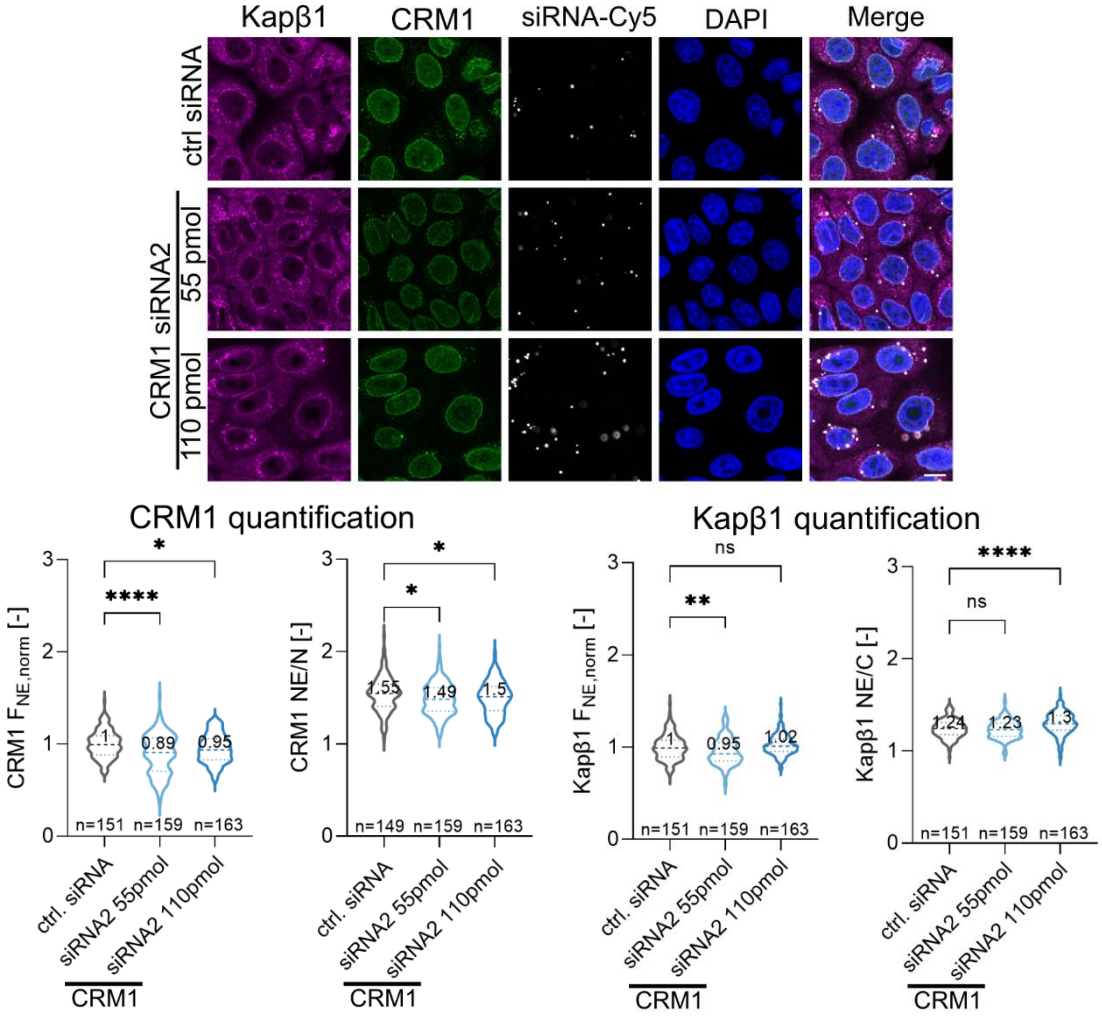

Figure 4.3 CRM1 silencing does not lead to significant changes in Kapβ1 occupancy.

*Only a small fraction of CRM1 is reduced at the NE following CRM1 silencing. This correlates with: (i) an enriched pool of Kapβ1 at the NE that is relatively unchanged, (ii) no change to the NE/N ratio of CRM1, and (iii) a slight increase in the NE/C ratio of Kapβ1. This suggests that only a small fraction of Kapβ1 is being recruited from the cytoplasm to compensate for depleted CRM1 molecules at the NPCs. Statistical analysis was performed using the Kruskal-Wallis test. P adjusted values were calculated using Benjamini-Hochberg procedure (****= 0.0001, ** = 0.0021, * = 0.0332, ns = 0.1). Scale bar: 10 µm.*

For this reason, we hypothesized that silencing CRM1 ought not to result in an increase of its NE/N ratio. As anticipated, ~50% CRM1 silencing (by Western blot analysis; Fig. 4.1C) resulted in a slight reduction of its NE signal and NE/N ratio (Fig. 4.3). This was accompanied by a small increase in the NE/C ratio of Kapβ1, which indicates that the soluble pool of CRM1 is insufficient to compensate for a reduction of its bound fraction at the NPC because (i) its concentration is below K_D (Fig. 3.5E), and (ii) it is greatly outbalanced by Kapβ1.

4.3 Kapβ1 depletion impairs NPC barrier function *in vivo*

To assess whether Kapβ enrichment fortifies the NPC permeability barrier *in vivo* we depleted endogenous Kapβ1 using the same siRNA conditions as above (i.e. siRNA1 55 pmol, siRNA2 55pmol, and siRNA2 110 pmol) in MDCK cells stably expressing 2xEGFP-NES (~55 kDa). We deliberately chose 2xEGFP-NES as a reporter for NPC leakage because it is disconnected from nuclear import and decouples the role of Kapβ1 as a barrier reinforcement from its import activity.

In comparison to control cells, Kapβ1 silencing resulted in a 16% average increase in the nuclear-to-cytoplasmic (N/C) ratio of 2xEGFP-NES from 0.37 up to 0.43 across the three silencing conditions (Fig. 4.4A). This signifies a passive leakage of 2xEGFP-NES back into the nucleus that might correspond to a 27% increase in NPC permeability based on the nucleocytoplasmic exchange model described in Cardarelli et. Al (Cardarelli et al., 2009). Briefly, the nuclear envelope permeability P_x for active transport is given by:

$$P_x = \frac{K_{eq} \cdot k_x^{N\to C} - k_x^{C\to N}}{(1 - K_{eq})}$$

where, K_{eq} is the equilibrium partition constant between the nucleus and the cytoplasm (i.e., nuclear-to-cytoplasmic (N/C) ratio), $k_x^{C\to N}$ is the effective active import and $k_x^{N\to C}$ is the effective active export rate. For 2xEGFP-NES, no active import is assigned $(k_x^{C\to N} = 0)$ and the rate of active export remains unchanged $(k_x^{N\to C} = const.)$. The shift in P_x can then be obtained by calculating the ratio of K_{eq} before and after siRNA knockdown.

We observed a similar, though less prominent backflow of 3xEGFP-NES (~81kDa) into the nucleus given that its N/C ratio increased from 0.28 to 0.31 (11%) after Kapβ1 silencing (Fig. 4.4A). This corresponds to a 15% increase in NPC permeability being consistent with a soft barrier whose effectiveness against passive diffusion gradually increases with the size of the permeant (Timney et al., 2016). Moreover, the increase in NPC permeability for 2xEGFP-NES

and 3xEGFP-NES exceeds the passive permeability reported for comparably sized non-specific cargoes by 3-5 times (Timney et al., 2016). Another key point to note is that following Kapβ1 silencing, CRM1-mediated export was insufficient to mitigate the backflow of NES-cargoes (Fig. 4.4A), despite the increase of the occupancy of this receptor at the NE (Fig. 4.2). As a positive control, we silenced CRM1 (Fig. 4.4B) to check how impairing 3xEGFP-NES export compares against its passive leakage into the nucleus. This resulted in a 29% increase in the N/C ratio from 0.28 to 0.36, which is three times stronger than Kapβ1 silencing (Fig 4.2). Hence, Kapβ1 depletion impairs NPC barrier function despite the partial compensation by CRM1.

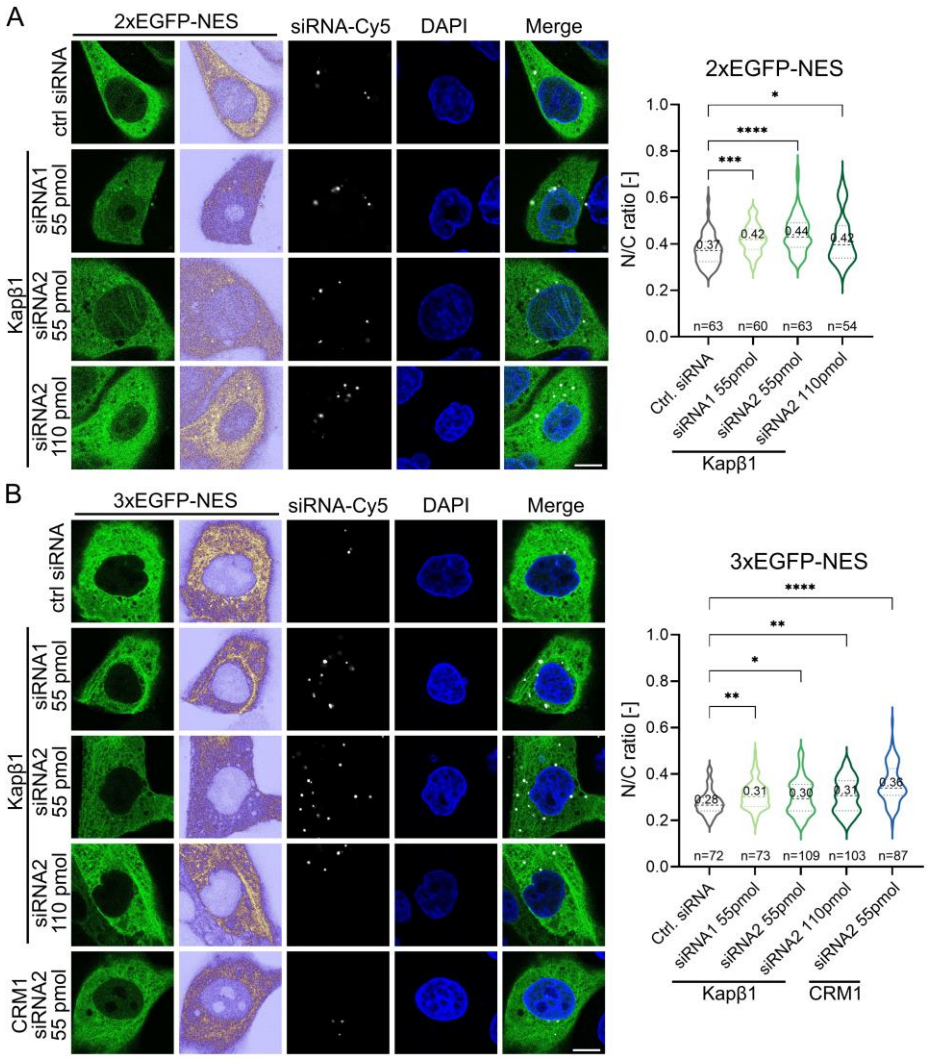

Figure 4.4 Kapβ1 enrichment fortifies the NPC permeability barrier in vivo

*(A) Silencing Kapβ1 shifts the steady-state distribution (N/C ratio) of 2xEGFP-NES into the nucleus as a result of increased NPC permeability (i.e., leak). (B) An increase of NPC permeability due to Kapβ1 silencing also results in a shift of 3xEGFP-NES into the nucleus. Impairing 3xEGFP-NES export via CRM1 silencing results in a qualitatively similar but larger shift in the N/C ratio. Statistical analysis was performed using the Kruskal-Wallis test. P adjusted values were calculated using the Benjamini-Hochberg procedure (****= 0.0001, ***= 0.0002, ** = 0.0021, * = 0.0332, ns = 0.1). Scale bars: 10 µm*

4.4 CRM1 reduction does not show to affect the NPC permeability barrier

Using the same rationale as in the previous section, we used 2xEGFP-NLS as a reporter to investigate the potential role of CRM1 as a barrier reinforcement. Since subcellular localization of this cargo is independent of CRM1-mediated export, utilizing this cargo as a 'leakage' reporter also allows us to decouple the transport and barrier reinforcement function of CRM1. However, in contrast to Kapβ1, CRM1 silencing had little to no effect on lowering the N/C ratio of 2xEGFP-NLS (Fig. 4.5). This suggests that any leakage out of the nucleus was below the detection limit due to an insufficient silencing efficiency of CRM1 siRNA (Fig. 4.1 and Fig. 4.3). Moreover, further attempts to increase CRM1 silencing efficiency did not improve the final outcome.

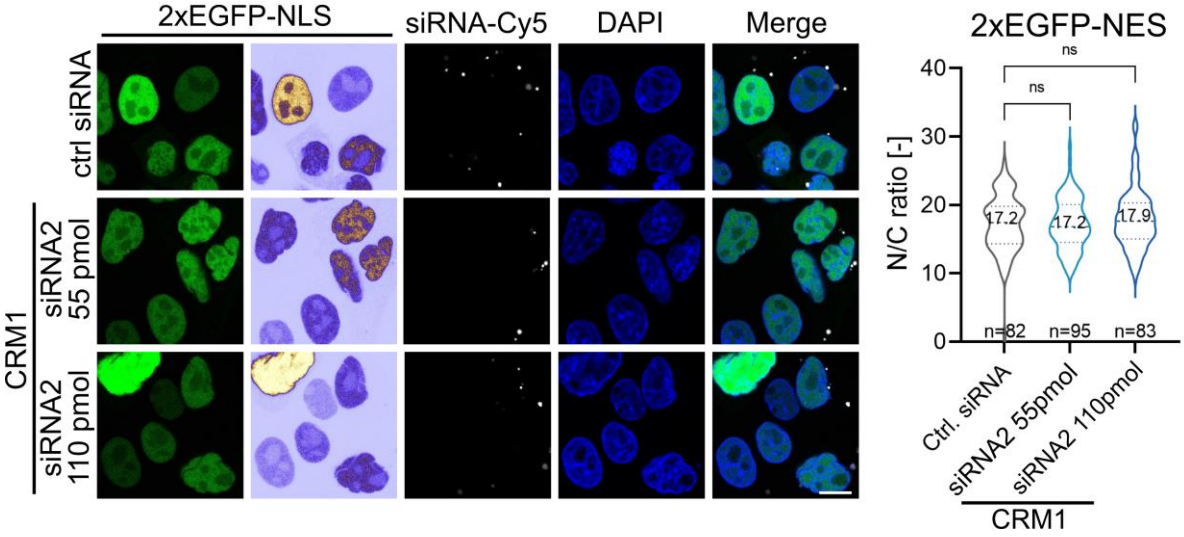

Figure 4.5 CRM1 depletion does not disturb the NPC permeability barrier

Silencing CRM1 does not show any detectable change to the N/C ratio of 2xEGFP-NLS. Statistical analysis was performed using the Kruskal-Wallis test. P adjusted values were calculated using the Benjamini-Hochberg procedure (ns = 0.1). Scale bar: 10 µm

4.5 NPC passive permeability increases upon Kapβ1 reduction

To further verify if Kapβs tighten NPC permeability, we performed fluorescence recovery after photobleaching (FRAP) in MDCK cells stably expressing 2xEGFP non-specific cargo. The advantage of FRAP is that it affects the fluorescence properties of the studied molecules (i.e. 2xEGFP) without disturbing their biochemical attributes or their diffusion/transport dynamics (Bizzarri et al., 2012). Applying the same three Kapβ1 silencing conditions as above enabled us to evaluate the recovery time of 2xEGFP in the nucleus before and after Kapβ1 depletion (Fig. 4.6A). In comparison with control cells, we observed a shorter

half-time recovery (τ) after Kapβ1 depletion, which signified an increase in passive nucleocytoplasmic exchange (Fig. 4.6C). The mean τ value reduced from 582 s to 527 s, 462 s, or 380 s depending on the silencing condition. Data obtained from FRAP measurements also allowed us to compute the permeability coefficient (P_X) of passive diffusion through the NE (Cardarelli et al., 2009) (See Chapter 4.9.7 for detailed description) (Fig. 4.6). The P_X is defined as:

$$P_X = \frac{1}{\tau} \cdot \left(\frac{K_{eq}}{V_C} + \frac{1}{V_N} \right)^{-1}$$

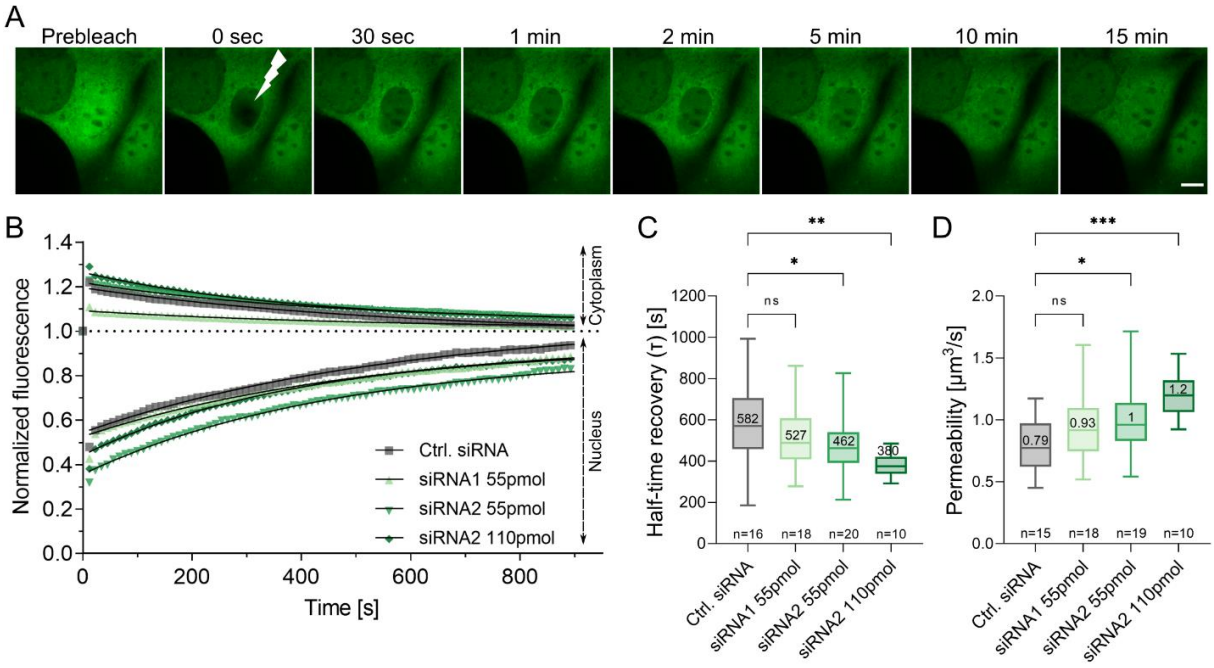

Figure 4.6 Kapβ1 depletion softens NPC permeability barrier against non-specific cargoes in vivo.

*(A) Representative image sequence showing the recovery of 2xEGFP in the nucleus obtained during a FRAP experiment in control siRNA-treated cells. Lightning indicates the nuclear photobleaching event at t = 0. Scale bar: 10 µm. (B) Fluorescence recovery curves (symbols) and their fits (black line) as obtained in individual cells. In all cases, an increase in nuclear fluorescence (normalized fluorescence <1) correlates to a concomitant decrease in cytoplasmic fluorescence (normalized fluorescence >1). Both nuclear recovery and cytoplasmic loss of fluorescence are characterized by similar time constants because Kapβs do not play a role in the passive diffusion of 2xEGFP. For clarity, only every tenth data point is shown. (C) Kapβ1 silencing expedites the passive exchange of 2xEGFP cargoes across NPCs as evidenced in the significant reduction of its recovery half-times (τ). (D) Kapβ1 silencing leads to an increase in NPC permeability for 2xEGFP cargoes. Statistical analysis was performed using the ordinary one-way ANOVA test. P adjusted values were calculated using the Benjamini-Hochberg procedure (***= 0.0002, ** = 0.0021, * = 0.0332, ns = 0.1). See main text for details.*

where V_N and V_C stand for the nuclear and cytoplasmic volumes, respectively, and K_{eq} is the equilibrium partition constant between the nucleus and cytoplasm. For MDCK cells, the following parameters were used: K_{eq} = 1 (for 2xEGFP cargo), V_C = 1760 ± 508 µm^3, and V_N = 600 ± 150 µm^3. Consequently, this analysis showed an increased permeability, which ranged from 18% to 27% and 52% over control cells, depending on the silencing condition used. Hence, a loss of Kapβ1 enrichment results in NPCs that are more amenable to the exchange of passive cargoes.

4.6 NPCs *in vivo* are saturated with Kapβ1

In contrast to the Kapβ1 silencing, an overexpression of Kapβ1 tagged with a near-infrared fluorescent protein (Kapβ1-iRFP) in MDCK cells did not result in an increase of τ nor a decrease of NE permeability (Fig. 4.7). This outcome suggests that Kapβ1 enrichment is near or at saturation levels in NPCs under physiological conditions (Fig. 2.5). This is consistent with equilibrium binding analysis (Fig. 3.2 and Fig. 3.5) which shows that further increase of Kapβ1 concentration changes its occupancy at the NPCs only marginally.

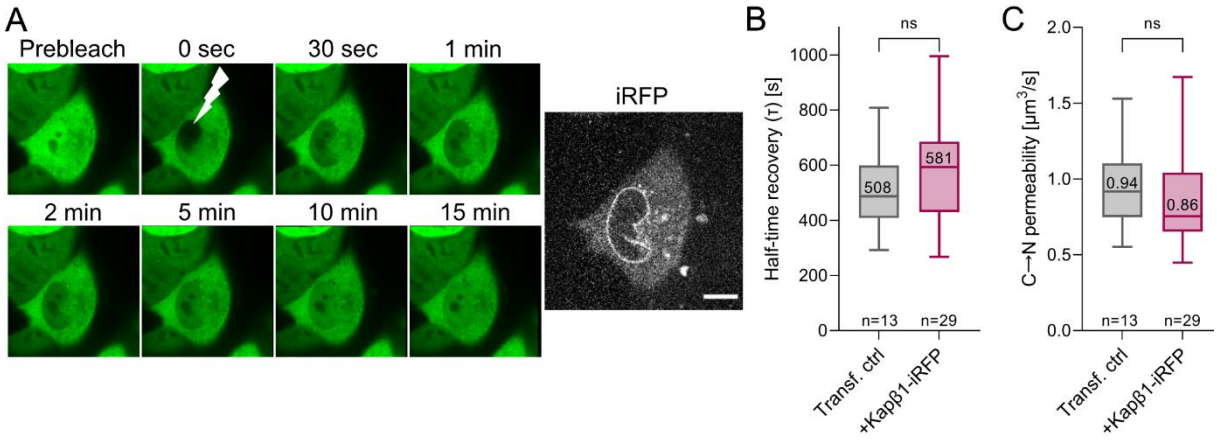

Figure 4.7 Overexpression of Kapβ1 does not further fortify the permeability barrier

(A) Fluorescence recovery of 2xEGFP within the nucleus in cells overexpressing Kapβ1-iRFP. The time elapsed per frame is 1s. Kapβ1-iRFP fluorescence is visualized on the last panel. Lightning indicates the nuclear photobleaching event at t = 0. Scale bar: 10 µm. (B) τ and (C) permeability for 2xEGFP cargo do not change significantly upon the Kapβ1-iRFP overexpression. Statistical analysis was performed using a non-parametric (Mann-Whitney) two-tailed test. Error bars denote minimum and maximum measured values.

4.7 The permeability barrier remains intact after CRM1 depletion

For completeness, we performed FRAP experiments in MDCK cells treated with siRNA against CRM1 (Fig. 4.8A, B). We found that in neither of the tested silencing conditions the speed of the 2xEGFP recovery was significantly different than in the control siRNA-treated cells

(Fig. 4.8C). Consequently, the NE permeability values remained similar across all the cells (Fig. 4.8D). This observation is consistent with the silencing results in the MDCK cells expressing 2xEGFP-NLS (Fig. 4.5), where no cargo leakage was observed upon CRM1 depletion. Nevertheless, NLS cargoes could be recaptured at the NPCs by Kapβ1 preventing its leakage and obscuring the changes to the NPC permeability. Therefore, the results obtained from the FRAP experiment confirm that the NPC permeability remains unaffected after CRM1 depletion.

It is important to point out that the half-time recovery values obtained for CRM1 silencing differ notably from FRAP results in Kapβ1 depleted cells (384 vs. 582 s in the control cells, respectively) (Fig. 4.6 and Fig. 4.8). This is due to the usage of different microscopy setups and thus different bleaching protocols which could cause such discrepancies (see Table 4.2 for comparison of the settings).

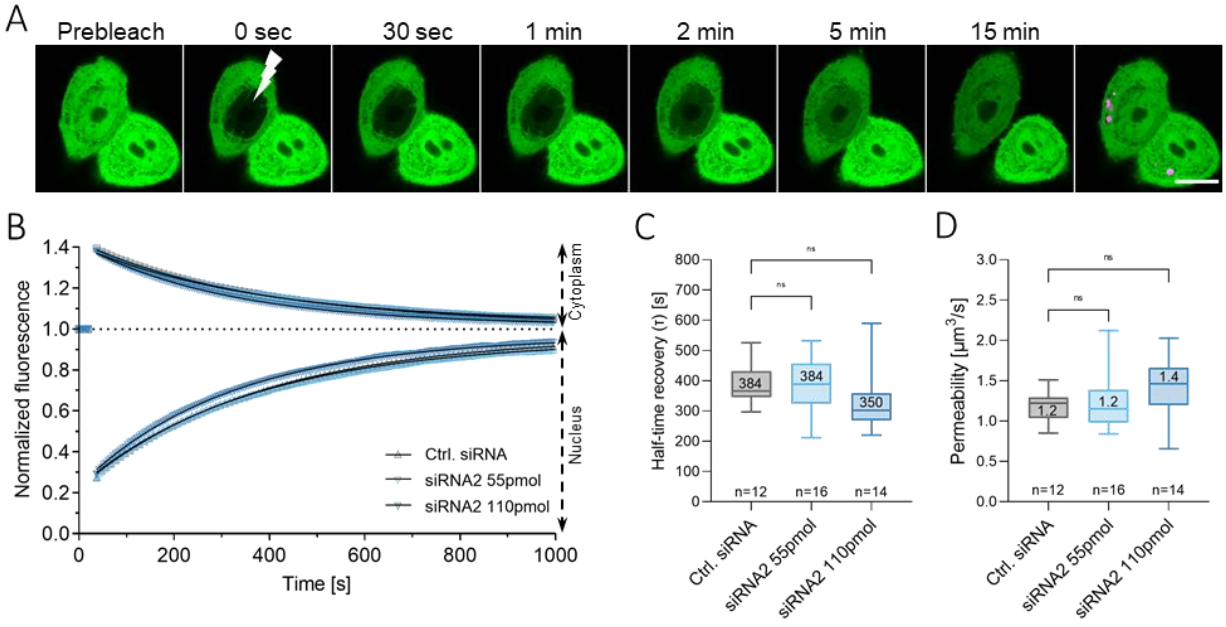

Figure 4.8 CRM1 depletion does not impair NPC permeability against 2xEGFP

(A) An example of the image sequence depicting 2xEGFP recovery after the nuclear FRAP in siRNA (110 pmol) treated cells. The last image shows that the chosen cell was indeed transfected with siRNA as indicated by the Cy5 signal (magenta). Lightning indicates the nuclear photobleaching event at t = 0. Scale bar: 10 µm. (B) Average fluorescence recovery curves (symbols) and their fits (black line). Bottom traces show signal recovery in the nucleus (normalized fluorescence <1), while the decay cures visualize a simultaneous decrease in cytoplasmic fluorescence (normalized fluorescence >1). For clarity, every other data point is shown. (C) Reduction of CRM1 at the NE does not affect the passive diffusion rate across the NPCs, as no significant differences were detected between control and treated cells. Statistical analysis was performed using the Kruskal Wallis test. P adjusted values were calculated using the Benjamini-Hochberg procedure (ns = 0.1).

4.8 Conclusions

NCT relies on diverse Kapβs that traverse NPCs to deliver their specific cargoes. However, it is unknown how many Kapβ molecules reside at the NPC nor how they compete for binding with the FG Nups *in vivo*. By utilizing various experimental approaches, we characterized the binding and competition behavior of three different Kapβs, i.e. Kapβ1, CRM1, and Imp5, which constitute some of the most abundant representatives of the Kapβ family. Combined with a mean-field model, our experiments reveal that the size of each Kapβ is enough to dictate its occupancy inside the NPC. As a simple example, different Kapβs characterized by the same cellular abundance and FG Nup-binding affinities would differ in the number of molecules residing within the NPC and can exclude each other solely because of the differences in their particle volumes. Since many structural details are still lacking such a minimal model does not take into account the number of FG binding pockets of each Kapβ, nor the interaction strength between Kapβs and FG, nevertheless, it reflects well Kapβs behavior *ex vivo* and to large extent also *in vivo*.

Moreover, we show that Kapβ1 depletion makes the permeability barrier of the NPCs less restrictive, thus increasing the fluxes between both compartments. Despite the apparent compensation that CRM1 provides after Kapβ1 depletion (Fig. 4.2 and Fig. 4.9), the NPC permeability barrier does not retain its full functionality. This is due to the relatively low cellular abundance of CRM1 (0.61 ± 0.02 µM) which limits its enrichment to only 50-60% of its maximum occupancy and thus allows only for the partial substitution of the Kapβ1 molecules missing from the NPC. In contrast, CRM1 reduction does not seem to significantly disturb the steady-state of the nucleocytoplasmic separation (Fig. 4.5). Bearing in mind the cellular concentrations of the Kapβs (Kapβ1: 4.32 ± 2.35 µM, CRM1: 0.61 ± 0.02 µM) (Fig. 2.5) and the level of their reduction (Kapβ1: 80-90%, CRM1: ~50%) (Fig. 4.1), this outcome could be explained by (i) a more significant contribution of Kapβ1 to the permeability barrier based on its cellular concentration, thus any disturbances in its occupancy would have a more substantial effect, and (ii) low wild-type occupancy of CRM1 at the NPCs (Fig. 4.9). We hypothesize that CRM1 contributes to the permeability barrier to a lower extent than Kapβ1 and its contribution can be diminished even further by competition with other Kapβs *in vivo*.

As discussed in Chapter 2.2., the role of the permeability barrier is not limited to the prevention of passive translocations. In the *in vivo* experiments, Kapβ1 could theoretically

replace only a subset of the CRM1 molecules missing from the NPC, and in such a scenario cargo leakage could still occur. However, Kapβ1 molecules are very efficient at recapturing small cargoes that diffuse through the NPC (e.g., RanGTP) and delivering them back to the nucleus. This is due to the high cytoplasmic abundance of Kapβ1 and its enrichment at the NPC, which shifts the binding equilibrium toward the formation of the import complex and its targeting to the NPC. In the reverse situation, partial replacement of Kapβ1 by CRM1 would not prevent the leakage of the export cargo. Unlike Kapβ1, CRM1 requires RanGTP to bind NES-cargos and form a functional export complex. Therefore, leakage prevention by recapturing the cargo at the NPC could not be effective in this case as all three components (i.e., CRM1, NES-cargo, and RanGTP) are required simultaneously (Fig. 2.2). Nevertheless, reduction of Kapβs enrichment at the NPCs increases its permeability for both, specific and non-specific cargoes, and disrupts nucleocytoplasmic partitioning *in vivo*.

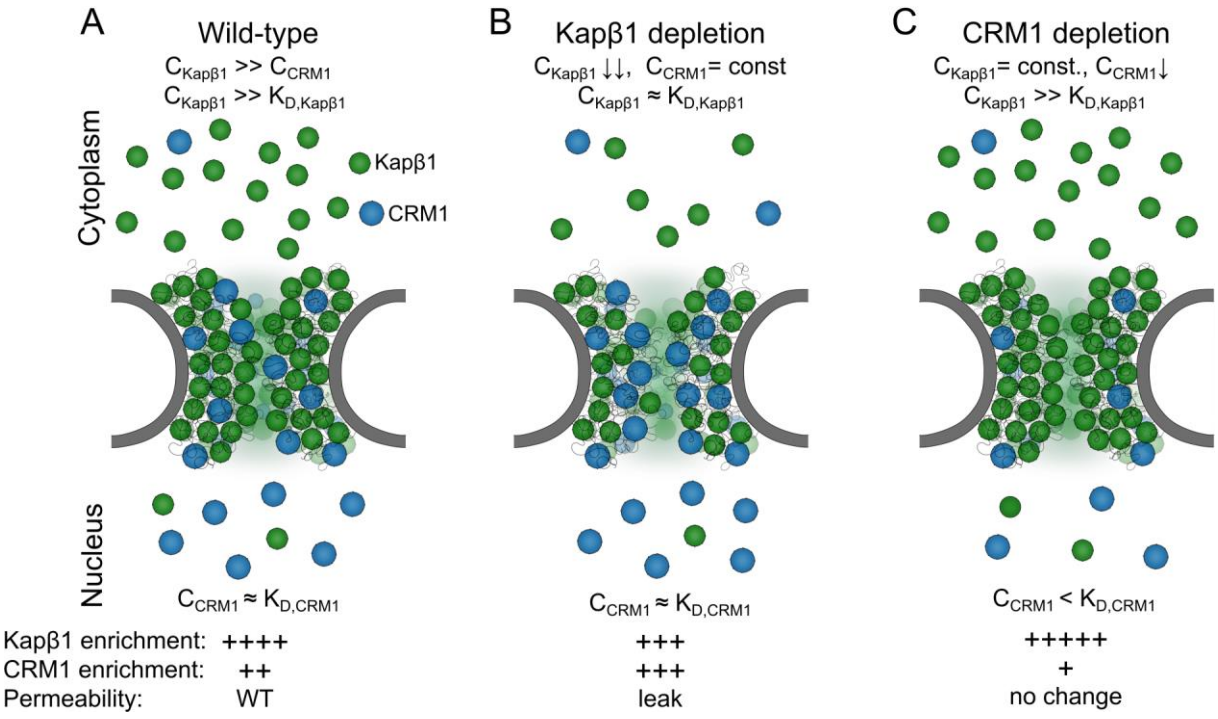

Figure 4.9 Summary of Kap enrichment and compensation at the NPC permeability barrier

(A) Enrichment of Kapβ1 and CRM1 at the NPC under wild-type conditions based on their respective cellular abundances (C_{Kap}), apparent binding affinities ($K_{D,Kap}$) to the FG Nups, and molecular volumes. (B) Depleting Kapβ1 significantly reduces its occupancy at the NPC, thereby allowing more CRM1 molecules to bind to the FG Nups. However, CRM1 compensation is constrained by its cellular concentration. (C) Depleting CRM1 does not elicit any detectable change to the permeability barrier due to (i) its low wild-type occupancy and (ii) dominance of Kapβ1. Note that the molecular volume of CRM1 is larger than Kapβ1.

Although molecular level evidence is so far missing, one cannot exclude that preferential FG Nup-specific interactions may influence the binding and occupancy of specific Kapβs at the NPC. For instance, the deletion of 50% of FG Nups in *S. cerevisiae* mutant strains impairs the import activity of Kap104 (the yeast homolog of Kapβ2/Transportin) and Kap121 (the yeast homolog of Imp5) but not Kap95 (the yeast homolog of Kapβ1) (Strawn et al., 2004). This suggests that the co-existence of different Kapβs or their competition at NPCs might also depend on binding to distinct combinations of FG Nups (Strawn et al., 2004; Terry and Wente, 2007). Our SPR experiments did not reveal strong binding preferences of Kapβ1, CRM1, or Imp5 however, our study was limited to only four representatives of FG Nups. Another important aspect concerns the link between Kapβ occupancy and the cell cycle. For example, Imp5 is required over a short period of time to import proteasomes following NE formation during mitosis, but not in G0/G1 phase up to late anaphase (Spits et al., 2019). Kapβ1-dependent import, however, remains functional during the entire cell cycle (Yasuhara et al., 2004). Furthermore, competitive behavior between Kapβ1 and CRM1 may be important for RanBP2/Nup358 localization during mitosis to impact development and cell fate (Gilistro et al., 2017).

The results presented in this thesis substantially expand on previous work and provide new insights into the inner workings of the NPC permeability barrier *in vivo*. In contrast to the NPC permeability models conceived based on the characteristics of purified FG Nups, in living cells the FG Nups (i.e., NPCs) are saturated with Kapβs and their complexes. As such this study demonstrates that Kapβs constitute *bona fide* constituents of the NPC, additionally fortifying the permeability barrier on top of their well-studied transport function. This validates previous *ex vivo* studies which showed that depleting endoKapβ1 abrogated NPC barrier function whereas adding back exoKapβ1 rescued it (Kapinos et al., 2017). Likewise, adding Kapβ1 (Lowe et al., 2015) and transportin (Mohr et al., 2009) further reduced NPC permeability against passive cargoes. Together with Kapβ1's ability to prevent uncontrolled leakage of Ran (Barbato et al., 2020) and other small cargoes, this work indicates that FG Nups are essential components of the NPC permeability barrier, but its optimal functionality is achieved only in synergy with Kapβs.

The findings described here are also important in the context of cellular pathologies and chronological (postmitotic) cell aging. For example, it has been demonstrated that during oxidative stress (Kodiha et al., 2004) and chronological cell aging (D'Angelo et al., 2009; Rempel

et al., 2019; Rempel et al., 2020) Kapβ1 binding at NE is reduced due to increased proteolysis, what in turn causes unrestricted leakage through the NPCs. Similarly, age-dependent disturbance of nucleocytoplasmic compartmentalization was correlated with depletion of RanBP17, which preoccupies NPCs in neurons (Mertens et al., 2015). Considering other pathological states described in Chapter 1.2, it is important to keep in mind that all NCT cycles are highly interlinked and thus perturbations to certain transport factors (e.g., RanGTP/GDP gradient) might negatively impact Kapβs enrichment, and as such cause NPC leakage and mislocalization of cargoes. Future studies will be necessary to examine the significance of Kapβ enrichment at the NPC in the context of cellular dysfunction and pathology.

4.9 Materials and Methods

4.9.1 siRNA design and validation

The siRNAs against dog Kapβ1 (F6X637_CANLF) and CRM1 (E2R9K4_CANLF) were designed using the InvivoGen siRNA design tool (https://www.invivogen.com/sirnawizard/design.php) (Table 4.1). For both proteins, two or three different oligos were selected, synthesized (Microsynth AG) and their efficiency was tested *via* immunoblotting. MDCK cells were transfected with the siRNA oligos at 40-50% confluency the day after passaging and split again 24 h later. Cell lysis and Western Blotting were performed 2 days after the transfection. The most efficient oligos were chosen for further experiments. siRNA oligos were modified with Cy5 at the 3' end of their antisense strand to visualize the cells affected by siRNA treatment.

Table 4.1 siRNA sequences

Target	*siRNA name*	*Sequence of a sense strand (5'-3')*
CRM1 (E2R9K4)	siRNA1_CRM1_Clupus	GTCAACAAGTTAGGAGGACAT
	siRNA2_CRM1_Clupus	GACAATGCATGCGTCAATACT
	siRNA3_CRM1_Clupus	GCTCTTTACACTGACAATGAT
Kapβ1 (F6X637)	siRNA1_KPNB1	GCUGGCGGCUACAAAUGCA
	siRNA2_KPNB1	GAGUCGACAUUGGAAGCUA

4.9.2 Western Blotting

Western blotting (WB) was used to confirm the silencing efficiency of the designed siRNA oligos. The day after transfection cells were split into a 6-well plate and lysed 24 h later. Lysis was performed in RIPA buffer (ThermoFisher, Cat. No. 89900) supplemented with cOmplete

Protease inhibitor cocktail (Roche, Cat. No. 11873580001), benzonase (Novagen, Cat. No. 70746-3), and phosphatase inhibitors 2 and 3 (Sigma Aldrich, Cat. No. P5726 & P0044). Lysates were spun down for 15 min at 15000 x g at 4 °C and total protein concentration was determined using Pierce BCA assay (ThermoFisher, Cat. No. 23227). For each sample, the same total amount of proteins was resolved by SDS-PAGE (12 % PAGE at 0.1 % SDS) and transferred onto nitrocellulose membranes (Trans-Blot Turbo Midi 0.2 µm, Bio-Rad, Cat. No. 1704158) using a Trans-Blot Turbo Transfer System. After the transfer, membranes were blocked with 0.1 % (wt/vol) blocking reagent (Roche, Cat. No. 11096176001) in TBST for at least 1 h at RT and probed for Kapβ1 [abcam, ab2811 (3E9)] or CRM1 (Antikörper, Cat. No. ABIN2778849). Simultaneously, membranes were probed for GAPDH (α-rabbit: ThermoFisher, Cat. No. PA1-987; α-mouse: Proteintech, Cat. No. 60004-1-Ig) to allow for the signal normalization and quantification.

ECL-conjugated anti-mouse (GE Healthcare, Cat. No. NA931V) and anti-rabbit (abcam, Cat. No. ab6721) secondary antibodies were used for the immunodetection. Finally, membranes were developed in Fusion FX (Vilber Lourmat) system and the chemiluminescent signal was quantified using Fiji (ImageJ).

4.9.3 Knockdown of Kapβ1 and CRM1 in stable MDCK cell lines

MDCK stable cell lines expressing NLS- or NES-cargos were plated in a 12-well plate and transfected with siRNA oligos the next day. Cells expressing NES-cargos were treated with siRNA1_KPNB1 (55 pmol) or siRNA2_KPNB1 (55 or 110 pmol), and siRNA2_CRM1_Clupus (55 or 110 pmol) was added to the cells expressing NLS-cargo. The day after that, transfected cells were split onto 18 mm round glass coverslips and fixed with PFA 24 h later. Subsequently, cells were incubated in 1 % (wt/vol in PBS (Sigma Aldrich)) BSA (Sigma Aldrich) for 30 min at RT and with DAPI (5 µg/ml in 1%BSA, Thermo Fisher, Cat. No. 62248) for 15-20 min at RT. Coverslips were mounted using Vectashield (Vector Laboratories, Cat. No. H-1000) antifade mounting medium and sealed using nail polish.

4.9.4 Immunofluorescence staining

One day after siRNA treatment, MDCK cells were plated on the glass coverslips (#1.5) allowing them to adhere for ~24h. Afterward, cells were rinsed twice with PBS (Sigma Aldrich) and fixed in 4 % paraformaldehyde (PFA) (Sigma Aldrich, Cat. No. HT501128) for 15 min at RT. Next, samples were washed three times for 5 min with PBS and permeabilized with 0.2 % Triton-

X (in PBS). After three more washes with 1% BSA (Sigma Aldrich, Cat. No. A9647) in PBS for 5 min each, coverslips were left for >1h in 1% BSA solution for blocking. Subsequently, the primary antibodies against Kapβ1 (abcam, Cat. No. ab2811 (3E9)) and CRM1 (rabbit antibody, kind gift from R. Kehlenbach, University of Göttingen, Göttingen, Germany) (in 1% BSA) were applied for 1h at RT. Following another triple washing step (3x5 min in 1 % BSA), the samples were incubated with secondary antibodies (goat anti-mouse Alexa-568 (Thermo Fisher Scientific, Cat. No. A11004); goat anti-rabbit Alexa-488 (Thermo Fisher Scientific, Cat. No. A11034) and DAPI (Thermo Fisher, Cat. No. 62248) solution in 1 % BSA for 1 h at room temperature and protected from light. After the last washing step (3x5 min in 1 % BSA), coverslips were mounted onto glass slides with Vectashield medium and sealed with nail polish.

4.9.5 Confocal microscopy, imaging, and analysis

Fluorescence images of fixed samples were obtained at room temperature using an LSM880 inverted confocal microscope with an oil-immersed 63×/1.4 NA PLAN APO objective. The system was equipped with a widefield camera and an Airyscan detector (ZEISS). Fluorescence quantification of IF staining and cargo leakage experiments were performed using CellProfiler software (Kamentsky et al., 2011). DAPI channel was used for initial image segmentation. For IF staining of Kapβs, nuclear envelope, nucleus, and cytoplasm ROIs were created by shrinking or expanding the original DAPI-defined regions. In cargo leakage experiments, only nuclear and cytoplasmic ROIs were specified. In both types of experiments, the ROIs of interest were used to quantify the mean fluorescence intensity across all channels. The number of analyzed cells per condition is specified in the figures.

4.9.6 Cell and nuclear volume measurements

MDCK cells stably expressing EGFP-NLS were split into 8-well ibidi slides at 10000-15000 cells/cm^2 density. The next day cells were imaged using a 3i spinning disk confocal set up based on Zeiss Axio Observer stand (Intelligent Imaging Innovations GmbH) equipped with a 1.4NA 63x plane apochromatic objective, EMCCD camera (Evolve(R) 512, Photometrics) and a humidified climate control system at 37°C supplemented with 5% CO2 (Okolab). Cells were illuminated with a 488 nm laser and the z-stacks were collected at 0.2 µm steps to cover the entire cell volume. Collected images were then deconvolved using Huygens Remote Manager (Settings: NA = 1.4; λ_{ex} = 488 nm, λ_{em} = 525 nm, Immersion medium: n_{oil} = 1.518; medium refractive index: n_{buffer} = 1.339; XY pixel size: 127 nm; Z-step: 200 nm; Backprojected pinhole radius: 198.41 nm;

Backprojected Pinhole Spacing: 2.01 µm). Imaris Cell package within Bitplane Imaris software was then used to measure the nuclear (V_N) and total (V_T) volume of each cell. Cytoplasmic volume (V_C) was then calculated by subtracting both values: $V_C = V_T - V_N$.

4.9.7 Fluorescent Recovery After photobleaching (FRAP) experiments

MDCK cells stably expressing 2xEGFP were transfected with Kapβ1-iRFP plasmid or siRNA oligonucleotides against Kapβ1 or CRM1. After 24 h, the cells were plated in an eight-well µ-Slide (ibidi) at ~15,000 cells/cm2 density, and, on the next day, FRAP experiments were performed in a Phenol Red–free medium (Thermo Fisher Scientific, Cat. No. 51200046). Cells treated with siRNA against Kapβ1 were visualized using SlideBook software and photobleached using a 3i spinning disk confocal setup built on a Zeiss Axio Observer stand (Intelligent Imaging Innovations). The system was equipped with a 1.4 NA/63× Plan Apochromat objective, EM charge-coupled device camera (Evolve 512; Photometrics), and a humidified climate control system (37°C, 5% CO2; Okolab). The effect of the CRM1 silencing, however, was tested using the LSM880 inverted confocal microscope with an oil-immersed 63×/1.4 NA PLAN APO objective equipped with a widefield camera and Airyscan detector (ZEISS) (Table 4.2). Movies from at least three independent experiments were collected and analyzed. Owing to differences in experimental design, statistical analysis of Kapβ1 and CRM1 silencing experiments was performed with control siRNA treated cells as the reference, whereas Kapβ1-iRFP overexpression experiments were compared to the mock-transfected cells.

Table 4.2 FRAP experimental settings

Setting	*Kapβ1 silencing/overexpression*	*CRM1 silencing*
Microscope	Spinning disk 3i Mariana	LSM880
Bleached nuclear region [µm²]	8	11
Prebleaching scans	10	5
Bleaching iterations	3	
Bleaching pixel dwell time	10 ms	169.5 µs
Laser power	100 % (3.4 mW)	100%
Interval [s]	1	5
Total no. of cycles	900	200

4.9.8 Analysis of FRAP half-time recovery (τ)

Collected movies were exported to TIFF files using SlideBook 6 software. Movies were checked for the oversaturated pixels and corrected for the motility of the cells in Fiji using the stack

registration (StackReg) plugin. For better visualization of the compartments 'Rainbow' LUT was used. Importantly, none of these steps affect the raw pixel intensity values.

Boundaries of the nuclear, cytoplasm, and background ROIs were hand-drawn to ensure that selected regions stay within the bounds of the compartment for the duration of the movies. The average fluorescent intensities of the nucleus or the entire cell were calculated based on the average ROIs fluorescence intensities and their area following the equations:

average nuclear fluorescence: $F_N = F_{N,ROI1} \times A_N$

and average whole-cell fluorescence: $F_{WC} = \frac{F_{N,ROI1} \times A_N + (A_{WC} - A_N) \times F_{C,ROI2}}{A_{WC}}$,

where:

F_N- average fluorescence of the nucleus

F_{WC}- average fluorescence of the whole cell

$F_{N,ROI1}$- average fluorescence of the drawn nuclear ROI (ROI1)

$F_{C,ROI2}$- average fluorescence of the drawn cytoplasm ROI (ROI2)

A_N- nucleus area

A_{WC}- whole-cell area

For each movie frame, a time-stamp and fluorescent intensity values of the nucleus, whole cell, and background were exported and saved in a .xls file.

Passive nucleocytoplasmic exchange of 2xEGFP was modeled following Cardarelli et al. (Cardarelli et al., 2009; Cardarelli et al., 2007). Fluorescence values at each time point were first background-subtracted

$$F(t)_{N'} = F(t)_N - F(t)_B$$

$$F(t)_{C'} = F(t)_C - F(t)_B$$

$$F(t)_{WC'} = F(t)_{WC} - F(t)_B$$

where $F(t)_N$ is the fluorescence intensity in the nucleus, $F(t)_C$ is the fluorescence intensity in the cytoplasm, $F(t)_{WC}$ is the whole cell average fluorescence, and $F(t)_B$ is the fluorescence intensity of the background. A double normalization was then used to correct for differences in acquisition bleaching or laser intensity fluctuations given by

$$F(t)_{norm}^{double} = \left(\frac{\frac{1}{n_{pre}} \cdot \sum_{t=1}^{n_{pre}} F(t)_{WC'}}{F(t)_{WC'}} \right) \cdot \left(\frac{F(t)_{N/C'}}{\frac{1}{n_{pre}} \cdot \sum_{t=1}^{n_{pre}} F(t)_{N/C'}} \right),$$

where n_{pre} stands for the number of the pre-bleached images thereby setting the pre-bleached fluorescence to unity. Normalized nuclear and cytoplasmic fluorescence data were fitted with two mono-exponential equations to extract the half-time recovery values (τ):

$$F_C(t) = F_C^{\infty} + (F_C^0 - F_C^{\infty}) \cdot e^{-t/\tau}$$

$$F_N(t) = F_N^{\infty} + (F_N^0 - F_N^{\infty}) \cdot e^{-t/\tau}$$

where F_C^{∞} and F_N^{∞} represent the fluorescent signal of the cargo in the cytoplasm and nucleus at equilibrium, respectively. F_C^0 and F_N^0 correspond to the global concentration of cargo in the cytoplasm and nucleus (emissive + bleached).

4.9.9 Analysis of NPC permeability changes

Knowing the properties of the cargo used in the FRAP experiments we could assume that: (i) 2xEGFP only diffuses passively through NPCs and its steady-state distribution is not affected by active transport; and (ii) 2xEGFP is fully mobile in the cell and does not interact with any cellular components. In this manner, K_{eq} remains as 1. This is true prior to and at an infinite time after the photobleaching

$$K_{eq} = [X]_N^{\infty} / [X]_C^{\infty}$$

Using the τ value and the volumes calculated as described in Chapter 4.9.8 and Chapter 4.9.6, the nuclear envelope permeability coefficient of passive diffusion (P_X) can be calculated

$$P_X = \frac{1}{\tau} \cdot \left(\frac{K_{eq}}{V_C} + \frac{1}{V_N} \right)^{-1}$$

where V_N and V_C stand for the nuclear and cytoplasmic volumes, respectively, and K_{eq} is the equilibrium partition constant between the nucleus and cytoplasm. For MDCK cells, we used

K_{eq}- ratio at equilibrium (=1 for 2xEGFP)

V_N - nuclear volume (600 ± 150 µm^3)

V_C - cytoplasmic volume (1760 ± 508 µm^3)

Subsequently, distributions of the data points were checked for normality and statistical analysis was performed using one-way ANOVA corrected for multiple comparisons (False Discovery Rate [FDR]) using Benjamini-Hochberg Procedure.

4.10 References

Barbato, S., Kapinos, L.E., Rencurel, C., and Lim, R.Y.H. (2020). Karyopherin enrichment at the nuclear pore complex attenuates Ran permeability. J Cell Sci.

Ben-Efraim, I., and Gerace, L. (2001). Gradient of increasing affinity of importin beta for nucleoporins along the pathway of nuclear import. J Cell Biol *152*, 411-417.

Bizzarri, R., Cardarelli, F., Serresi, M., and Beltram, F. (2012). Fluorescence recovery after photobleaching reveals the biochemistry of nucleocytoplasmic exchange. Anal Bioanal Chem *403*, 2339-2351.

Cardarelli, F., Bizzarri, R., Serresi, M., Albertazzi, L., and Beltram, F. (2009). Probing Nuclear Localization Signal-Importin alpha Binding Equilibria in Living Cells. J Biol Chem *284*, 36638-36646.

Cardarelli, F., Serresi, M., Bizzarri, R., Giacca, M., and Beltram, F. (2007). In vivo study of HIV-1 Tat arginine-rich motif unveils its transport properties. Mol Ther *15*, 1313-1322.

Christie, M., Chang, C.W., Rona, G., Smith, K.M., Stewart, A.G., Takeda, A.A., Fontes, M.R., Stewart, M., Vertessy, B.G., Forwood, J.K., *et al.* (2016). Structural biology and regulation of protein import into the nucleus. J Mol Biol *428*, 2060-2090.

Conti, E., Muller, C.W., and Stewart, M. (2006). Karyopherin flexibility in nucleocytoplasmic transport. Curr Opin Struct Biol *16*, 237-244.

D'Angelo, M.A., Raices, M., Panowski, S.H., and Hetzer, M.W. (2009). Age-Dependent Deterioration of Nuclear Pore Complexes Causes a Loss of Nuclear Integrity in Postmitotic Cells. Cell *136*, 284-295.

Gilistro, E., de Turris, V., Damizia, M., Verrico, A., Moroni, S., De Santis, R., Rosa, A., and Lavia, P. (2017). Importin-beta and CRM1 control a RANBP2 spatiotemporal switch essential for mitotic kinetochore function. J Cell Sci *130*, 2564-2578.

Kalita, J., Kapinos, L.E., and Lim, R.Y.H. (2021). On the asymmetric partitioning of nucleocytoplasmic transport – recent insights and open questions. J Cell Sci *134*, jcs240382.

Kamentsky, L., Jones, T.R., Fraser, A., Bray, M.A., Logan, D.J., Madden, K.L., Ljosa, V., Rueden, C., Eliceiri, K.W., and Carpenter, A.E. (2011). Improved structure, function and compatibility for CellProfiler: modular high-throughput image analysis software. Bioinformatics *27*, 1179-1180.

Kapinos, L.E., Huang, B., Rencurel, C., and Lim, R.Y.H. (2017). Karyopherins regulate nuclear pore complex barrier and transport function. J Cell Biol *216*, 3609-3624.

Kapinos, L.E., Schoch, R.L., Wagner, R.S., Schleicher, K.D., and Lim, R.Y. (2014). Karyopherin-centric control of nuclear pores based on molecular occupancy and kinetic analysis of multivalent binding with FG nucleoporins. Biophys J *106*, 1751-1762.

Kirli, K., Karaca, S., Dehne, H.J., Samwer, M., Pan, K.T., Lenz, C., Urlaub, H., and Gorlich, D. (2015). A deep proteomics perspective on CRM1-mediated nuclear export and nucleocytoplasmic partitioning. Elife *4*.

Kodiha, M., Chu, A., Matusiewicz, N., and Stochaj, U. (2004). Multiple mechanisms promote the inhibition of classical nuclear import upon exposure to severe oxidative stress. Cell Death Differ *11*, 862-874.

Lim, R.Y.H., Huang, B., and Kapinos, L.E. (2015). How to operate a nuclear pore complex by Kap-centric control. Nucleus *6*, 366-372.

Lowe, A.R., Tang, J.H., Yassif, J., Graf, M., Huang, W.Y., Groves, J.T., Weis, K., and Liphardt, J.T. (2015). Importin-beta modulates the permeability of the nuclear pore complex in a Ran-dependent manner. Elife *4*.

Malekian, B., Schoch, R.L., Robson, T., Ferrand-Drake Del Castillo, G., Xiong, K., Emilsson, G., Kapinos, L.E., Lim, R.Y.H., and Dahlin, A. (2018). Detecting Selective Protein Binding Inside Plasmonic Nanopores: Toward a Mimic of the Nuclear Pore Complex. Front Chem *6*, 637.

Mertens, J., Paquola, A.C.M., Ku, M.C., Hatch, E., Bohnke, L., Ladjevardi, S., McGrath, S., Campbell, B., Lee, H., Herdy, J.R.*, et al.* (2015). Directly Reprogrammed Human Neurons Retain Aging-Associated Transcriptomic Signatures and Reveal Age-Related Nucleocytoplasmic Defects. Cell Stem Cell *17*, 705-718.

Mohr, D., Frey, S., Fischer, T., Guttler, T., and Gorlich, D. (2009). Characterisation of the passive permeability barrier of nuclear pore complexes. Embo Journal *28*, 2541-2553.

Pulupa, J., Prior, H., Johnson, D.S., and Simon, S.M. (2020). Conformation of the nuclear pore in living cells is modulated by transport state. Elife *9*.

Pyhtila, B., and Rexach, M. (2003). A gradient of affinity for the karyopherin Kap95p along the yeast nuclear pore complex. J Biol Chem *278*, 42699-42709.

Quan, Y., Ji, Z.L., Wang, X., Tartakoff, A.M., and Tao, T. (2008). Evolutionary and transcriptional analysis of karyopherin beta superfamily proteins. Molecular & Cellular Proteomics *7*, 1254-1269.

Rempel, I.L., Crane, M.M., Thaller, D.J., Mishra, A., Jansen, D.P., Janssens, G., Popken, P., Aksit, A., Kaeberlein, M., van der Giessen, E.*, et al.* (2019). Age-dependent deterioration of nuclear pore assembly in mitotic cells decreases transport dynamics. Elife *8*.

Rempel, I.L., Steen, A., and Veenhoff, L.M. (2020). Poor old pores-The challenge of making and maintaining nuclear pore complexes in aging. FEBS J *287*, 1058-1075.

Schoch, R.L., Kapinos, L.E., and Lim, R.Y. (2012). Nuclear transport receptor binding avidity triggers a self-healing collapse transition in FG-nucleoporin molecular brushes. Proceedings of the National Academy of Sciences of the United States of America *109*, 16911-16916.

Spits, M., Janssen, L.J., Voortman, L.M., Kooij, R., Neefjes, A.C.M., Ovaa, H., and Neefjes, J. (2019). Homeostasis of soluble proteins and the proteasome post nuclear envelope reformation in mitosis. J Cell Sci *132*.

Strawn, L.A., Shen, T.X., Shulga, N., Goldfarb, D.S., and Wente, S.R. (2004). Minimal nuclear pore complexes define FG repeat domains essential for transport. Nat Cell Biol *6*, 197-206.

Tan, P.S., Aramburu, I.V., Mercadante, D., Tyagi, S., Chowdhury, A., Spitz, D., Shammas, S.L., Grater, F., and Lemke, E.A. (2018). Two Differential Binding Mechanisms of FG-Nucleoporins and Nuclear Transport Receptors. Cell reports *22*, 3660-3671.

Terry, L.J., and Wente, S.R. (2007). Nuclear mRNA export requires specific FG nucleoporins for translocation through the nuclear pore complex. J Cell Biol *178*, 1121-1132.

Tetenbaum-Novatt, J., Hough, L.E., Mironska, R., McKenney, A.S., and Rout, M.P. (2012). Nucleocytoplasmic Transport: A Role for Nonspecific Competition in Karyopherin-Nucleoporin Interactions. *11*, 31-46.

Timney, B.L., Raveh, B., Mironska, R., Trivedi, J.M., Kim, S.J., Russel, D., Wente, S.R., Sali, A., and Rout, M.P. (2016). Simple rules for passive diffusion through the nuclear pore complex. J Cell Biol *215*, 57-76.

Wagner, R.S., Kapinos, L.E., Marshall, N.J., Stewart, M., and Lim, R.Y.H. (2015). Promiscuous binding of Karyopherinbeta1 modulates FG nucleoporin barrier function and expedites NTF2 transport kinetics. Biophys J *108*, 918-927.

Wang, M., Herrmann, C.J., Simonovic, M., Szklarczyk, D., and von Mering, C. (2015). Version 4.0 of PaxDb: Protein abundance data, integrated across model organisms, tissues, and cell-lines. Proteomics *15*, 3163-3168.

Yasuhara, N., Takeda, E., Inoue, H., Kotera, I., and Yoneda, Y. (2004). Importin alpha/beta-mediated nuclear protein import is regulated in a cell cycle-dependent manner. Exp Cell Res *297*, 285-293.

Zilman, A. (2018). Aggregation, Phase Separation and Spatial Morphologies of the Assemblies of FG Nucleoporins. Journal of Molecular Biology *430*, 4730-4740.

Chapter 5

Outlook

Adapted from

The role of nucleocytoplasmic transport in mechanotransduction

Elena Kassianidou, Joanna Kalita and Roderick Y. H. Lim

Published in Experimental Cell Research, 377, 86-93,

j.yexcr.2019.02.009 (2019)

5.1 Role of NCT in mechanotransduction

Cells are able to recognize, adapt and respond to mechanical cues through the activation of different signaling pathways. Such mechanosensing involves activation of the intracellular signaling cascades which require nucleocytoplasmic shuttling of the transcription factors (TFs) (Fig. 5.1). These include Yes-associated protein (YAP) (Elosegui-Artola et al., 2017), Myocardin-related transcription factor (MRTF) (Iyer et al., 2012), and Hypoxia-Inducible Factors (HIFs) (Depping et al., 2008; Masoud and Li, 2015). While it is largely appreciated that TFs respond to extracellular mechanical and biochemical stimuli, much less is known about how they interact with the NCT machinery to shuttle across NPCs. It has been shown, for example, that NPC composition and Kapβ expression profiles vary among tissue types and developmental stages, thereby regulating the entry of specific cargo including TFs in the nucleus at specific time points (Oka and Yoneda, 2018; Poon and Jans, 2005). Moreover, the vast number of Kapβ isoforms and FG Nups may allow the cell to be at different NCT "stages" where specific NLSs are favored over others. Since processes such as developmental progression, stem cell differentiation, and cell transformation are also highly regulated by external biophysical cues,

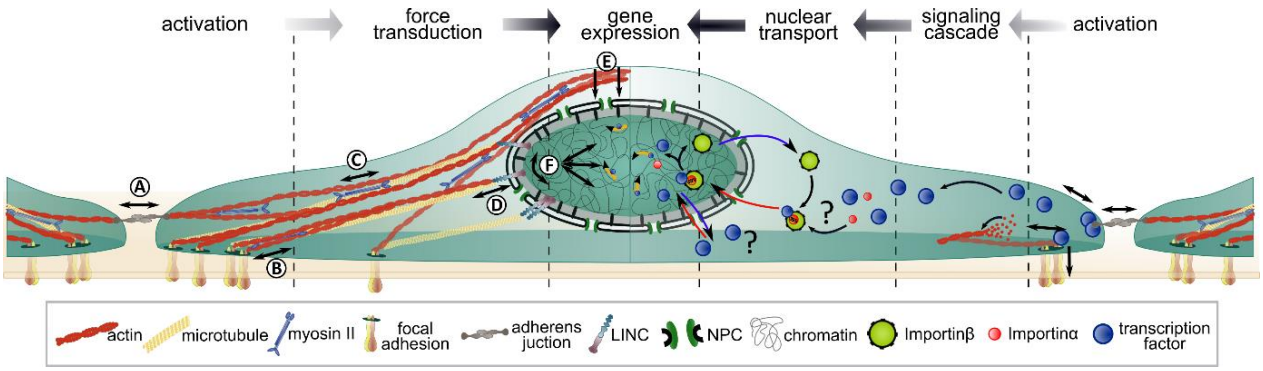

Figure 5.1 Cellular mechanotransduction is mechanical and biochemical.

From the left: Forces applied to cells via (A) adherens junctions or (B) focal adhesions are transmitted across the cell membrane and propagate to the actin cytoskeleton. (C) Filamentous actin and myosin II generate additional internal mechanical stress. (D) LINC complexes and (E) the nuclear actin cap further propagate mechanical signals and deform the nucleus. (F) Overall, these processes distort the nuclear lamina and affect chromatin organization. From the right: In addition to nuclear deformation, mechanical cues can activate mechanoresponsive-signaling cascades by direct dissociation of signaling molecules from adherens junctions or filamentous actin. These molecules include mechanoresponsive TFs, which are trafficked into the nucleus via nuclear pore complexes by the nuclear transport machinery or karyopherin-independent pathways.

NCT and mechanotransduction need to work synergistically to achieve a certain cellular phenotype. Nevertheless, it is unknown whether TFs somehow regulate their own transport by enhancing the transcription of specific NCT machinery *via* a positive feedback loop mechanism.

Within a cell, extracellular forces can be also directly transduced using force-bearing elements of the cytoskeleton, i.e. mechanotransduction (Fig. 5.1). Forces applied to integrins or cadherins through the interactions with the ECM or neighboring cells, are transmitted across the cell membrane and propagated to the actin cytoskeleton (Engler et al., 2006; Wang et al., 2009). Together with microtubules and intermediate filaments, actin creates a force-responsive cytoplasmic network directly connected to the NE and nuclear lamina *via* the Linker of the Nucleoskeleton and Cytoskeleton (LINC) complex (Kirby and Lammerding, 2018). This enables further propagation of mechanical signals to the nucleus which itself can be considered as a mechanosensor (Jahed et al., 2016; Kirby and Lammerding, 2018). Locally mechanotransduction may result in nuclear scaffold deformation, which subsequently leads to changes in chromatin organization, deformation of the nuclear lamina, and DNA melting (Engler et al., 2006; Kirby and Lammerding, 2018; Wang et al., 2009) and thus can cause detachment of chromatin from NE and alter gene expression (Guilluy et al., 2014; Iyer et al., 2012; Tajik et al., 2016). Furthermore, direct contact between lamins and NPCs raises the possibility that the lamina network and particularly its stiffness may affect the opening size of the pore. Indeed, specific NPC subcomplexes (Kampmann and Blobel, 2009; Solmaz et al., 2013) or even the entire NPC structure (Pulupa et al., 2020; Wolf et al., 2009) may potentially undergo conformational changes leading to pore dilation. By this means, NPCs might provide a form of cellular feedback control by regulating NCT during mechanotransduction (Wolf et al., 2009). Moreover, nuclear membrane folds or herniations may be caused directly by external mechanical force. Assuming that NPCs are uniformly spread throughout the nuclear membrane, NPCs found within a fold may not be as “active” since their openings may be obstructed. Likewise, it is possible that NPCs found in tensed nuclear membrane regions may have larger openings and result in overall “leakiness” (Elosegui-Artola et al., 2017). If and how this affects Kapβ occupancy within the NPC is still not known. Although evident, crosstalk between mechanosensing and NCT, and the effect of mechanical disturbances on NCT and NPCs are fundamental problems that remain poorly understood.

5.2 Cell squeezing experiments

To show proof of concept, we employed a home-built instrument that combines a spinning disc (SD) confocal and atomic force microscope (AFM). Merge of both allows for manipulation of biological samples and simultaneous detection of the occurring changes with high spatial and temporal resolution in 3D (Fig. 5.2). Furthermore, an integrated fluorescent recovery after the photobleaching (FRAP) unit provides an opportunity to study alterations in the kinetics of the molecules *in vivo*.

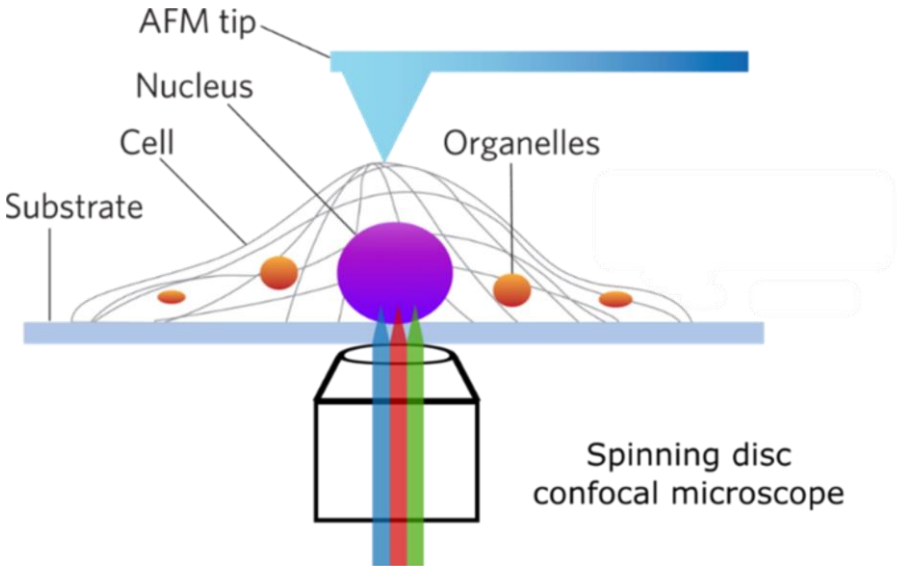

Figure 5.2 Schematic of combined Spinning Disk (SD) and Atomic Force Microscopy (AFM) setup

Simultaneous cell manipulation and recording of their behaviour in 3D opens new avenues to studying mechanobiology.

First, we asked if the force application can lead to the shift in the steady-state distribution of nucleus-destined cargo. To ensure that any potential nuclear leakage will be detected we used MDCK stable cell line expressing maltose-binding protein tagged with GFP and NLS (MBP-GFP-NLS) (76 kDa). In this case, the passive diffusion back to the cytoplasm is highly restricted due to the size of the cargo, while NLS guarantees accumulation of this reporter in the nucleus pre- and post-force application. As such, this cargo also enabled for a straightforward identification of the nuclei.

Cantilevers with flat punch probes were used to locally indent ('squeeze') the cells of interest with an organelle precision (Fig. 5.3A, B). The initial series of experiments focused on the optimization of the experimental conditions, starting with testing indentation speed. We varied the indentation speed between 20 and 500µm/s to find appropriate experimental optimization of settings. Lower indentation speed values up to 300µm/s did not show signs of obvious cargo

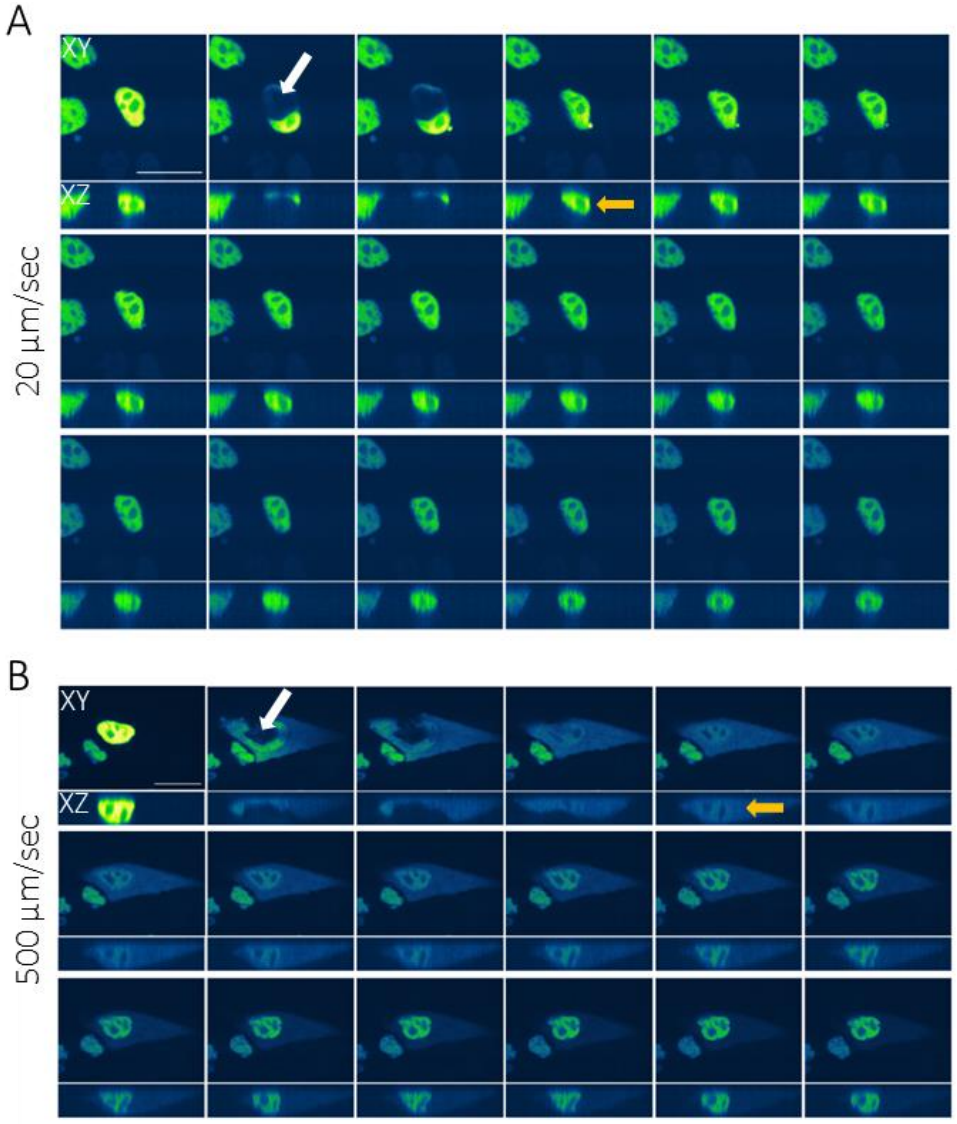

Figure 5.3 Nuclear leakage of cargo upon indentation.

(A) SEM images of the AFM cantilever before and after cutting it to create a flat punch geometry. (A, B) MDCK cells stably expressing MBP-GFP-NLS cargo were 'squeezed' (5µm indentation) with a flat punch cantilever at different indentation speeds. Subsequently, fluorescent signal recovery was recorded by collecting z-stacks. (B) At lower indentation speeds (20- 300 µm /s) leakage from the nucleus has not been observed for any of the tested cells. (C) The high indentation rates ensure the occurrence of the nuclear leakage. Anew accumulation of the MBP-GFP-NLS cargo in the nucleus can be observed over time. Noticeably, right after indentation (panel 4), fluorescent signal in the nucleus is slightly higher than in the cytoplasm, indicating that both compartments did not fully mix. This suggests that NE might stay intact even during the squeezing at the high speed rates. White arrows indicate the indentation step; orange arrows point out the nuclear shape recovery.

leakage from the nuclei (Fig. 5.3A). However, the application of high indentation rates (≥300µm/s) resulted in the leakage of the MBP-GFP-NLS followed by the recovery of the fluorescent signal in the nucleus within minutes after squeezing (Fig. 5.3B). Such a rapid re-accumulation of MBP-GFP-NLS in the nucleus can be explained by the activity of NCT. Interestingly, nuclei returned to their initial shapes following indentation (Fig. 5.3A, B, panels 4-5 XZ side projections). Even though rupture of the NE cannot be completely ruled out (Denais et al., 2016), the observed behavior suggests that the NE had remained intact. Future experiments will require the incorporation of the DNA or nuclear lamina markers to ensure the integrity of NE.

5.3 Prospects

As NCT controls the translocation of a vast number of cargos and must reliably function at different stages of the cell cycle, organ formation, etc., in-depth studies will be required to understand how mechanical forces impact NCT. It is important to note that NCT studies are rather challenging, especially because NCT serves to balance multiple connected transport pathways. As such, perturbation (e.g., overexpression) of one Kapβ could potentially affect other transport components as shown in the preceding Chapter. Therefore, new scientific advancements like CRISPR could be used to create fluorescently-labeled endogenous proteins whose concentration is maintained on the endogenous levels. Additionally, further improvements in techniques like super-resolution microscopy and cryo-electron microscopy will hopefully aid to resolve the functional and structural changes NPCs undergo during normal and pathological states (Szymborska et al., 2013; Turgay et al., 2017). Despite many open questions, it is clear that mechanotransduction and NCT act together to ensure phenotypic changes following the mechanical perturbation of a cell.

5.4 References

Denais, C.M., Gilbert, R.M., Isermann, P., McGregor, A.L., te Lindert, M., Weigelin, B., Davidson, P.M., Friedl, P., Wolf, K., and Lammerding, J. (2016). Nuclear envelope rupture and repair during cancer cell migration. Science *352*, 353-358.

Depping, R., Steinhoff, A., Schindler, S.G., Friedrich, B., Fagerlund, R., Metzen, E., Hartmann, E., and Kohler, M. (2008). Nuclear translocation of hypoxia-inducible factors (HIFs):

involvement of the classical importin alpha/beta pathway. Biochim Biophys Acta *1783*, 394-404.

Elosegui-Artola, A., Andreu, I., Beedle, A.E.M., Lezamiz, A., Uroz, M., Kosmalska, A.J., Oria, R., Kechagia, J.Z., Rico-Lastres, P., Le Roux, A.L.*, et al.* (2017). Force Triggers YAP Nuclear Entry by Regulating Transport across Nuclear Pores. Cell *171*, 1397-1410 e1314.

Engler, A.J., Sen, S., Sweeney, H.L., and Discher, D.E. (2006). Matrix elasticity directs stem cell lineage specification. Cell *126*, 677-689.

Guilluy, C., Osborne, L.D., Van Landeghem, L., Sharek, L., Superfine, R., Garcia-Mata, R., and Burridge, K. (2014). Isolated nuclei adapt to force and reveal a mechanotransduction pathway in the nucleus. Nature cell biology *16*, 376-381.

Iyer, K.V., Pulford, S., Mogilner, A., and Shivashankar, G.V. (2012). Mechanical activation of cells induces chromatin remodeling preceding MKL nuclear transport. Biophys J *103*, 1416-1428.

Jahed, Z., Soheilypour, M., Peyro, M., and Mofrad, M.R. (2016). The LINC and NPC relationship - it's complicated! J Cell Sci *129*, 3219-3229.

Kampmann, M., and Blobel, G. (2009). Three-dimensional structure and flexibility of a membrane-coating module of the nuclear pore complex. Nat Struct Mol Biol *16*, 782-788.

Kassianidou, E., Kalita, J., and Lim, R.Y.H. (2019). The role of nucleocytoplasmic transport in mechanotransduction. Exp Cell Res *377*, 86-93.

Kirby, T.J., and Lammerding, J. (2018). Emerging views of the nucleus as a cellular mechanosensor. Nature cell biology *20*, 373-381.

Masoud, G.N., and Li, W. (2015). HIF-1alpha pathway: role, regulation and intervention for cancer therapy. Acta Pharm Sin B *5*, 378-389.

Oka, M., and Yoneda, Y. (2018). Importin alpha: functions as a nuclear transport factor and beyond. Proc Jpn Acad Ser B Phys Biol Sci *94*, 259-274.

Poon, I.K., and Jans, D.A. (2005). Regulation of nuclear transport: central role in development and transformation? Traffic *6*, 173-186.

Pulupa, J., Prior, H., Johnson, D.S., and Simon, S.M. (2020). Conformation of the nuclear pore in living cells is modulated by transport state. Elife *9*.

Solmaz, S.R., Blobel, G., and Melcak, I. (2013). Ring cycle for dilating and constricting the nuclear pore. Proceedings of the National Academy of Sciences of the United States of America *110*, 5858-5863.

Szymborska, A., de Marco, A., Daigle, N., Cordes, V.C., Briggs, J.A., and Ellenberg, J. (2013). Nuclear pore scaffold structure analyzed by super-resolution microscopy and particle averaging. Science *341*, 655-658.

Tajik, A., Zhang, Y., Wei, F., Sun, J., Jia, Q., Zhou, W., Singh, R., Khanna, N., Belmont, A.S., and Wang, N. (2016). Transcription upregulation *via* force-induced direct stretching of chromatin. Nat Mater *15*, 1287-1296.

Terry, B.R., Matthews, E.K., and Haseloff, J. (1995). Molecular characterisation of recombinant green fluorescent protein by fluorescence correlation microscopy. Biochemical and biophysical research communications *217*, 21-27.

Turgay, Y., Eibauer, M., Goldman, A.E., Shimi, T., Khayat, M., Ben-Harush, K., Dubrovsky-Gaupp, A., Sapra, K.T., Goldman, R.D., and Medalia, O. (2017). The molecular architecture of lamins in somatic cells. Nature *543*, 261-264.

Wang, N., Tytell, J.D., and Ingber, D.E. (2009). Mechanotransduction at a distance: mechanically coupling the extracellular matrix with the nucleus. Nat Rev Mol Cell Biol *10*, 75-82.

Wolf, C., Mofrad, M.J.C.M.D.P.f.M.t.T.M.M., and R. Kamm, e.C.U.P., New York (2009). Mechanotransduction: role of nuclear pore mechanics and nucleocytoplasmic transport. 415-435.